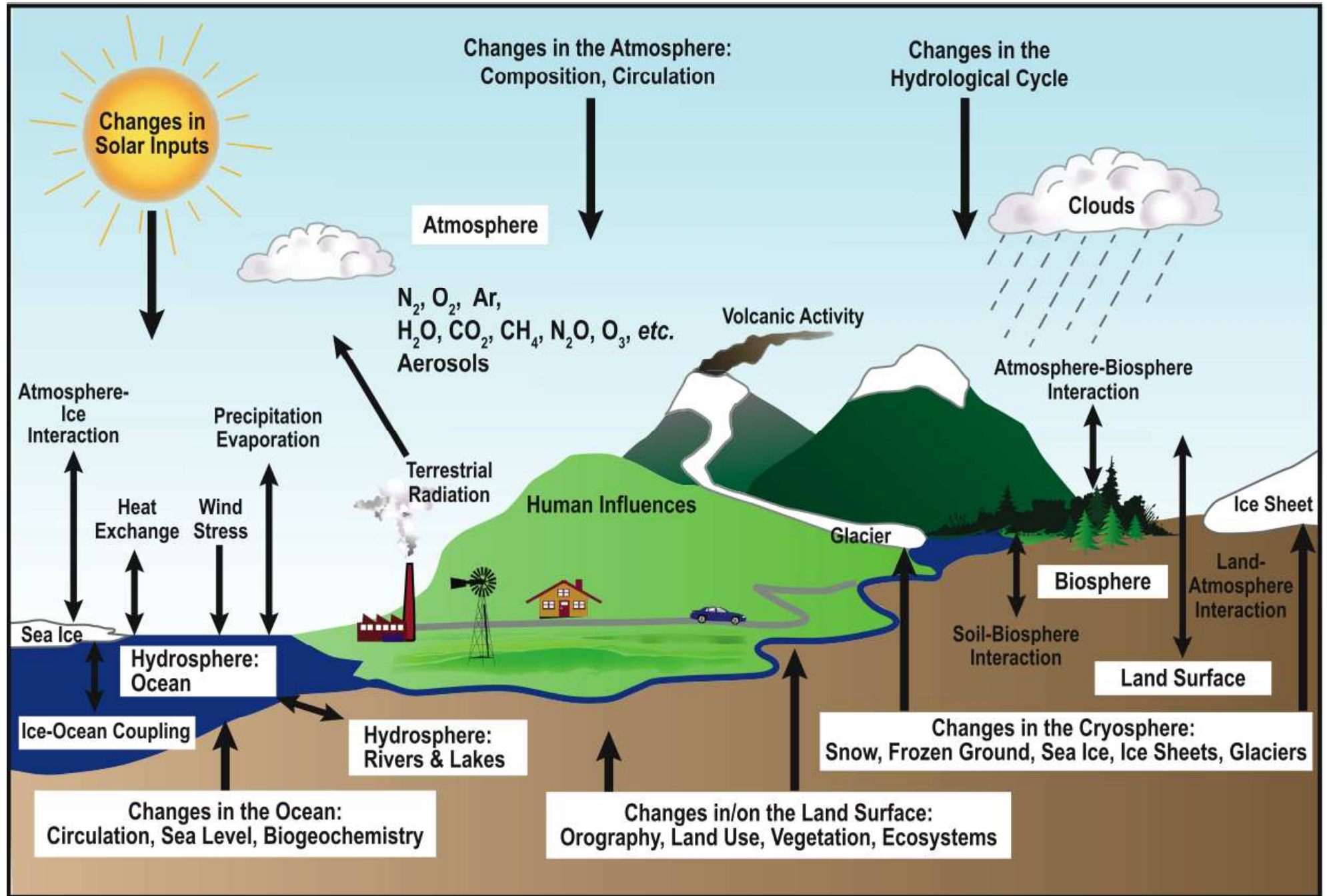


Climate System

http://ipcc-wg1.ucar.edu/wg1/FAQ/wg1_faq-1.2.html



Schematic view of the components of the climate system, their processes and interactions.

Causes of Climate Variability

- Natural origin

external: land-sea distribution, orography

solar constant, orbital variations

volcano

internal variability of the climate system

(e.g., air-sea interaction,,,))

- Anthropogenic origin

emission of greenhouse gases, destruction of ozone layer, land surface modification,,,

Various time scales of climate variability

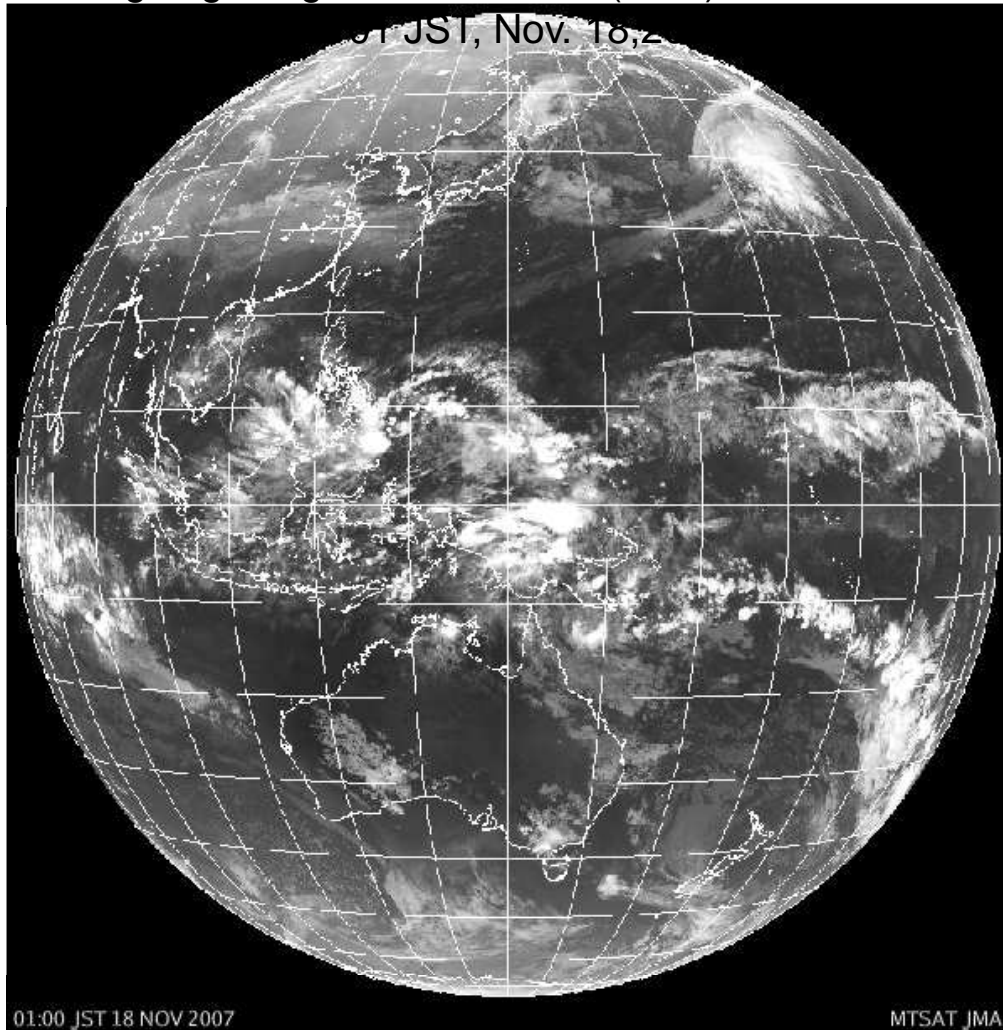
- glacial and interglacial
- ocean thermohaline circulation
- decadal to interdecadal climate variability
- seasonal to interannual climate variability
 - El Nino/Southern Oscillation (ENSO)
 - monsoon variability, TBO
 - modes of variability (NAO, PNA, WP patterns)
- days to intraseasonal variability

N.B. climate system is not in equilibrium

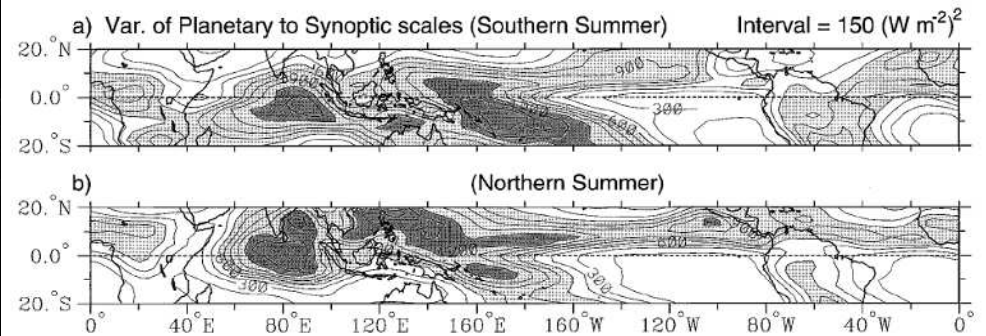
Tropical Disturbances

In Tropics, Heavy Precipitation -> Deep Cloud -> OLR

⌘ Outgoing Longwave Radiation (OLR) from



OLR variance in all planetary to synoptic scales



From Wheeler, M., and G. N. Kiladis, 1999

Wheeler, M., and G. N. Kiladis, 1999: Convectively coupled equatorial waves: **Analysis of clouds in the wavenumber frequency domain.** *J. Atmos. Sci.*, **56**, 374–399.

Red Noise

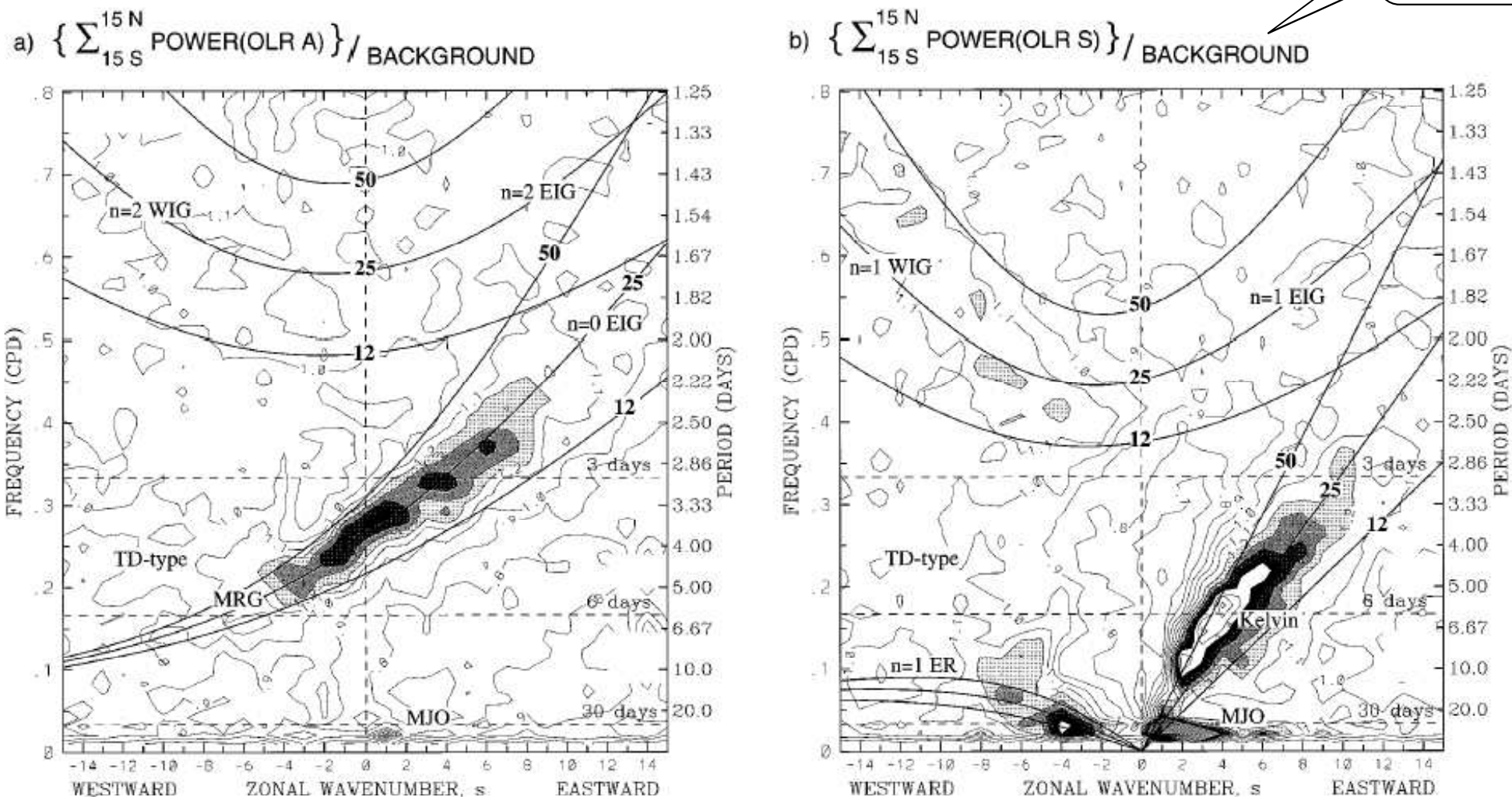


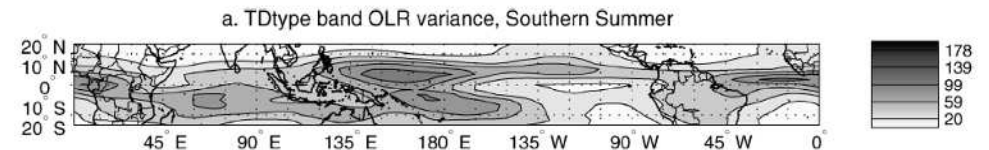
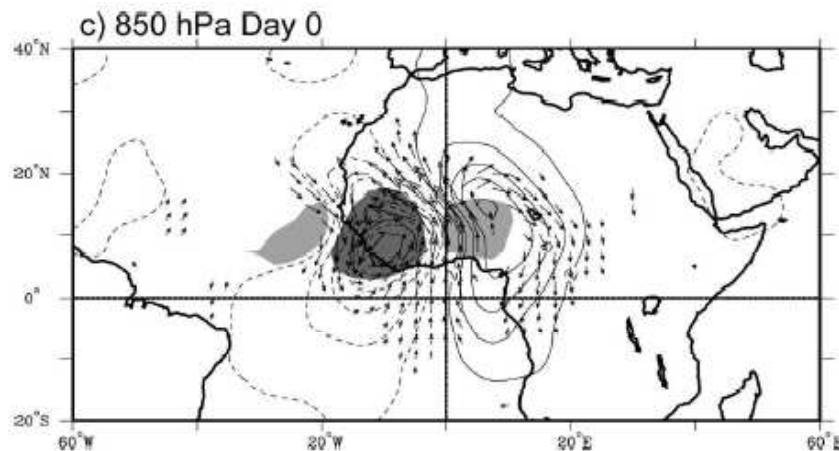
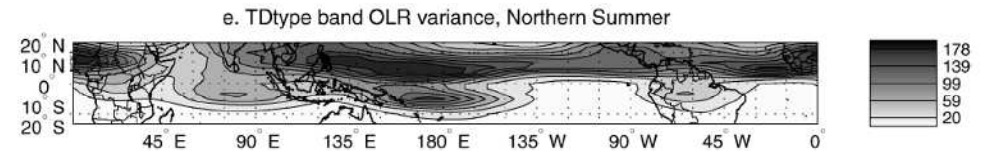
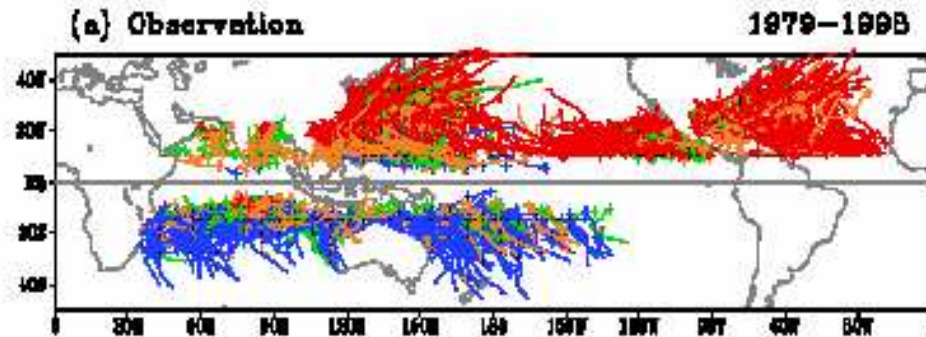
FIG. 3. (a) The antisymmetric OLR power of Fig. 1a divided by the background power of Fig. 2. Contour interval is 0.1, and shading begins at a value of 1.1 for which the spectral signatures are statistically significantly above the background at the 95% level (based on 500 dof). Superimposed are the dispersion curves of the even meridional mode-numbered equatorial waves for the three equivalent depths of $h = 12, 25,$ and 50 m. (b) Same as in panel a except for the symmetric component of OLR of Fig. 1b and the corresponding odd meridional mode-numbered equatorial waves. Frequency spectral bandwidth is $1/96$ cpd.

Easterly waves and Tropical Depression (TD) -type disturbances

TD best tracks

from Jun Yoshimura at MRI/JMA

Roundy, P. and William M. Frank, 2004: A Climatology of Waves in the Equatorial Region. *J. Atmos. Sci.*, **61**, 2105-2132.



Kiladis, G.N., C. D. Thorncroft, and N. M. J. Hall, 2006: Three-Dimensional Structure and Dynamics of African Easterly Waves. Part I: Observations. *J. Atmos. Sci.*, **63**, 2212-2230.

Decomposition of OLR anomalies

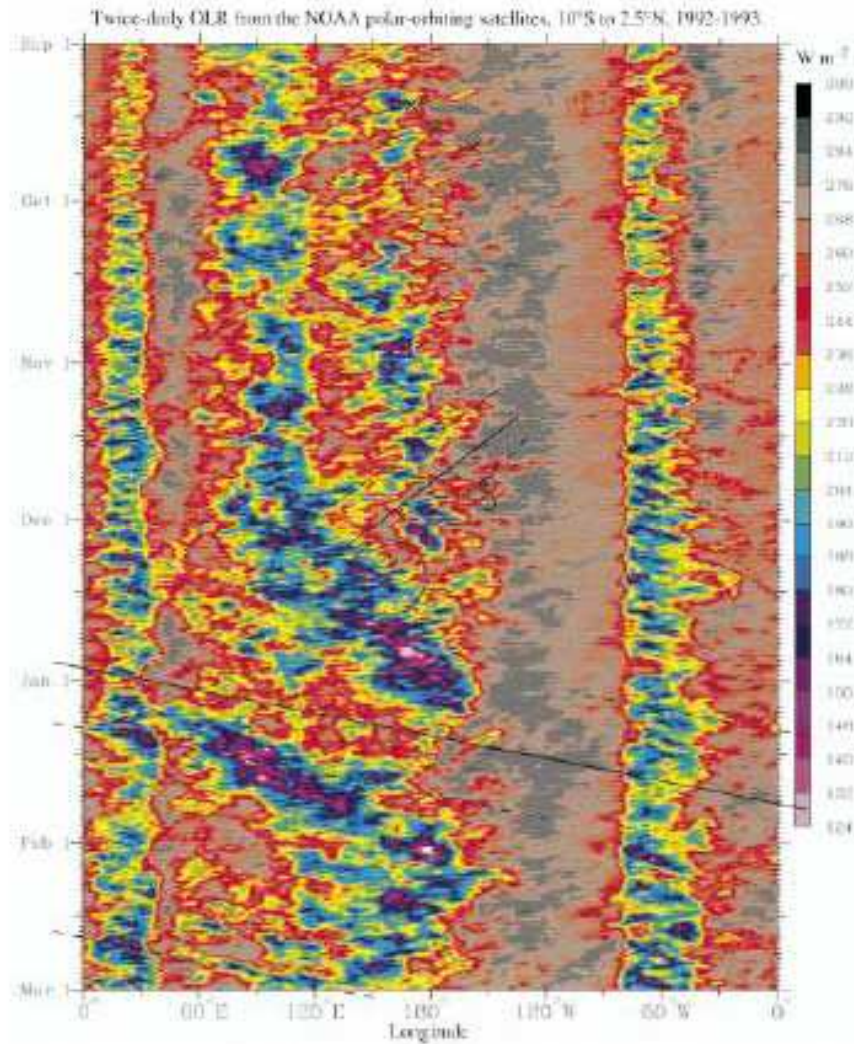
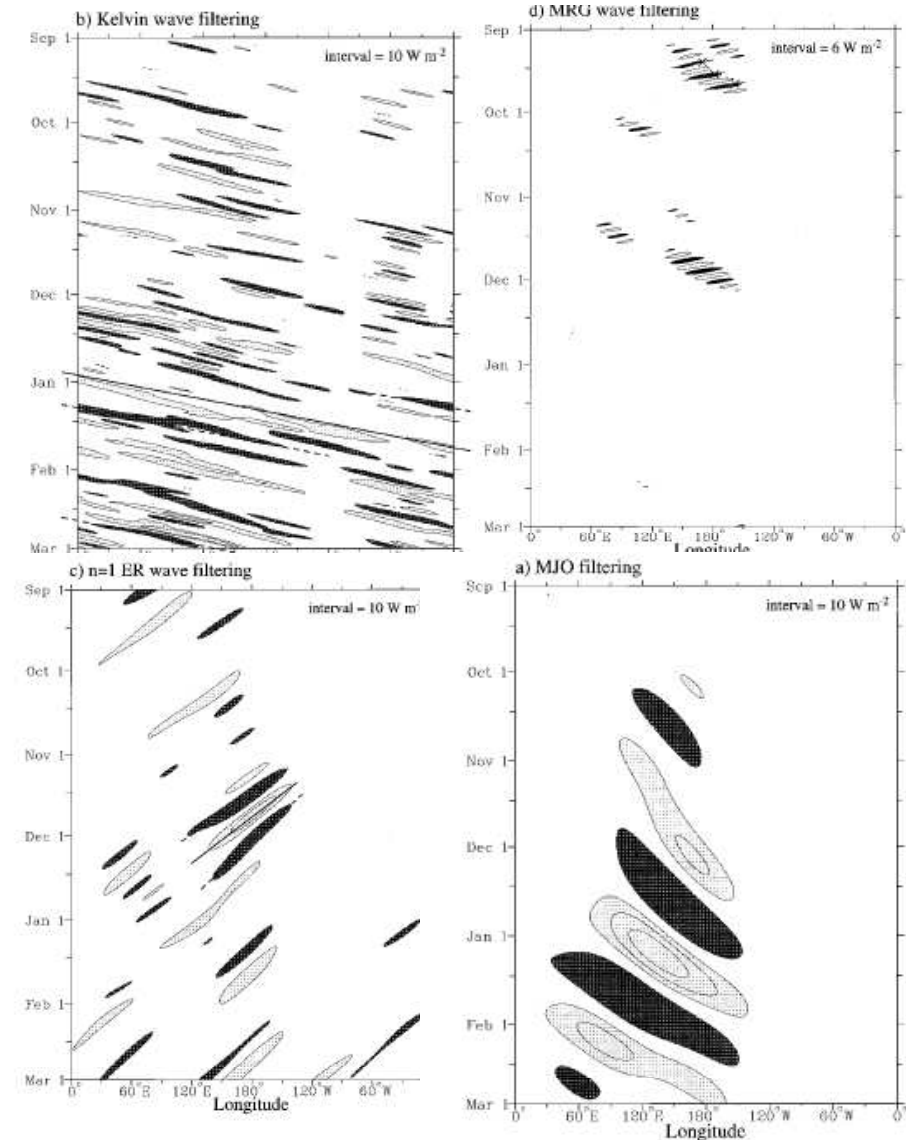


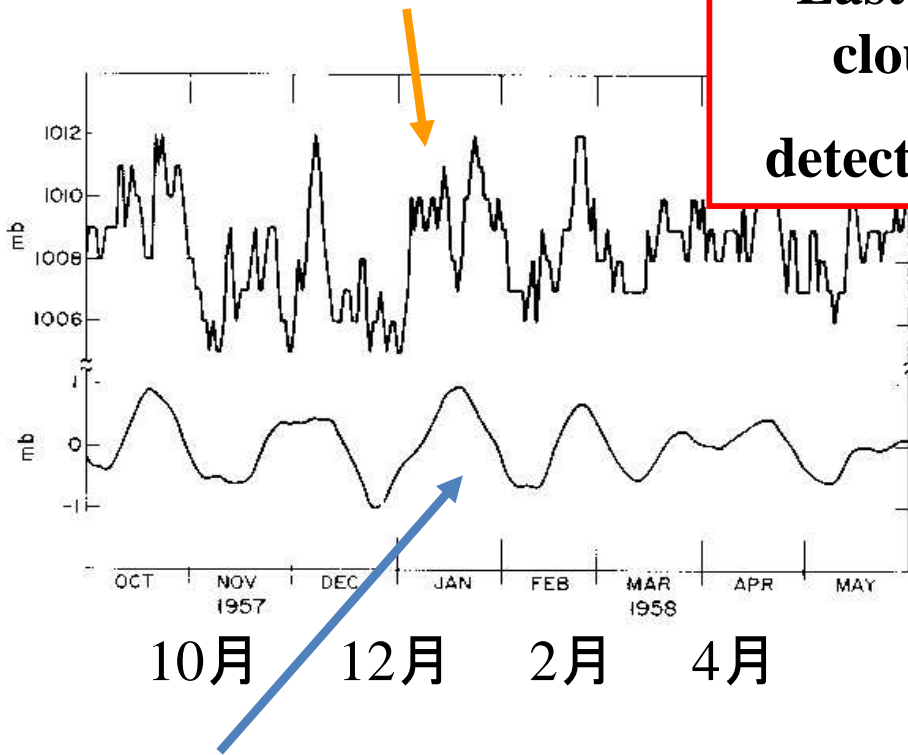
FIG. 8. Time-longitude section of the twice-daily total OLR ($W m^{-2}$) averaged for the latitude from $10^{\circ}S$ to $2.5^{\circ}N$ and for 6×1 September 1992 through 6×1 March 1993. Values correspond to the color bar. Each time section consists of half nighttime and half daytime data from the polar-orbiting satellite (see text for details). Dark lines, circles, and crosses refer to respectively equatorial equatorial wave disturbances, and north those of Fig. 9.

FIG. 9. (a) Time-longitude section of the OLR anomalies for the MJO-filtered band for the same 6-month sample period as Fig. 8, averaged for the latitudes from $10^{\circ}S$ to $2.5^{\circ}N$. The zero contour has been omitted. Light shading for positive anomalies and dark shading and dashed contours for negative anomalies. (b) Same as in panel a except for the Kelvin wave-filtered band. (c) The $n = 1$ ER wave-filtered band. (d) The MRG wave-filtered band.



Madden-Julian Oscillation (MJO)

Surface pressure at Canton
Iceland (3S, 172W)

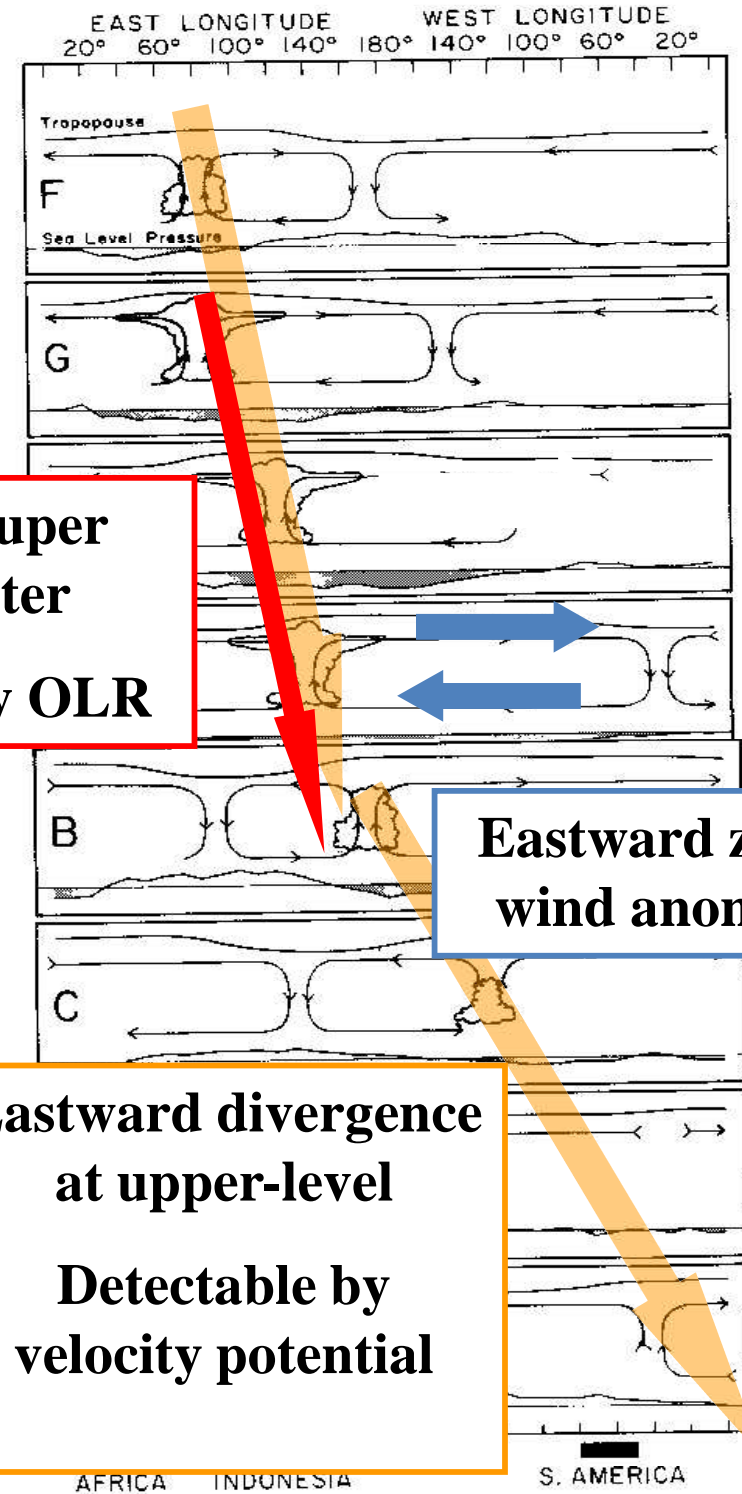


After applying band-pass filter around 45 days

Eastward super cloud cluster detectable by OLR

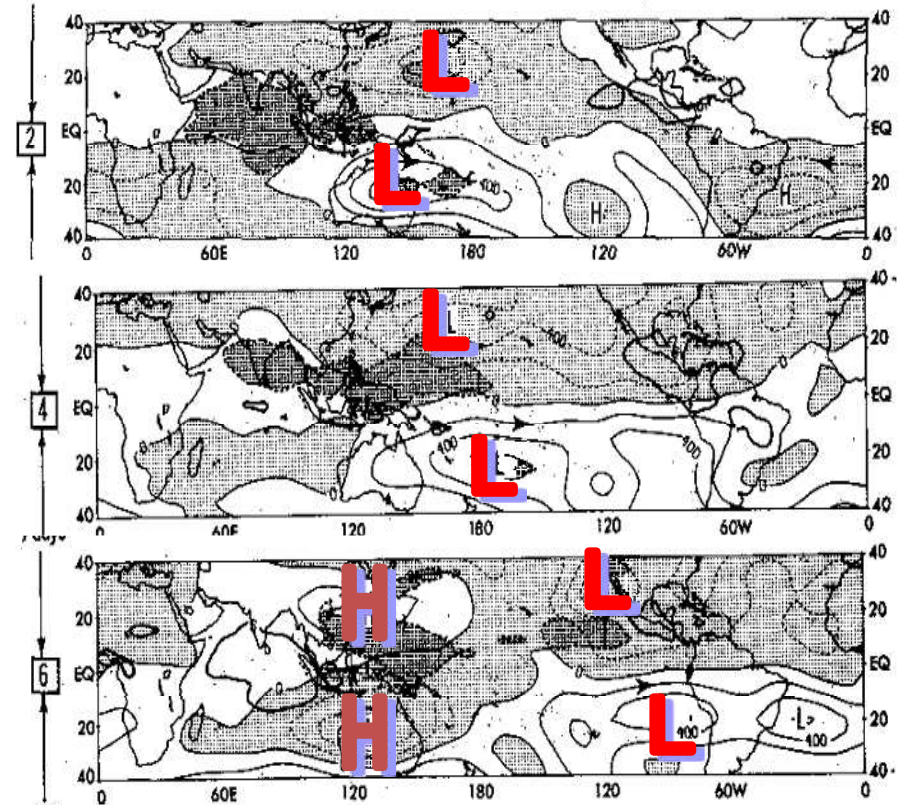
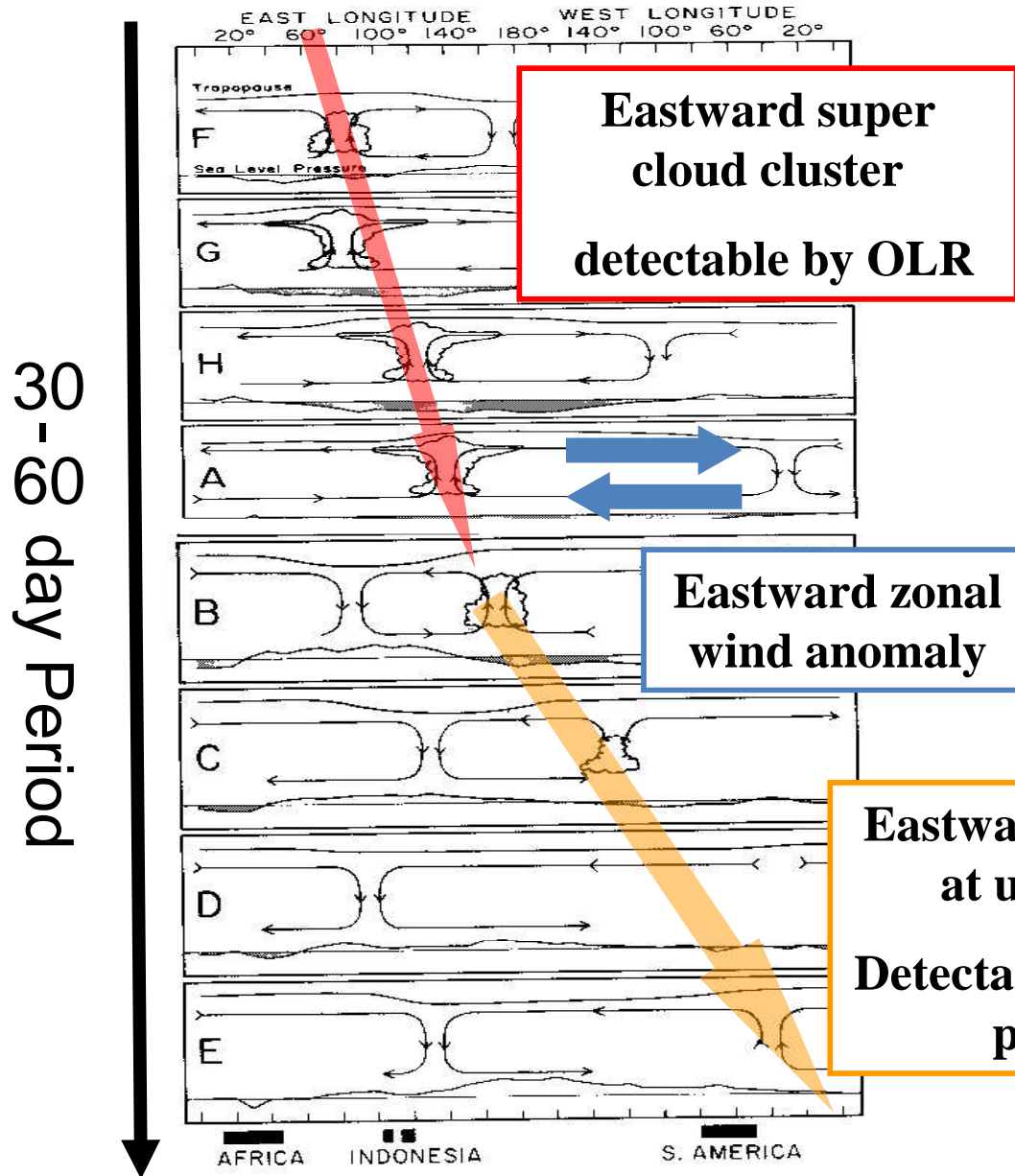
Eastward zonal wind anomaly

Eastward divergence at upper-level Detectable by velocity potential



30-90 day Period

Madden-Julian Oscillation (MJO)

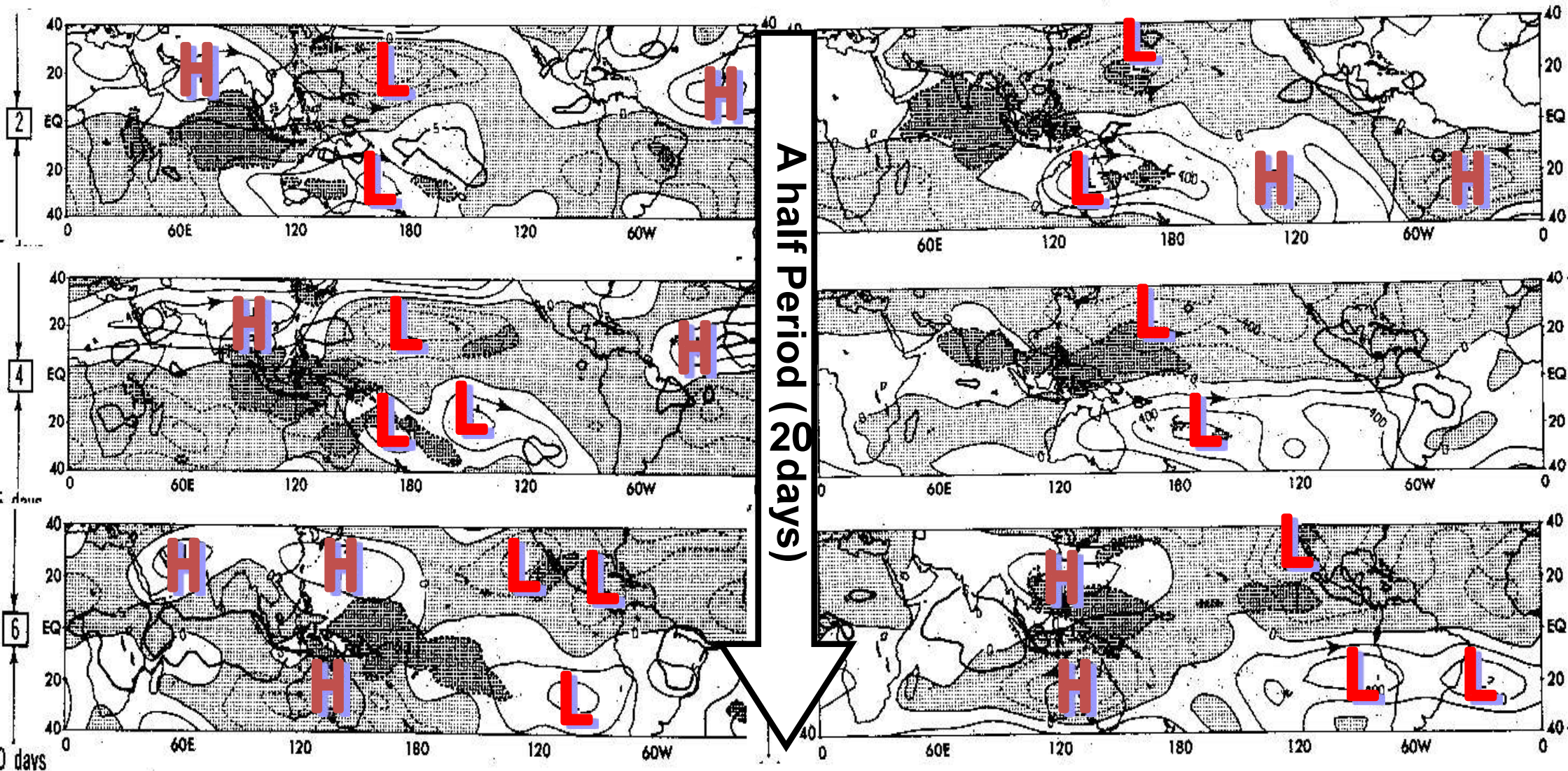


Northern Summer
250 hPa streamfunction
and OLR composites
at phases of MJO

250 hPa streamfunction and OLR composites at phases of MJO

Northern winter

Northern summer



Decomposition of OLR anomalies

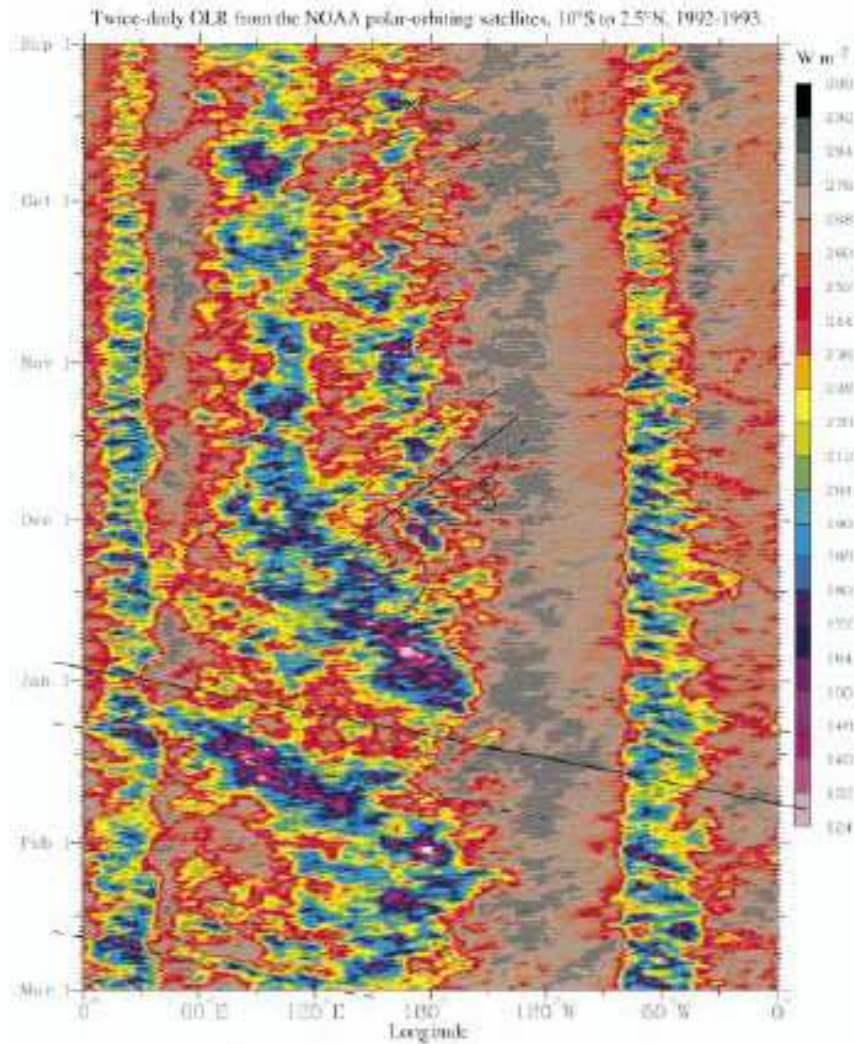
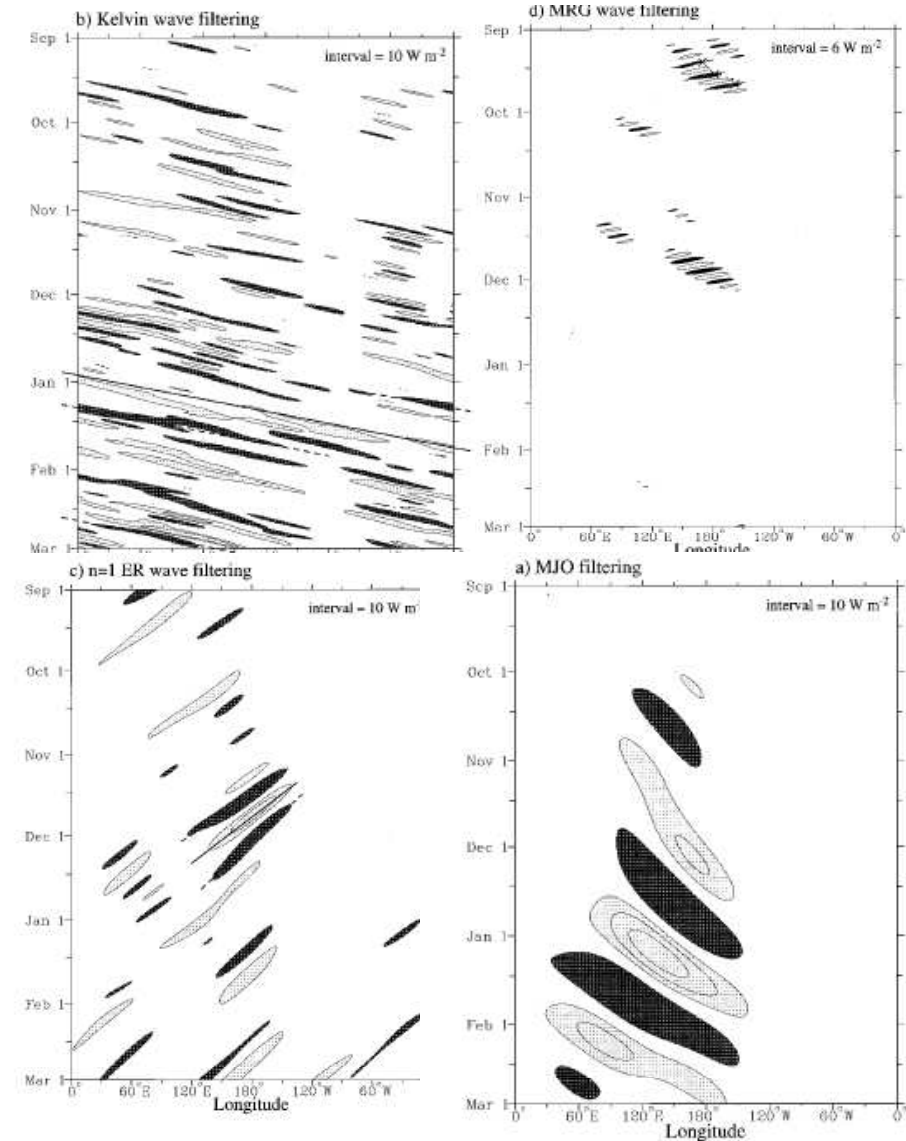
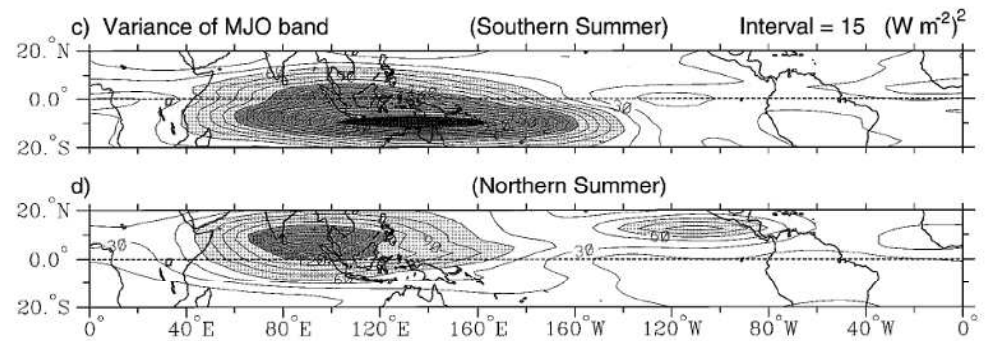
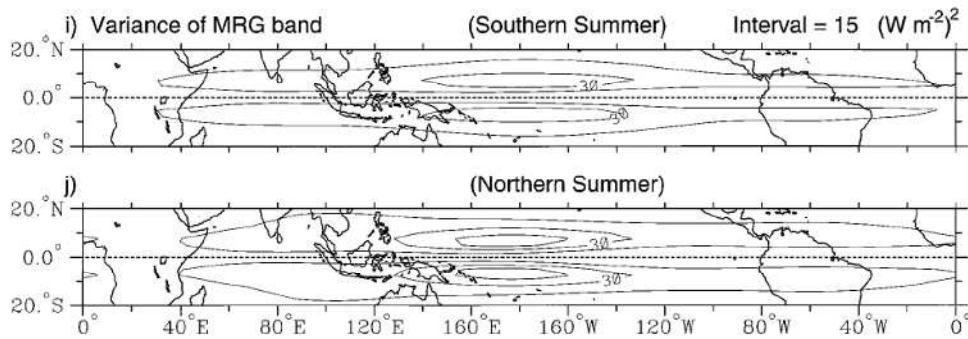
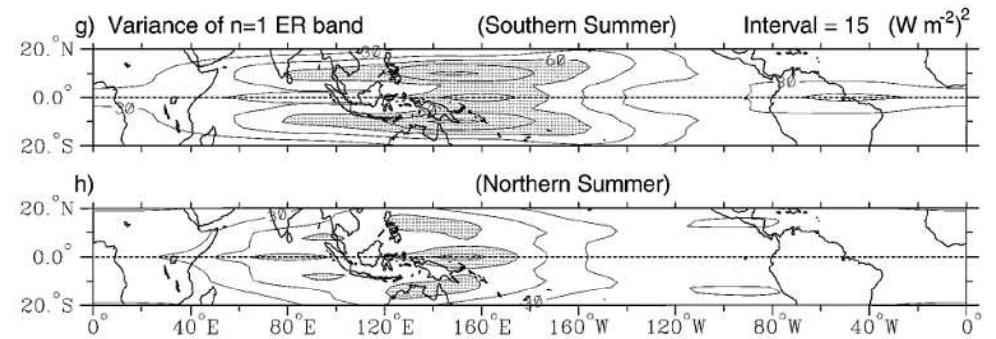
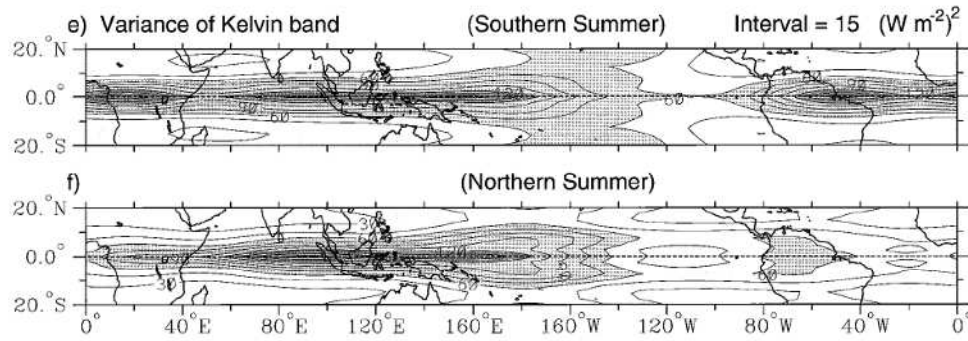


FIG. 8. Time-longitude section of the twice-daily total OLR ($W m^{-2}$) averaged for the latitude from $10^{\circ}S$ to $2.5^{\circ}N$ and for 6 Z 1 September 1992 through 6 Z 1 March 1993. Values correspond to the color bar. Each time section consists of half nighttime and half daytime data from the polar-orbiting satellite (see text for details). Dark lines, circles, and crosses refer to respectively equatorial equatorial wave disturbances, and north those of Fig. 9.

FIG. 9. (a) Time-longitude section of the OLR anomalies for the MJO-filtered band for the same 6-month sample period as Fig. 8, averaged for the latitudes from $10^{\circ}S$ to $2.5^{\circ}N$. The zero contour has been omitted. Light shading for positive anomalies and dark shading and dashed contours for negative anomalies. (b) Same as in panel a except for the Kelvin wave-filtered band. (c) The $n = 1$ ER wave-filtered band. (d) The MRG wave-filtered band.

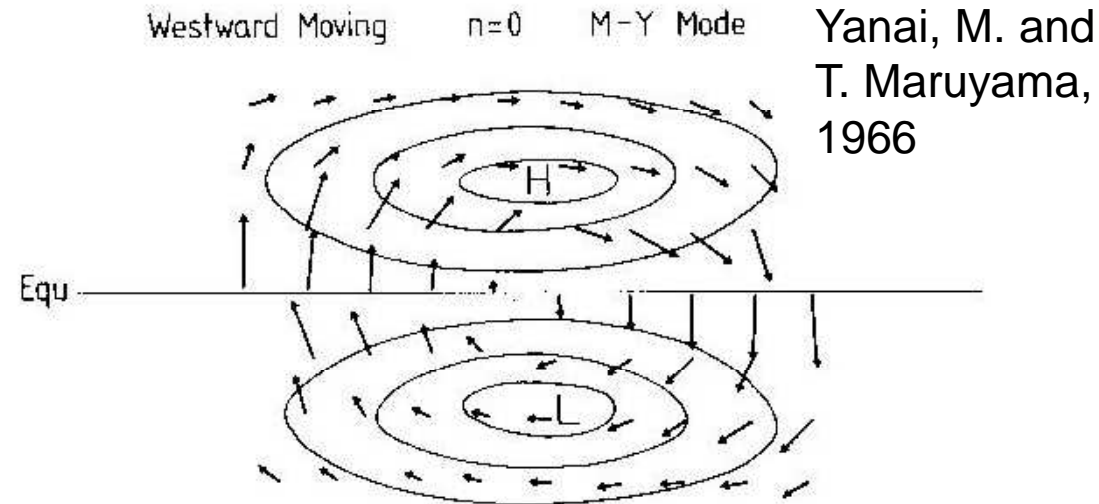
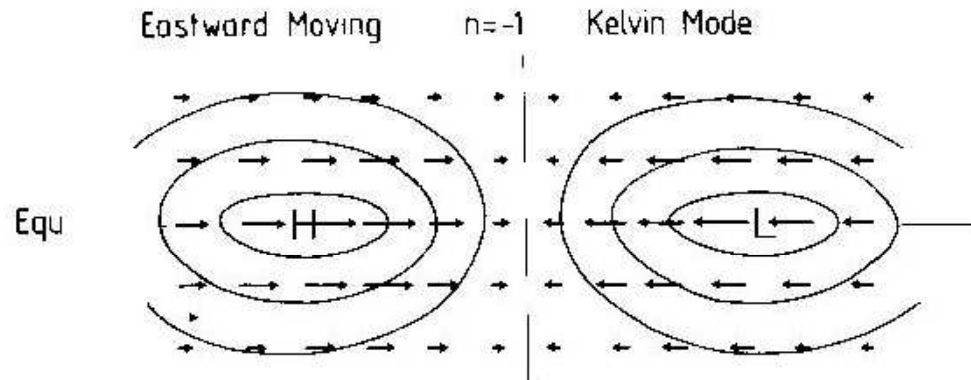


Geographical distribution of Convectively coupled equatorial waves

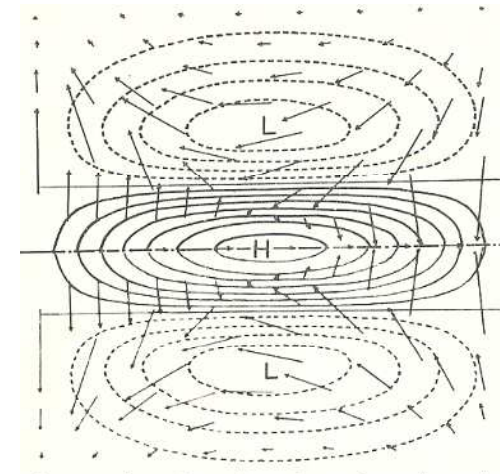
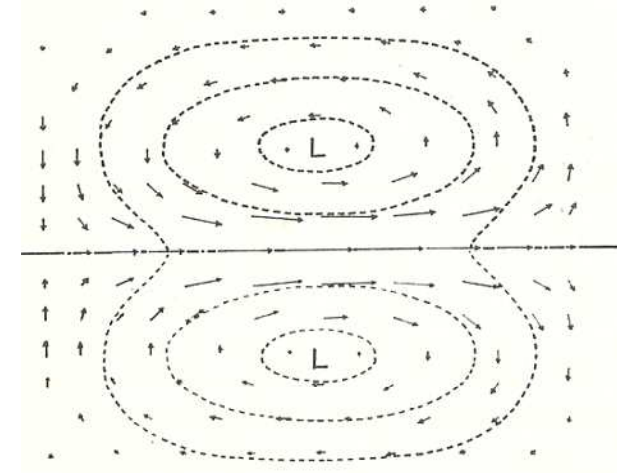


Equatorial Waves

Kelvin wave



ER: Rossby wave ($n=1$)

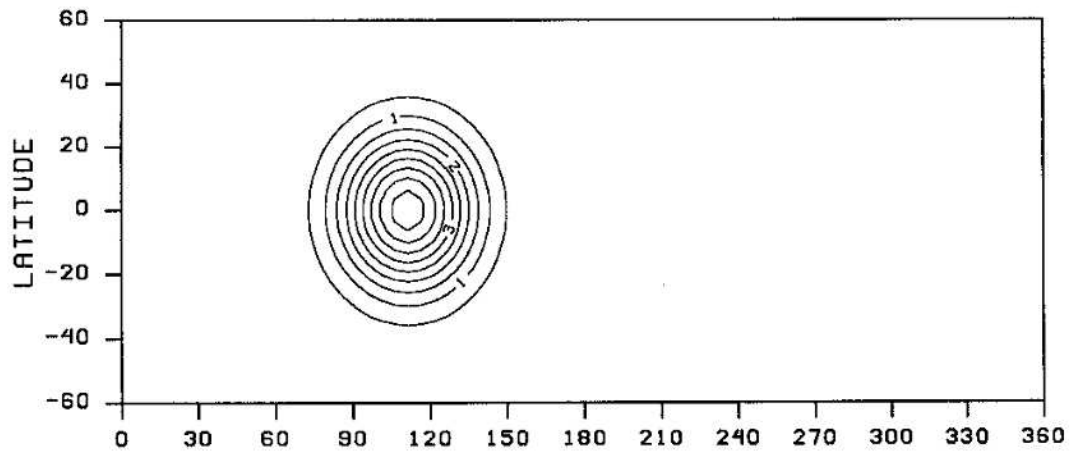


MRG : mixed Rossby-Gravity wave

EIG: eastward propagating
inertio-gravity wave ($n=1$)

If a water mountain is put at the equator

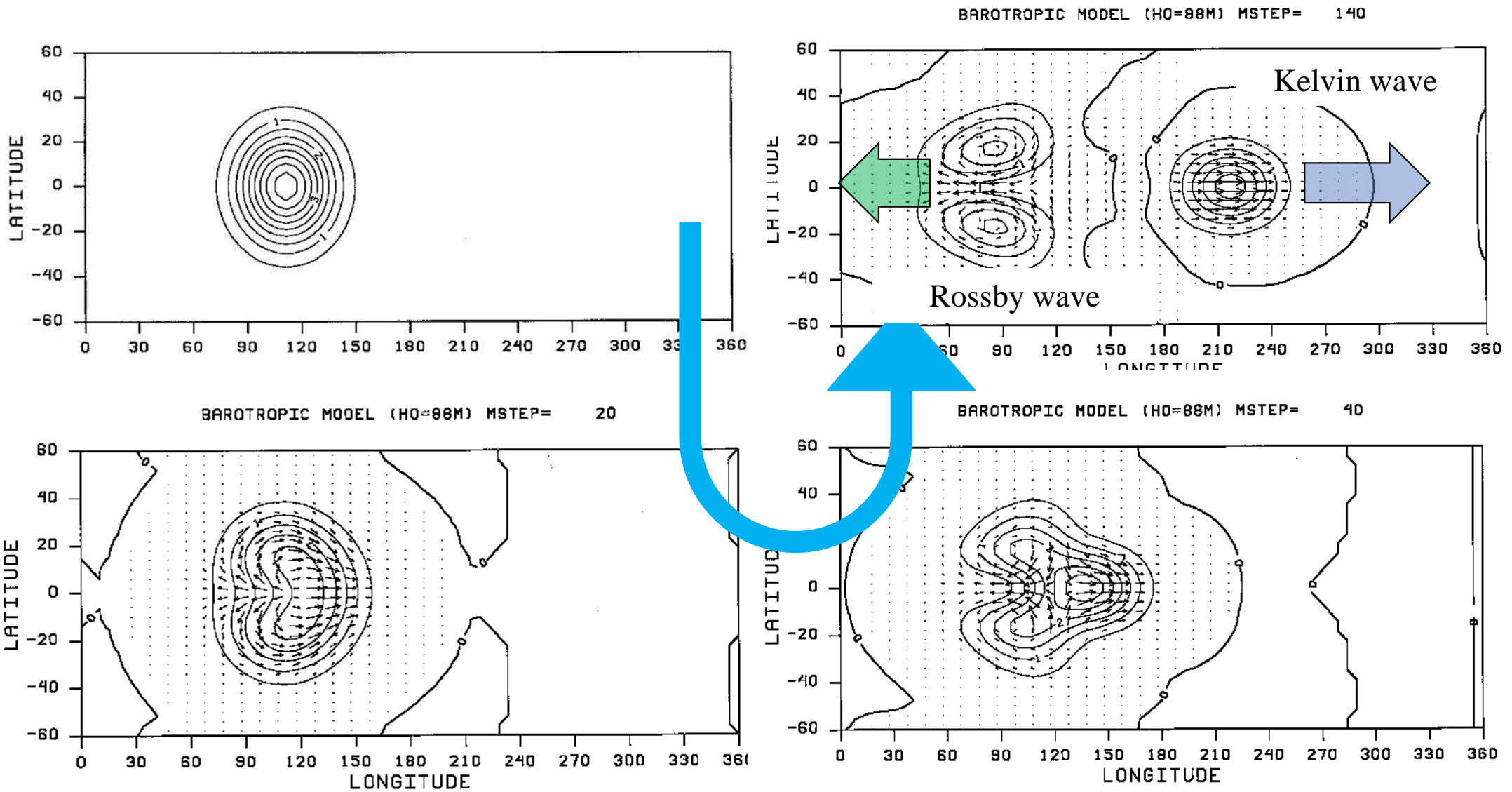
How does it evolve next?



If a water mountain is put at the equator

How does it evolve next?

=> East-west asymmetry moving

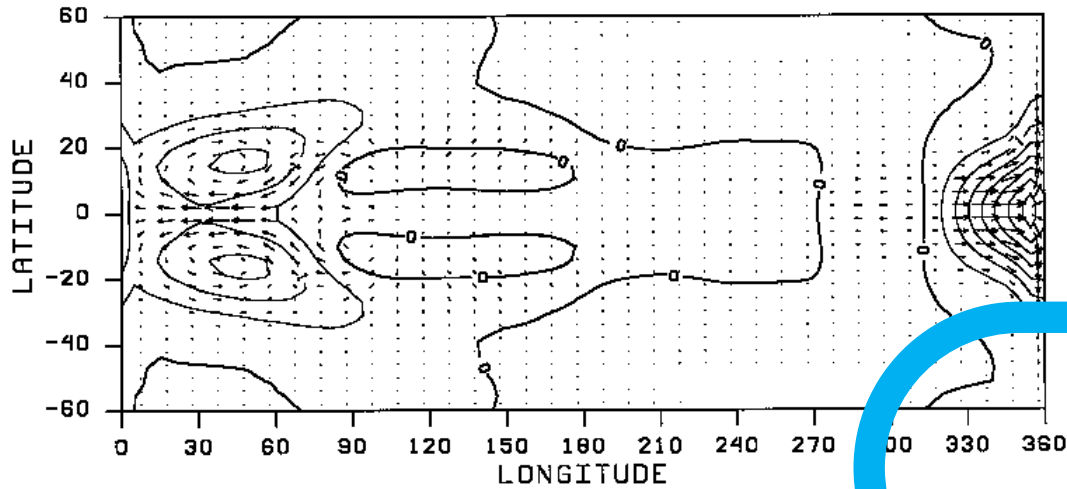


Ocean (If the pool is enclosed with walls)

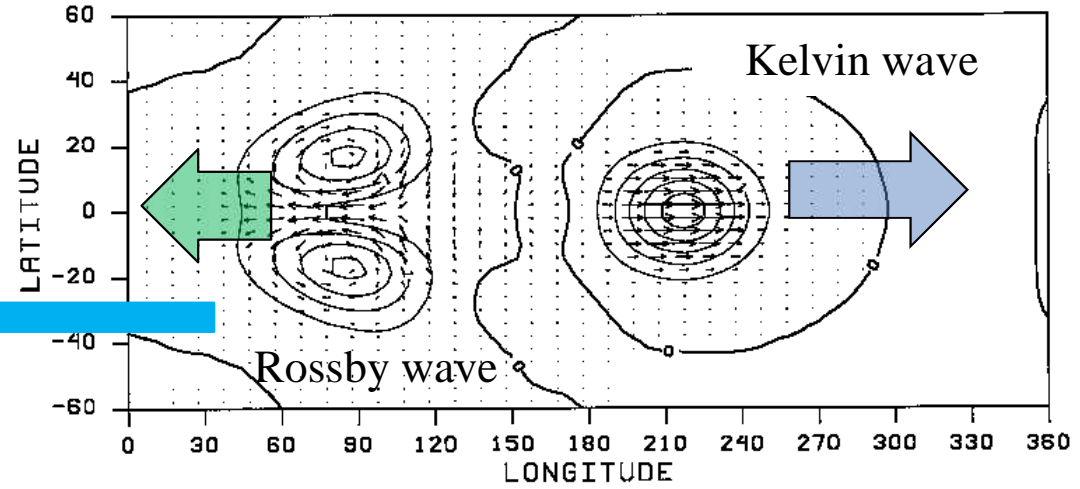
How does it evolve next?

=> Reflection at the walls

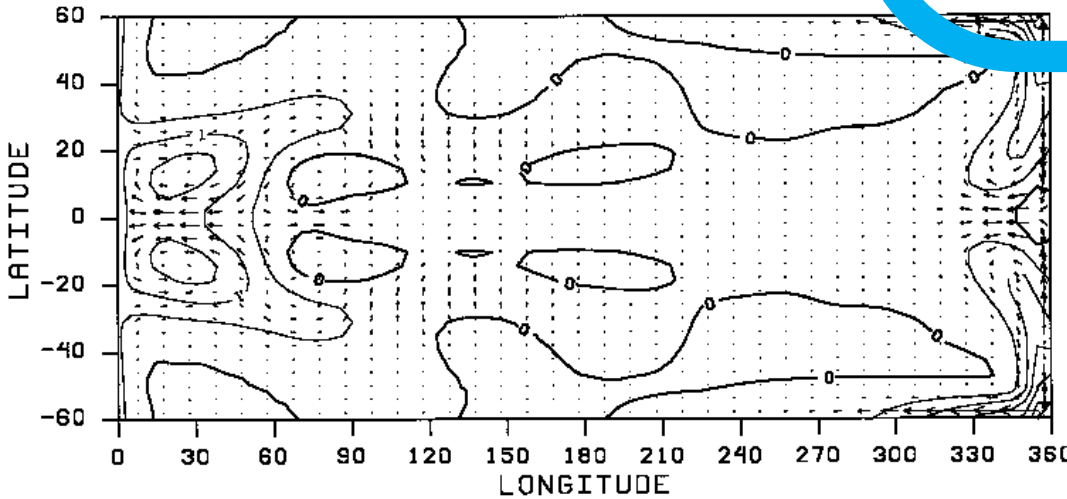
BAROTROPIC MODEL (H0=88M) MSTEP= 320



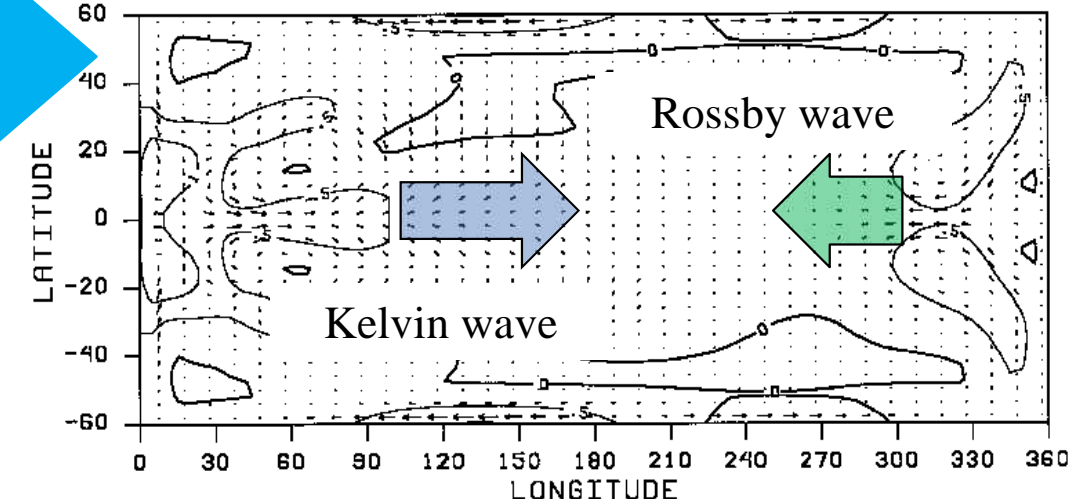
BAROTROPIC MODEL (H0=88M) MSTEP= 140



BAROTROPIC MODEL (H0=88M) MSTEP= 40



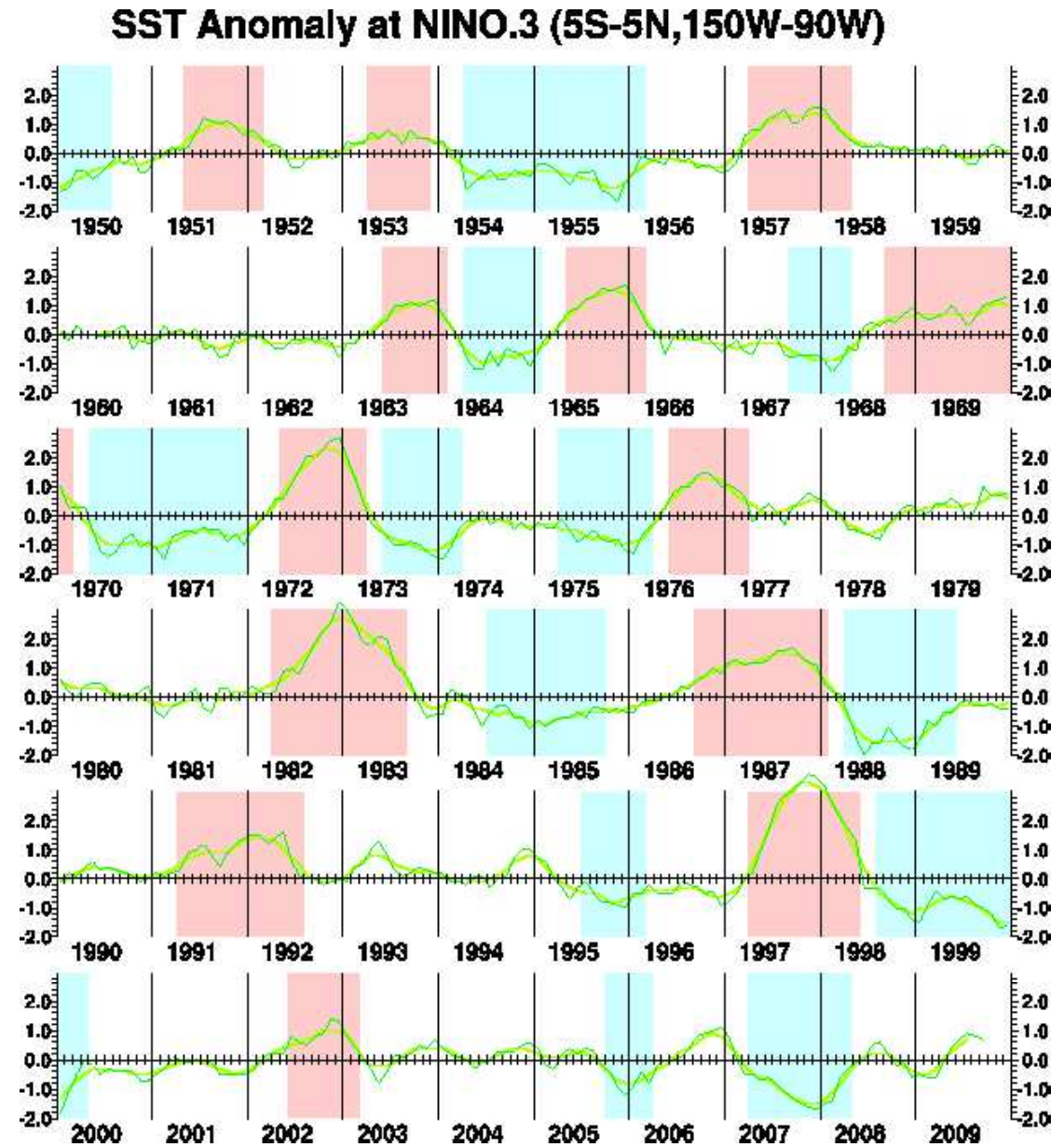
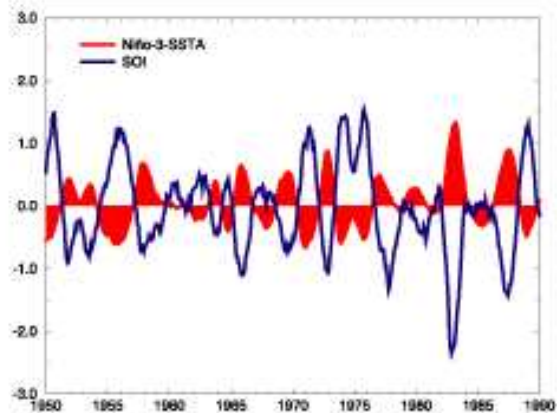
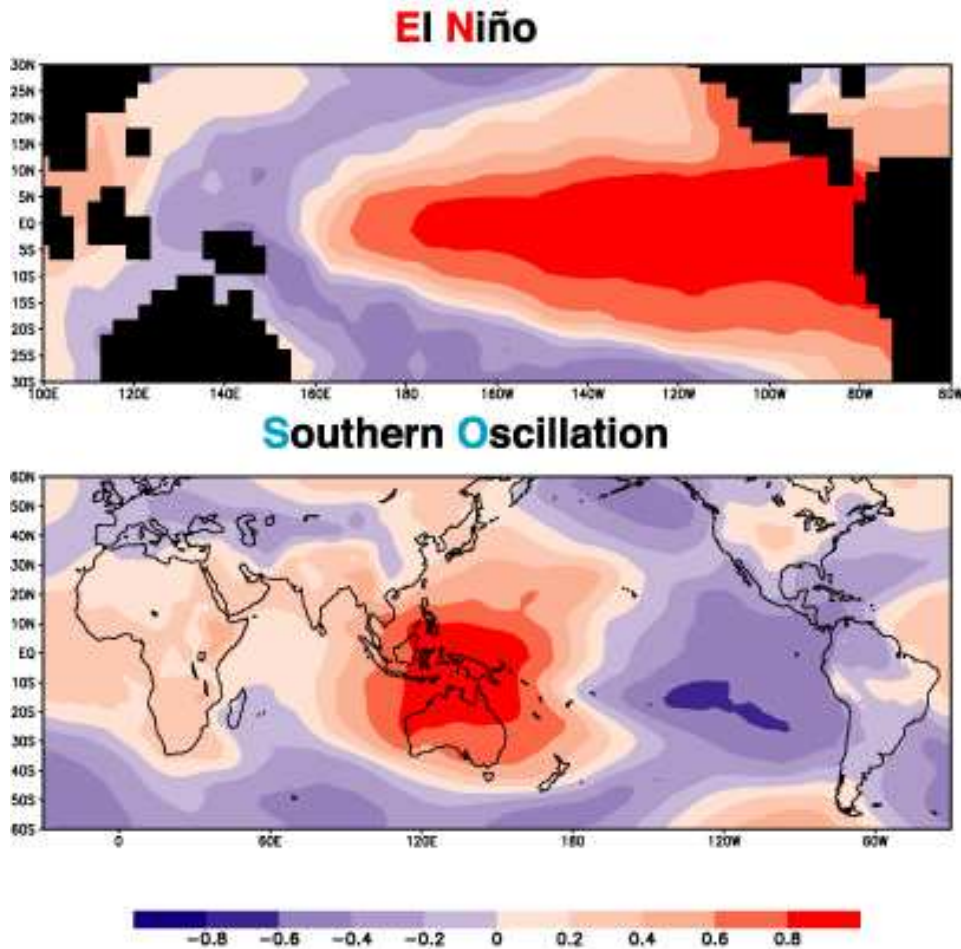
BAROTROPIC MODEL (H0=88M) MSTEP= 540



Climate Variability

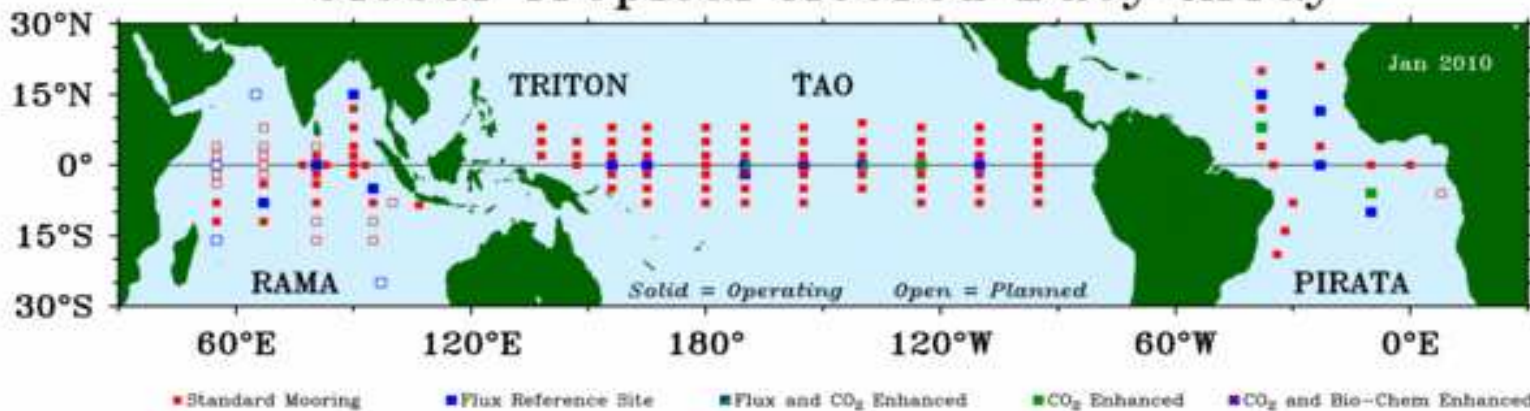
G1: ENSO and IOD : Seasonal Predictions

from JMA website





Global Tropical Moored Buoy Array



TAO Project Office, NOAA/PMEL

Research Moored Array for African-Asian-Australian Monsoon Analysis and Prediction (RAMA)

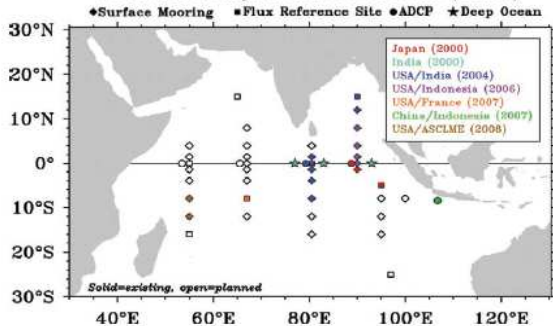


FIG. 4. Schematic of RAMA as of Dec 2008. Filled symbols indicate occupied sites. Color coding indicates national support, with year of first involvement shown in the upper-right box. Open symbols indicate sites not yet instrumented. ASCLME is a consortium of nine African nations including Kenya, Tanzania, Mozambique, South Africa, Madagascar, Mauritius, Seychelles, Somalia, and Comoros.

Pacific Marine Environmental Laboratory

Tropical Atmosphere Ocean project

Michael J. McPhaden, Director

Home Project overview Data display Data delivery El Niño & La Niña Site map

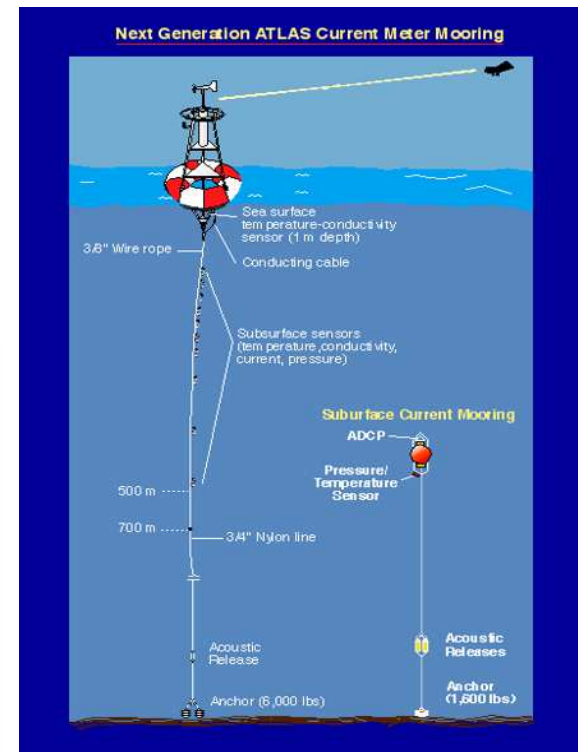
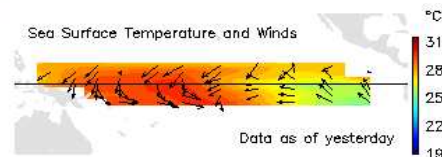
Find

Friday February 12, 2010 (PDT)



The TAO Story

Real-time data from moored ocean buoys for improved detection, understanding and prediction of El Niño and La Niña.



PIRATA Home Station Plots Data Display & Delivery Technical Information Meeting Reports Sensor Status Cruises

Prediction and Research Moored Array in the Atlantic (PIRATA)

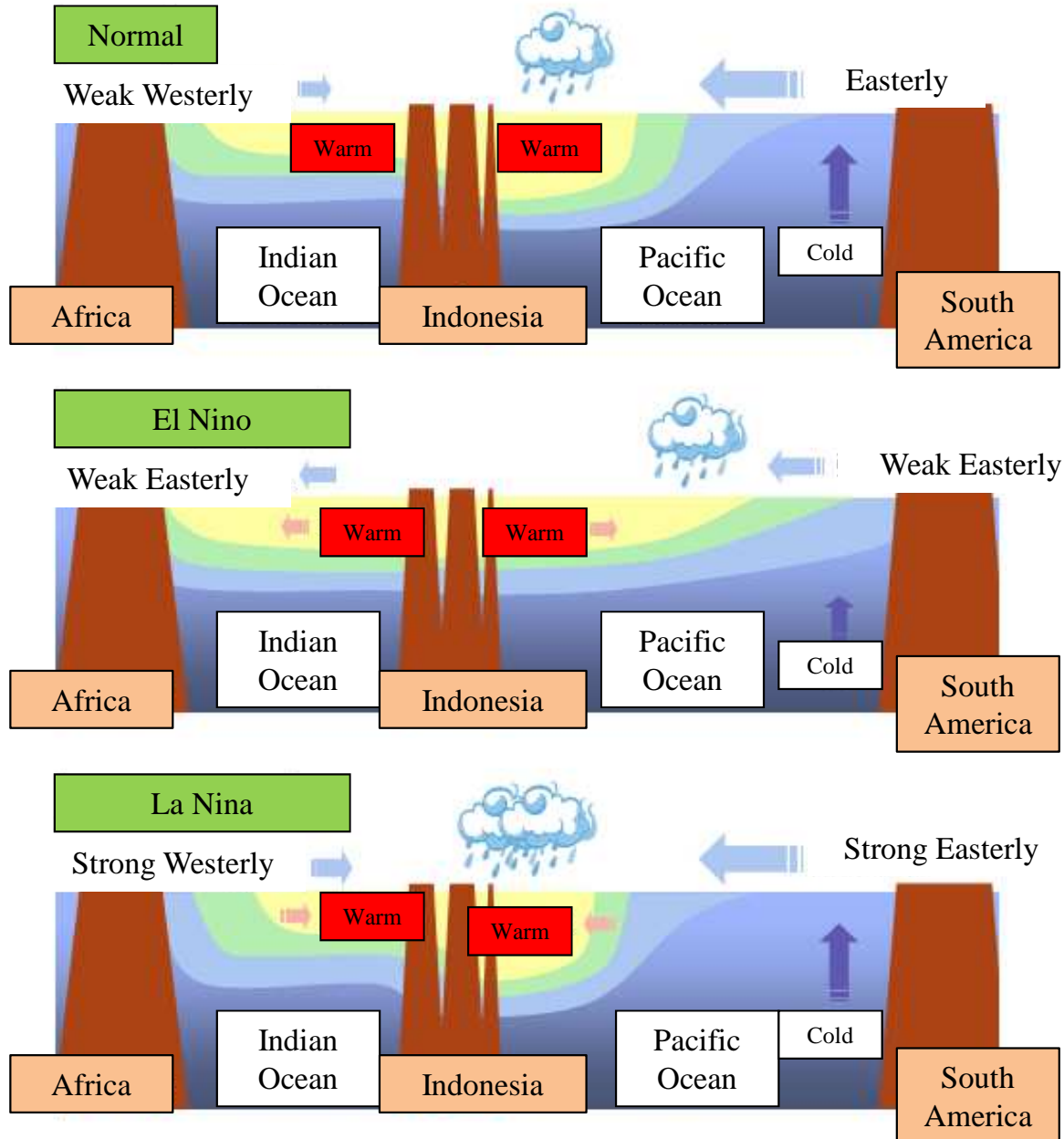
PIRATA is a program designed to study ocean-atmosphere interactions in the tropical Atlantic that affect regional climate variability on seasonal, interannual and longer time scales. The array was originally developed in the mid-1990s and has undergone expansions and enhancements since 2005 to improve its utility for describing, understanding, and predicting societally relevant climate fluctuations. PIRATA has been implemented through multi-national cooperation in support of CLIVAR, GOOS, GCOS, and GEOS. Financial, technical and logistic support are provided by France (IRD) in collaboration with Meteo-France, CNRS and IFREMER, Brazil (INPE and DHO) and the USA (NOAA). Data are freely available for research and operational applications via the World Wide Web and the Global Telecommunications System.



French R/V Antea, photo courtesy Jacques Servain

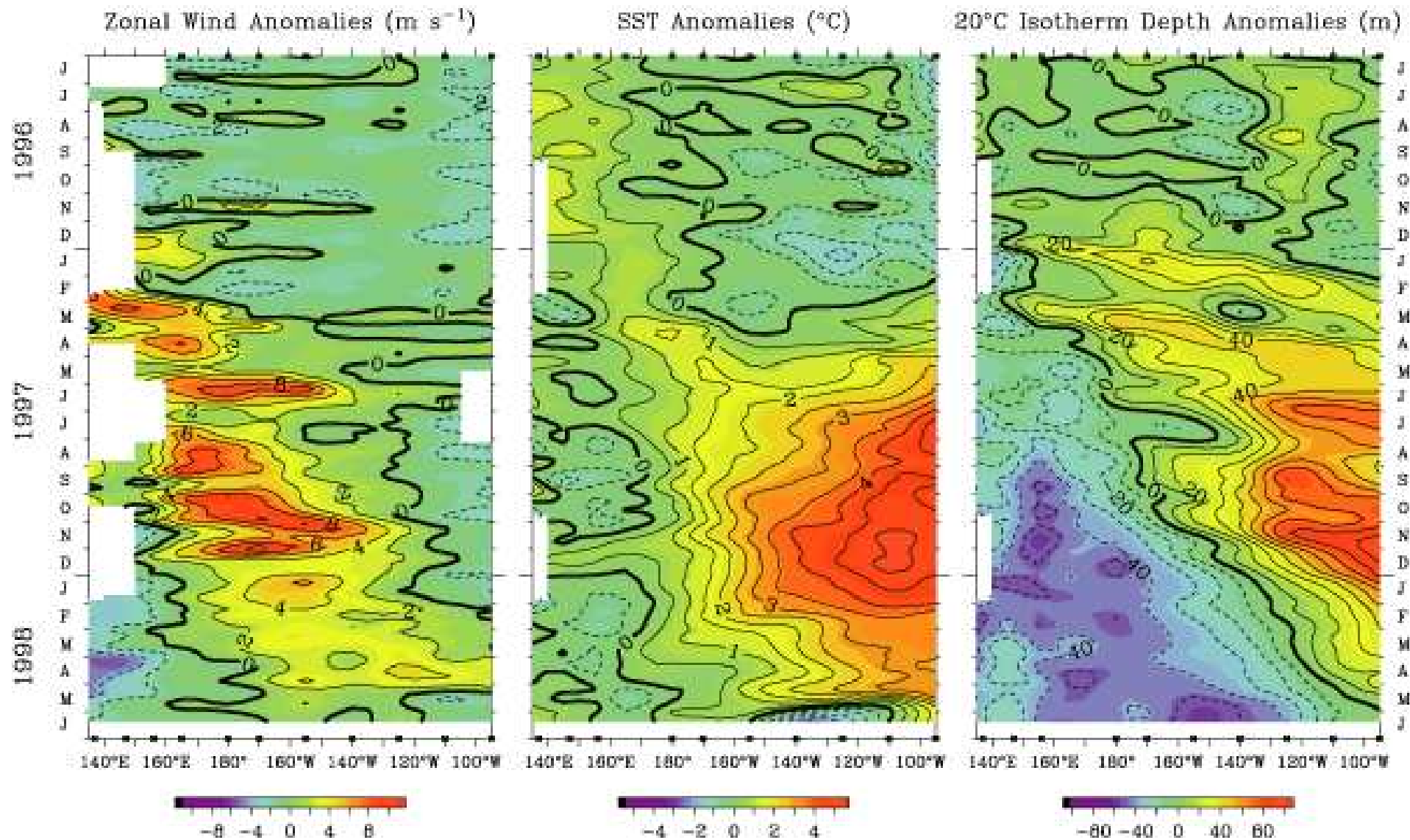
Brazilian R/V Antares, photo courtesy Paulo Artino

ENSO Mechanism



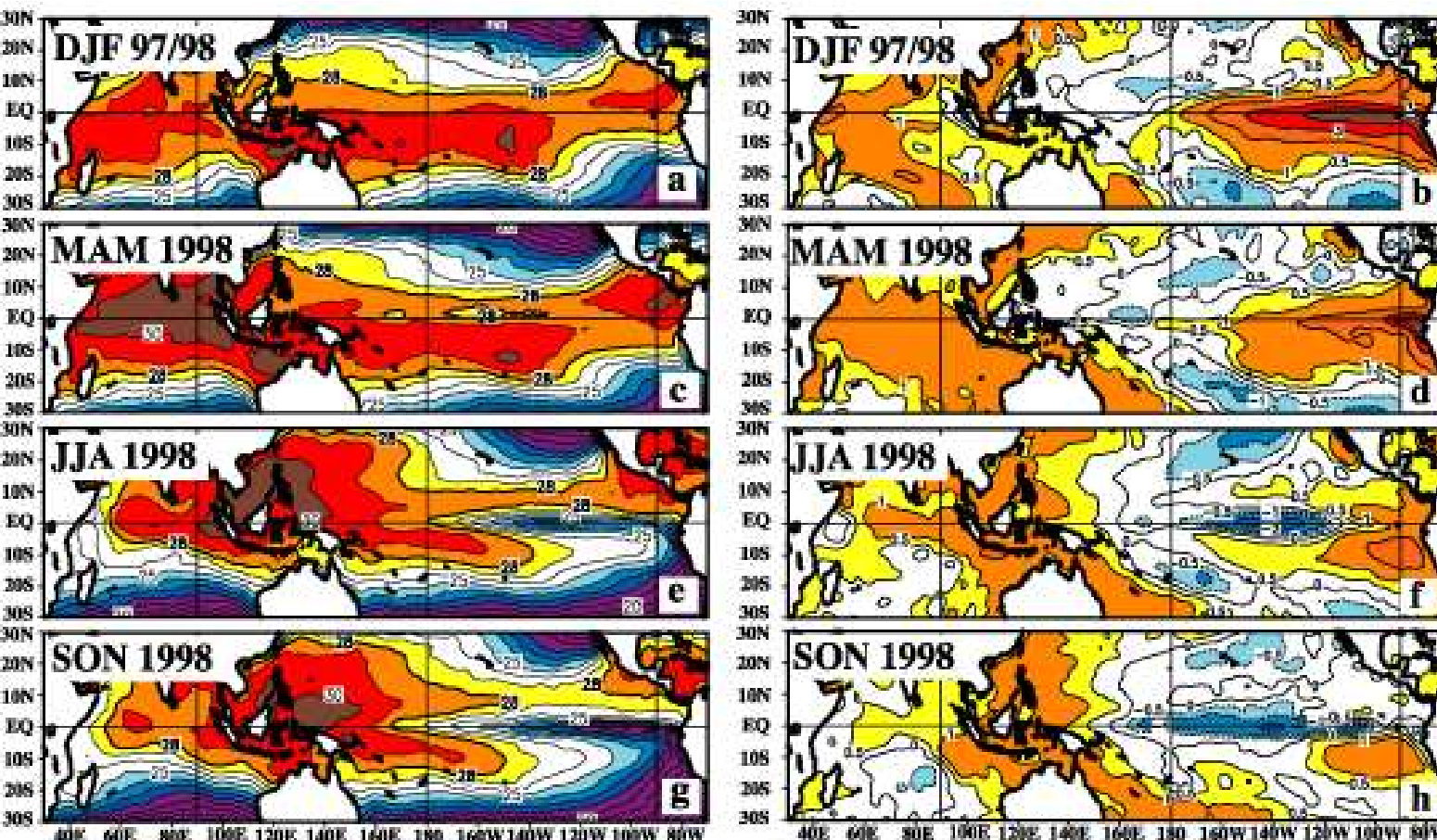
ENSO 1997/98

Five Day Mean Zonal Wind, SST, and 20°C Isotherm Depth 2°S to 2°N Average

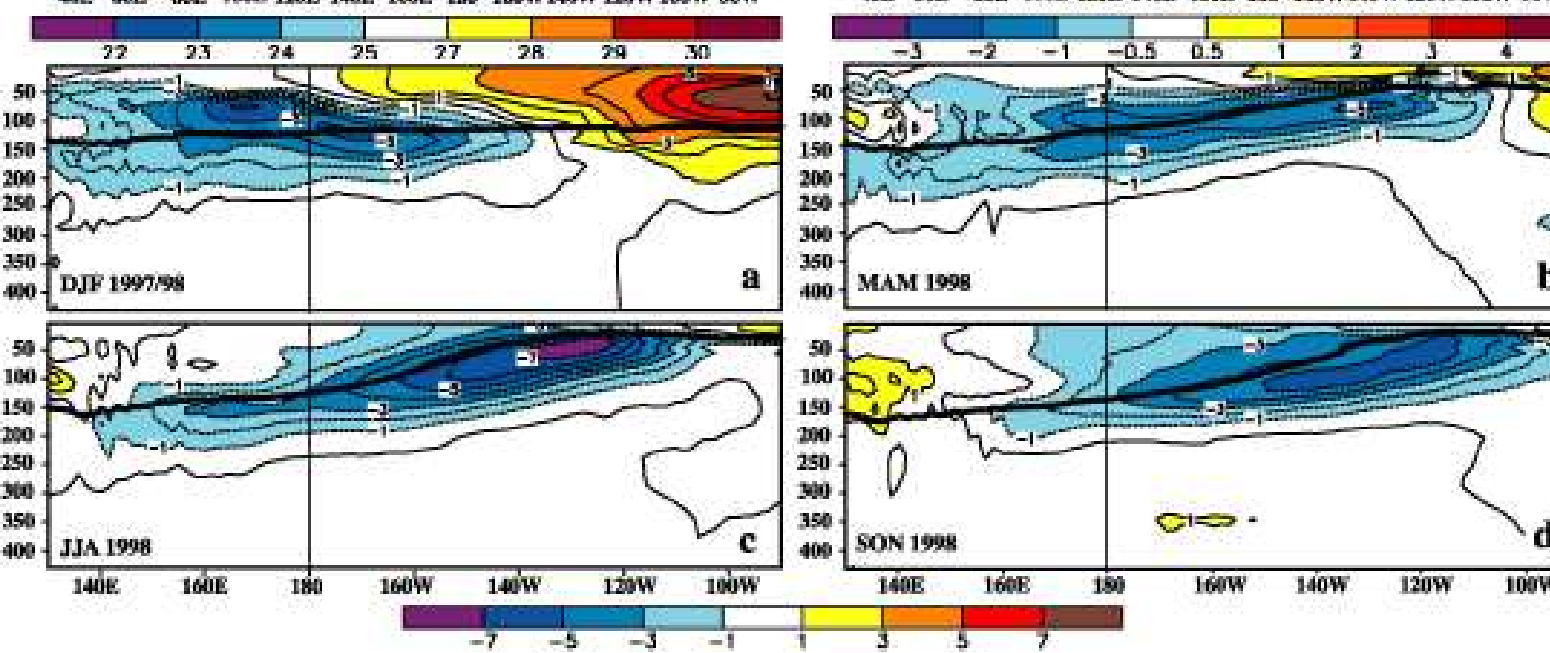


Time-longitude sections of anomalies in the surface zonal winds (m/sec), SST (° C) and 20° C isotherm depth (m) for the 24 months. Analysis is based on 5-day averages between 2° N-2° S of moored time series from the TAO array. Anomalies are relative to monthly climatologies cubic spline fitted to 5-day intervals (COADS winds, Reynolds SST, CTD/XBT 20° C depths).

ENSO transition

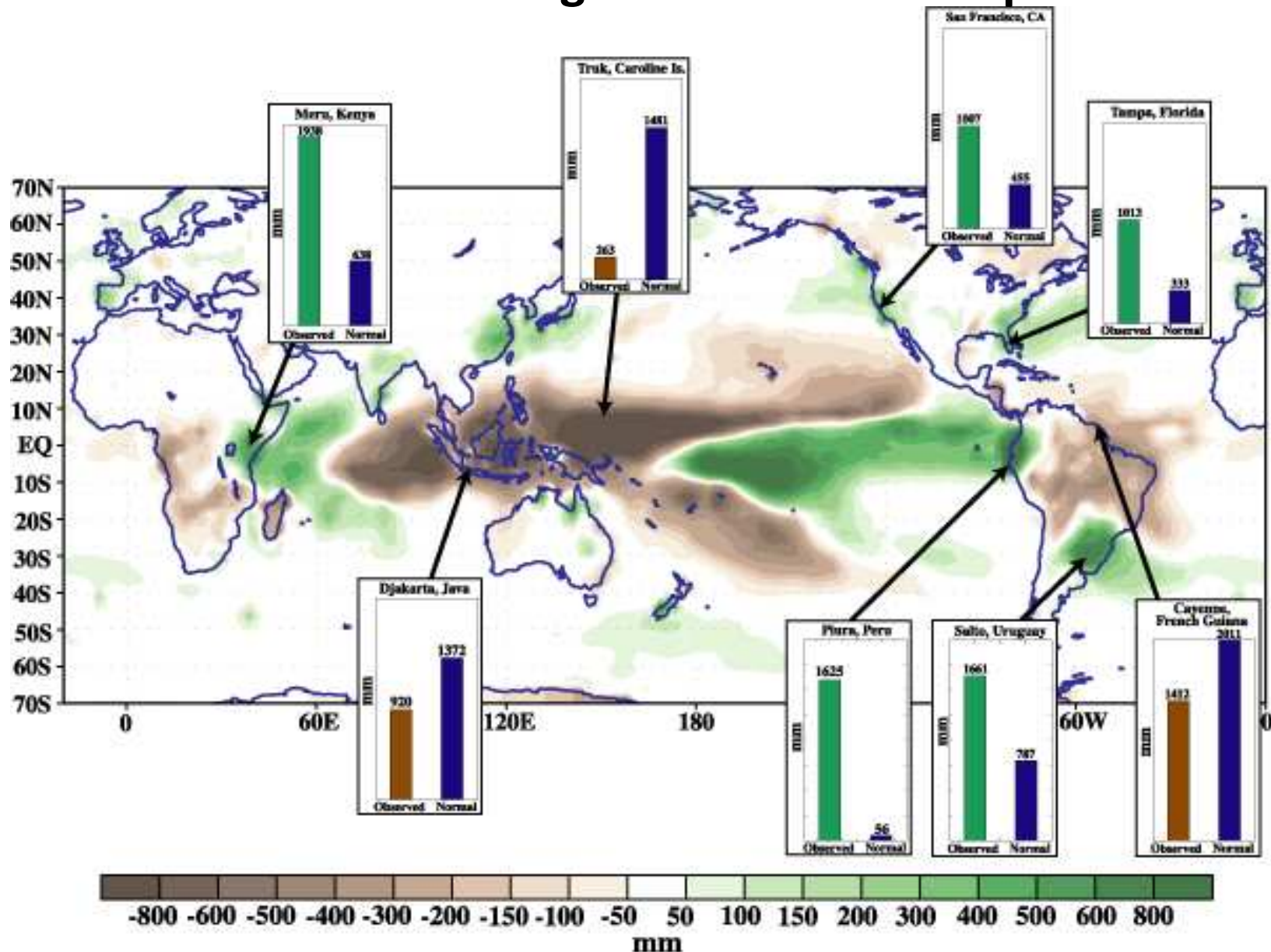


Seasonal SST (left) and anomaly (right) for DJF 1997/98, MAM 1998, JJA 1998, SON 1998. Contour interval is 1° C, with the 0.5° C contour included. Anomalies are departures from the 1950-79 adjusted OI climatology (Reynolds and Smith 1995) (from BAMS, 1999, 80, S1-48)



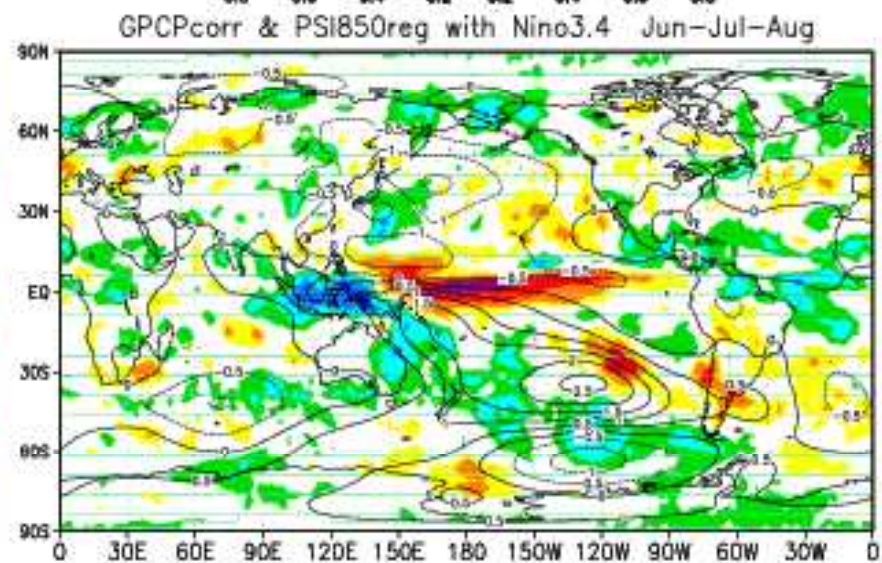
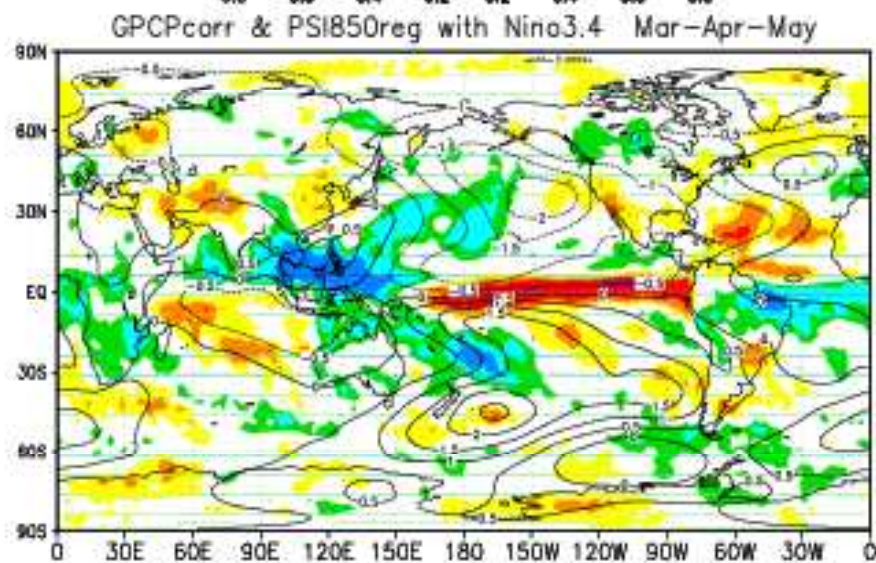
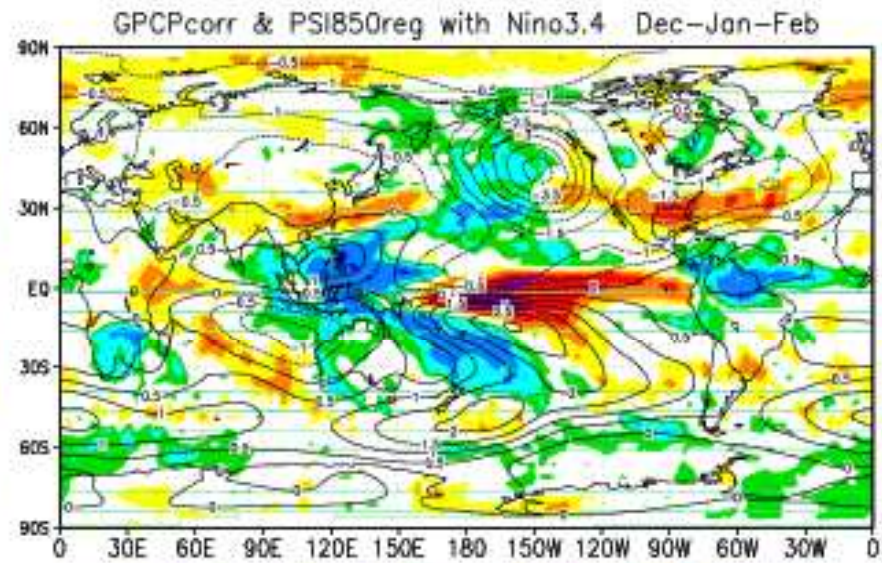
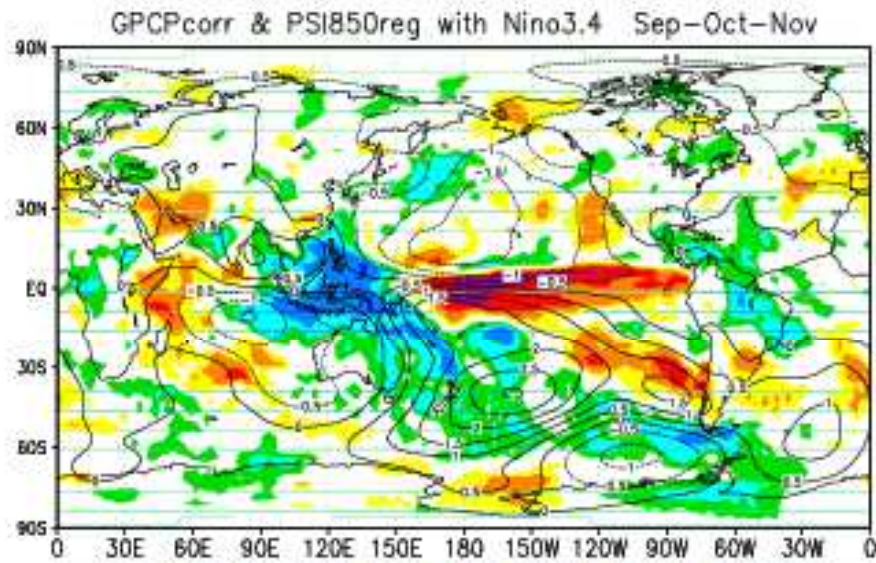
Equatorial depth-longitude section of ocean temperature anomalies. Contour interval is 1(C. The dark line is 20C isotherm. Data are derived from an analysis system that assimilates oceanic observations into an oceanic GCM (Behringer et al. 1998). Anomalies are departures from the 1983-92 base period means.

Rainfall anomalies during November 1997-April 1998

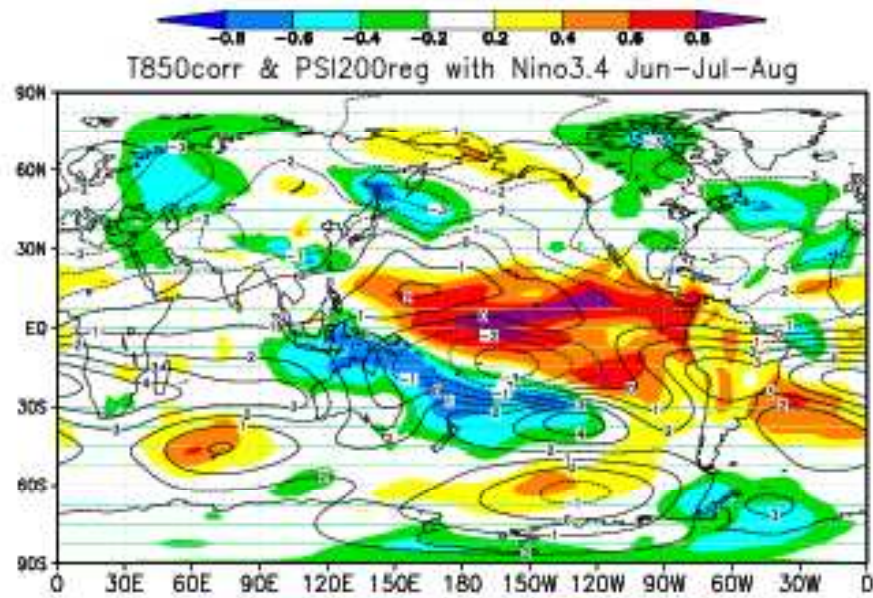
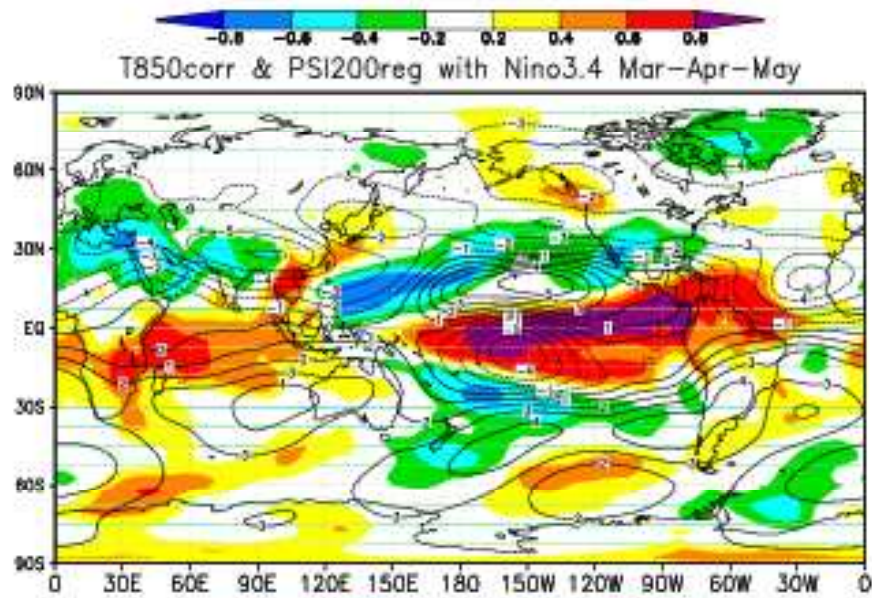
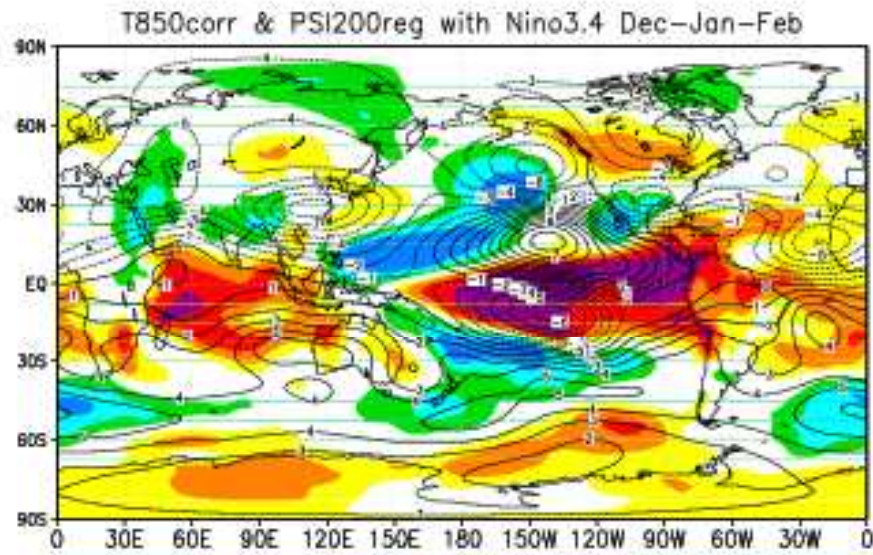
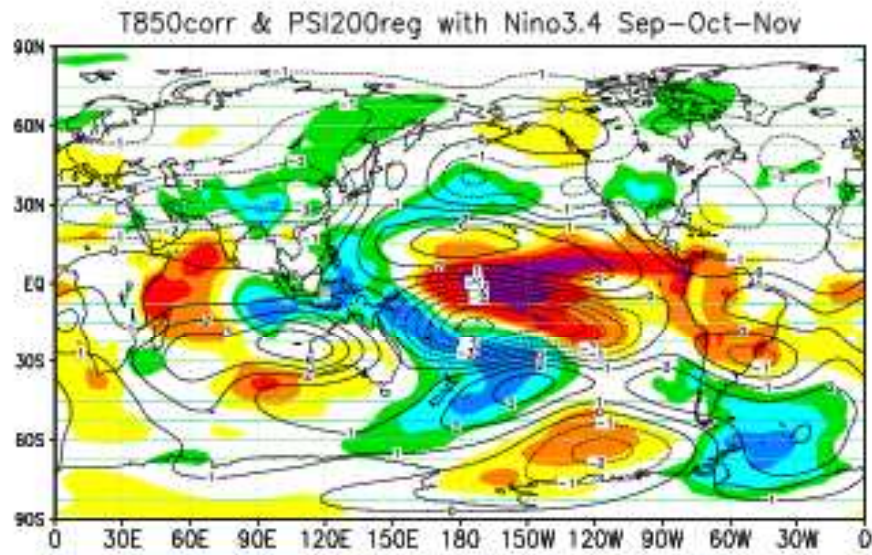


Accumulated rainfall departures during November 1997-April 1998. Precipitation amounts are obtained by merging rain gauge observations and satellite-derived precipitation estimates. The satellite estimates are generated by the outgoing longwave radiation precipitation technique (Xie and Arkin 1998), and are merged with rain gauge data via a method adapted from Xie and Arkin (1996). Anomalies are departures from the 1979-95 base period means (from BAMS, 1999, 80, S1-48).

Correlation coefficient map between Rainfall anomalies and Nino3.4 SST anomaly



Correlation coefficient map between 850hPa temperature anomalies and Nino3.4 SST anomaly



The El Niño with a difference

Karumuri Ashok and Toshio Yamagata

El Niño in a changing climate

Sang-Wook Yeh¹, Jong-Seong Kug¹, Boris Dewitte², Min-Ho Kwon³, Ben P. Kirtman⁴ & Fei-Fei Jin³

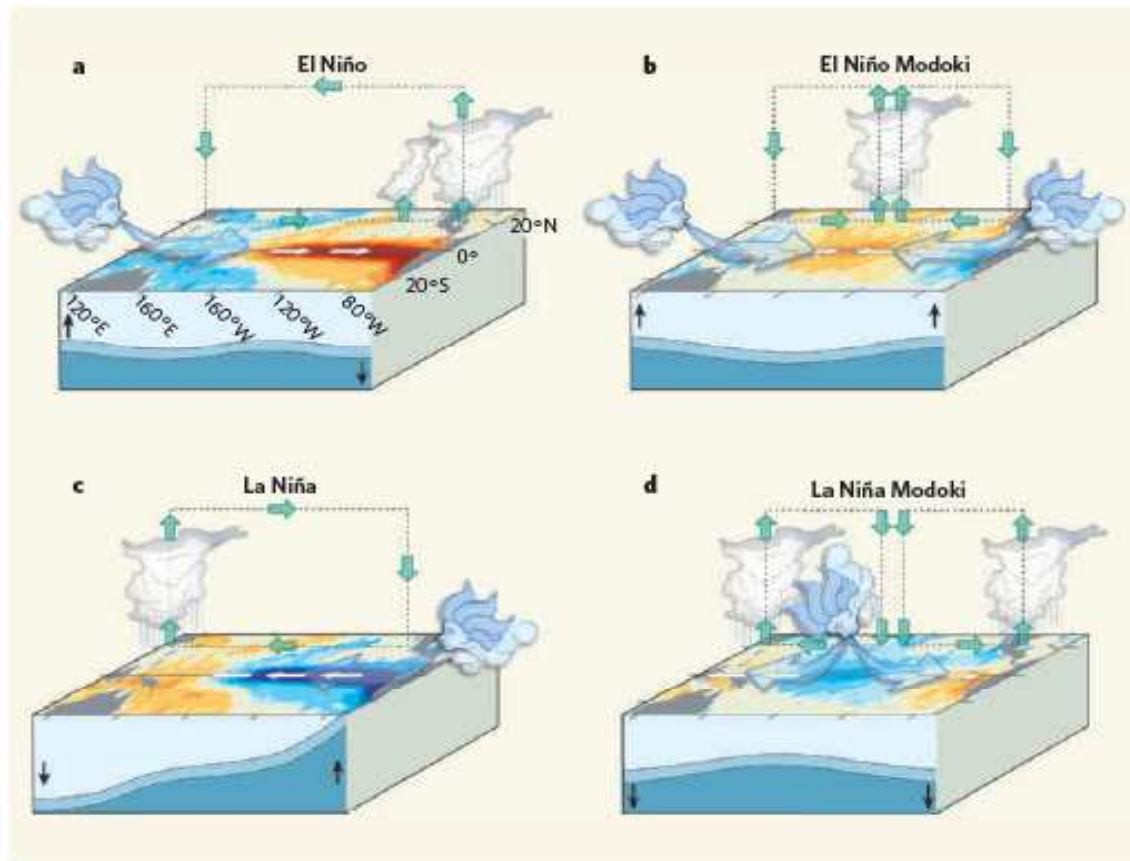


Figure 2 | Anomalous conditions in the tropical Pacific. **a**, An El Niño event is produced when the easterly winds weaken; sometimes, in the west, westerlies prevail. This condition is categorized by warmer than normal sea surface temperatures (SSTs) in the east of the ocean, and is associated with alterations in the thermocline and in the atmospheric circulation that make the east wetter and the west drier. **b**, An El Niño Modoki event is an anomalous condition of a distinctly different kind. The warmest SSTs occur in the central Pacific, flanked by colder waters to the east and west, and are associated with distinct patterns of atmospheric convection. **c**, **d**, The opposite (La Niña) phases of the El Niño and El Niño Modoki respectively. Yeh *et al.*³ argue that the increasing frequency of the Modoki condition is due to anthropogenic warming, and that these events in the central Pacific will occur more frequently if global warming increases.

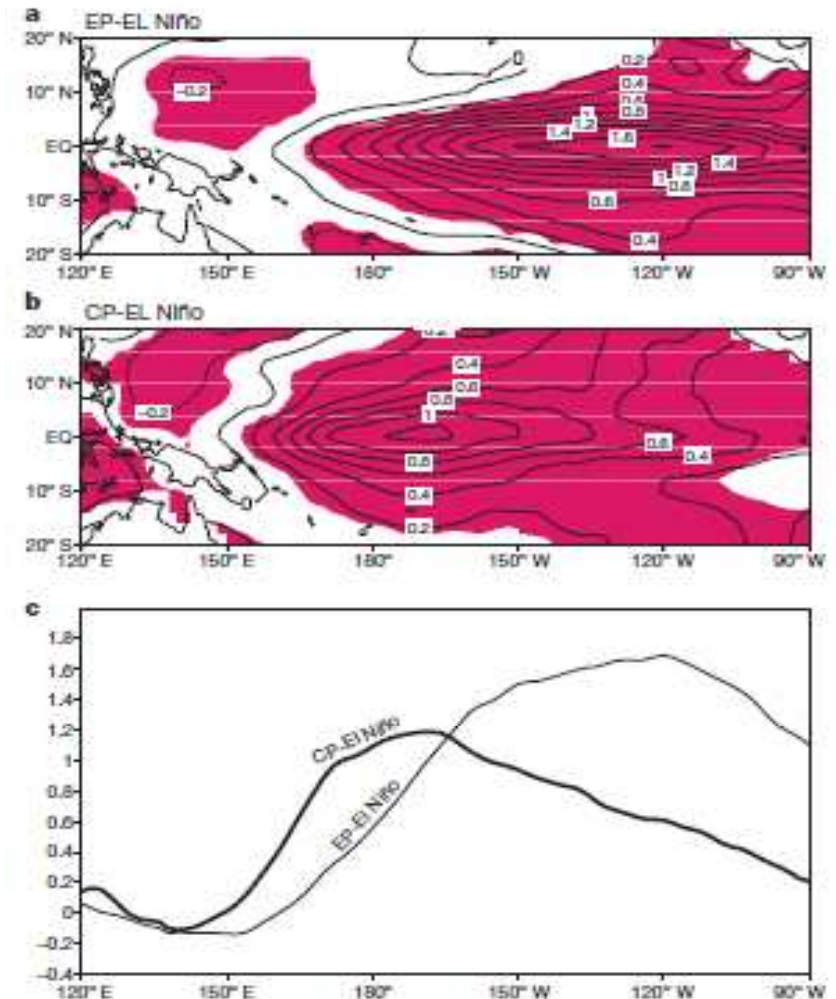


Figure 1 | Deviations of mean SST for the two characteristics of El Niño from the 1854–2006 climatology. **a**, The EP-El Niño; **b**, the CP-El Niño. The contour interval is 0.2 °C and shading denotes a statistical confidence at 95% confidence level based on a Student's *t*-test. **c**, The zonal structure for the composite EP-El Niño (thin line) and CP-El Niño (thick line) averaged over 2°N to 2°S.

A dipole mode in the tropical Indian Ocean

Saji et al., Nature 1999

N. H. Saji*, B. N. Goswami†, P. N. Vinayachandran* & T. Yamagata*‡

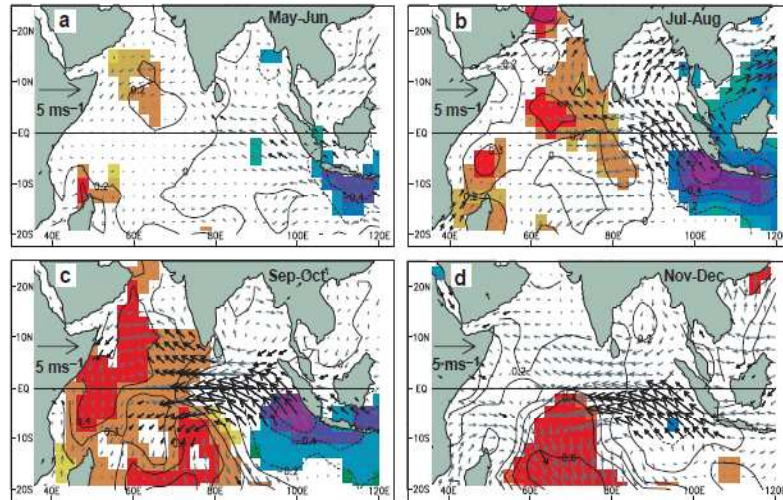


Figure 2 A composite dipole mode event. **a–d**, Evolution of composite SST and surface wind anomalies from May–June (**a**) to Nov–Dec (**d**). The statistical significance of the

analysed anomalies were estimated by the two-tailed *t*-test. Anomalies of SSTs and winds exceeding 90% significance are indicated by shading and bold arrows, respectively.

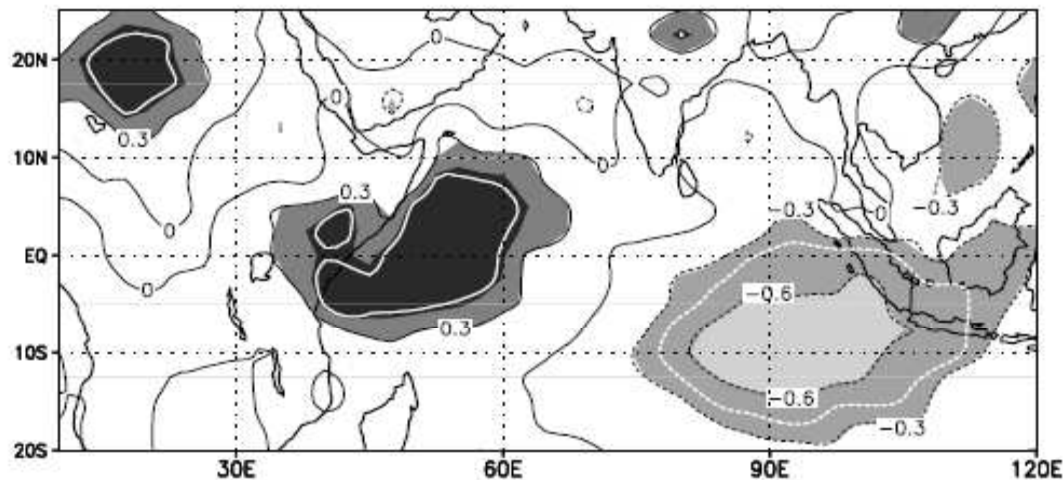


Figure 4 Rainfall shifts northwest of the OTCZ during dipole mode events. The map correlates the DMI and rainfall to illustrate these shifts. The areas within the white curve exceed the 90% level of confidence for non-zero correlation (using a two-tailed *t*-test).

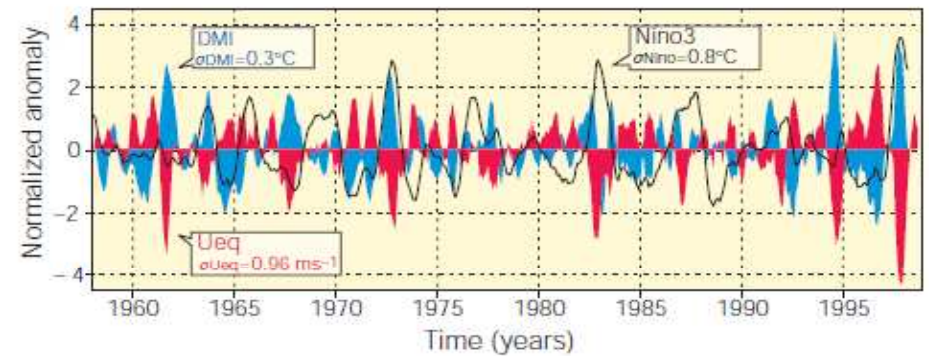


Figure 1 Dipole mode and El Niño events since 1958. Plotted in blue, the dipole mode index (DMI) exhibits a pattern of evolution distinctly different from that of the El Niño, which is represented by the Nino3 sea surface temperature (SST) anomalies (black line). On the other hand, equatorial zonal wind anomalies U_{eq} (plotted in red) coevolves with the DMI. All the three time series have been normalized by their respective standard deviations. We have removed variability with periods of 7 years or longer, based on harmonic analysis, from all the data sets used in this analysis. In addition, we have smoothed the time series using a 5-month running mean.

Possible impacts of Indian Ocean Dipole mode events on global climate

N. H. Saji^{1,3,*}, T. Yamagata^{1,2}

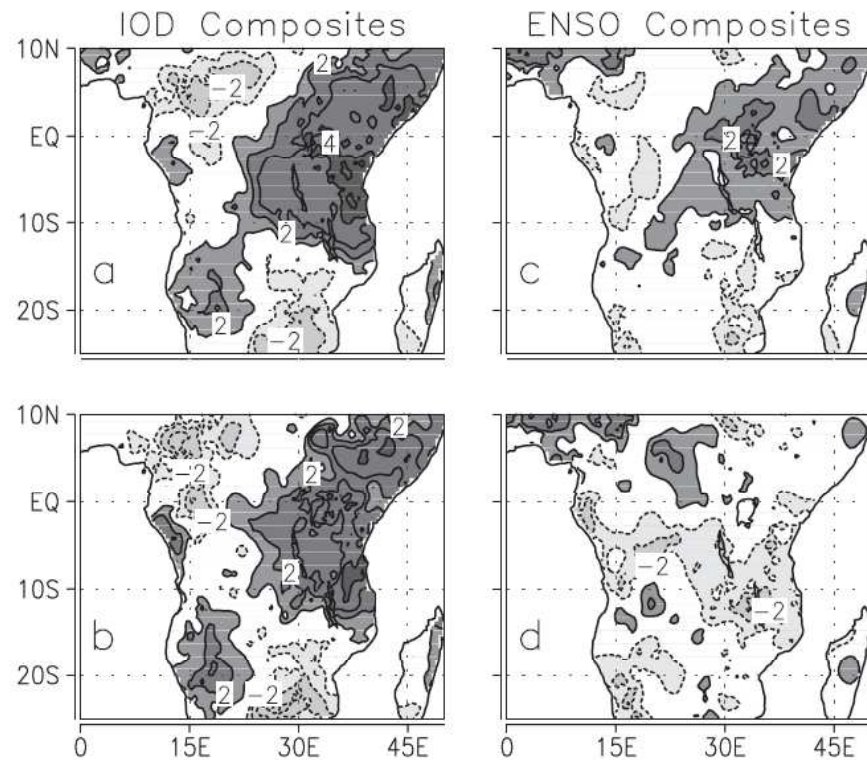


Fig. 1. Composite OND rain anomaly over Africa for (a) 19 IOD events, (b) 11 ENSO-independent IOD events, (c) 20 ENSO events and (d) 12 IOD-independent ENSO events. The composite anomaly was normalized by the standard deviation of rain during OND. Contours given at ± 1 , ± 2 , etc.

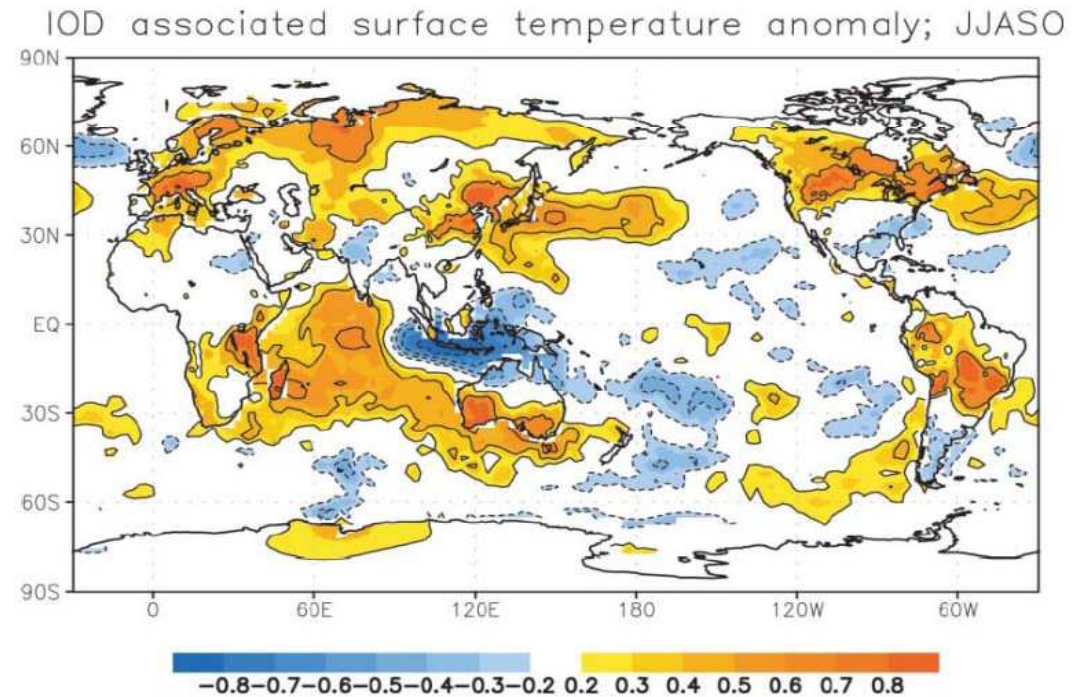


Fig. 21. Partial correlation of land and sea-surface temperature on DMI independent of Nino3 during JJASO

Indian Ocean Capacitor Effect on Indo–Western Pacific Climate during the Summer following El Niño

SHANG-PING XIE,^{*,†} KAIMING HU,[#] JAN HAFNER,^{*} HIROKI TOKINAGA,^{*} YAN DU,^{*,@}
 GANG HUANG,[#] AND TAKEAKI SA[^]MADE^{*}

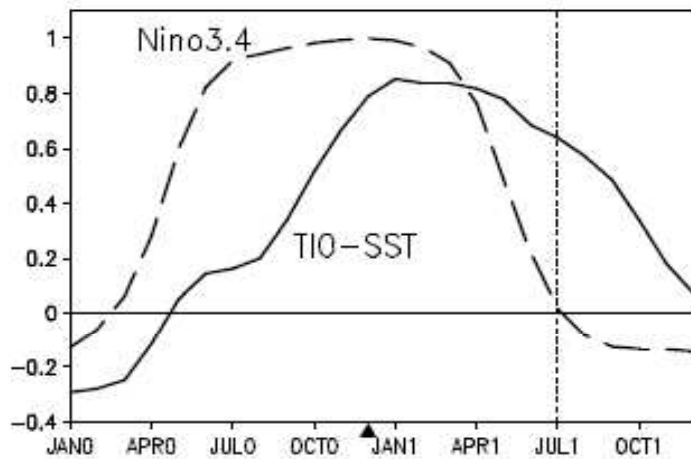


Fig. 1. Correlation of tropical Indian Ocean (40–100°E, 20°S–20°N) SST (solid) with the Niño-3.4 (170°W–120°W, 5°S–5°N) SST index for Nov(0)–Dec(0)–Jan(1). Numerals in parentheses denote years relative to El Niño: 0 for its developing and 1 for decay year. The dashed curve is the Niño-3.4 SST auto-correlation as a function of lag. The black triangle denotes Dec(0), the peak phase of ENSO.

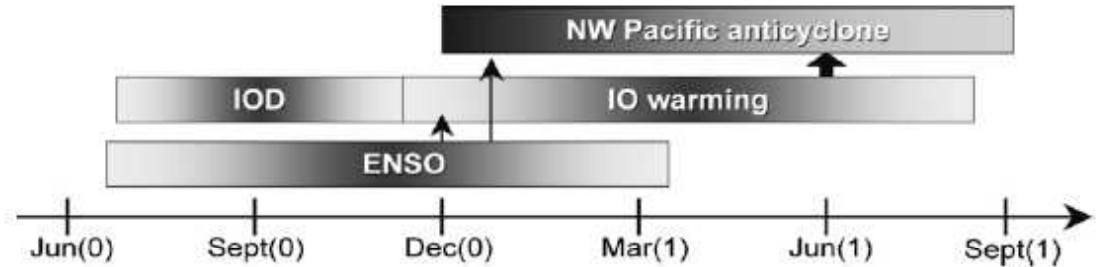


FIG. 13. Seasonality of major modes of Indo–western Pacific climate variability. Vertical arrows indicate causality, and the block arrow emphasizes the TIO capacitor effect, the major finding of the present study.

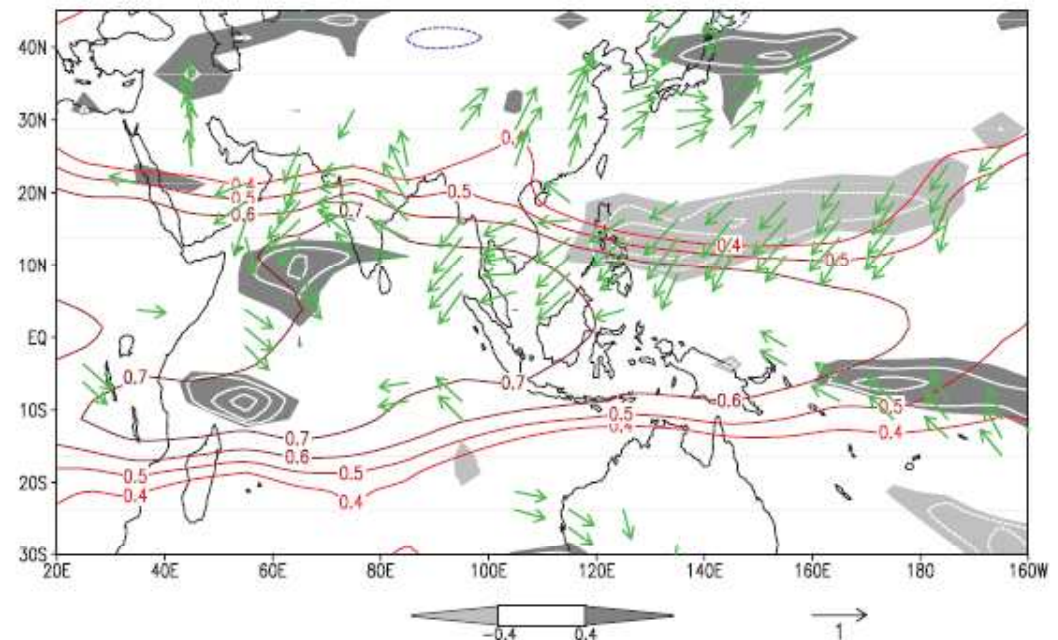


FIG. 6. JJA(1) correlation with the NDJ(0) Niño-3.4 SST index: tropospheric (850–250 hPa) temperature (contours), precipitation (white contours at intervals of 0.1; dark shade > 0.4; light < -0.4), and surface wind velocity (vectors).

Seasonal Forecasting System

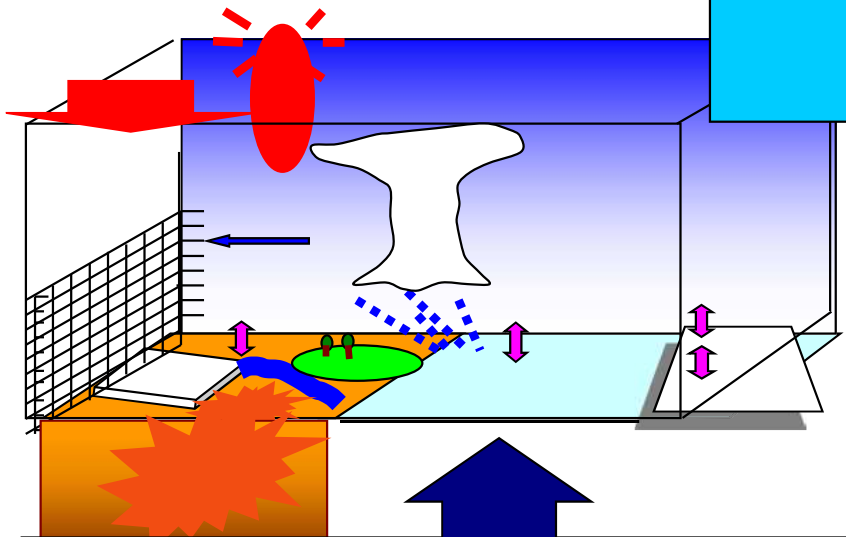
Weather Forecast

Atmosphere-Land
Coupled Model

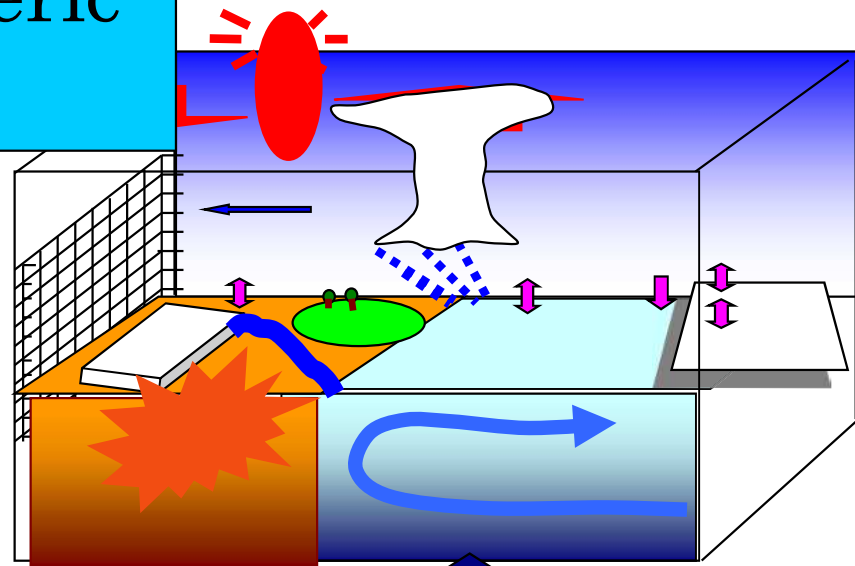
Seasonal Forecast

Atmosphere-Land-Ocean Coupled
Model

Atmospheric
Model

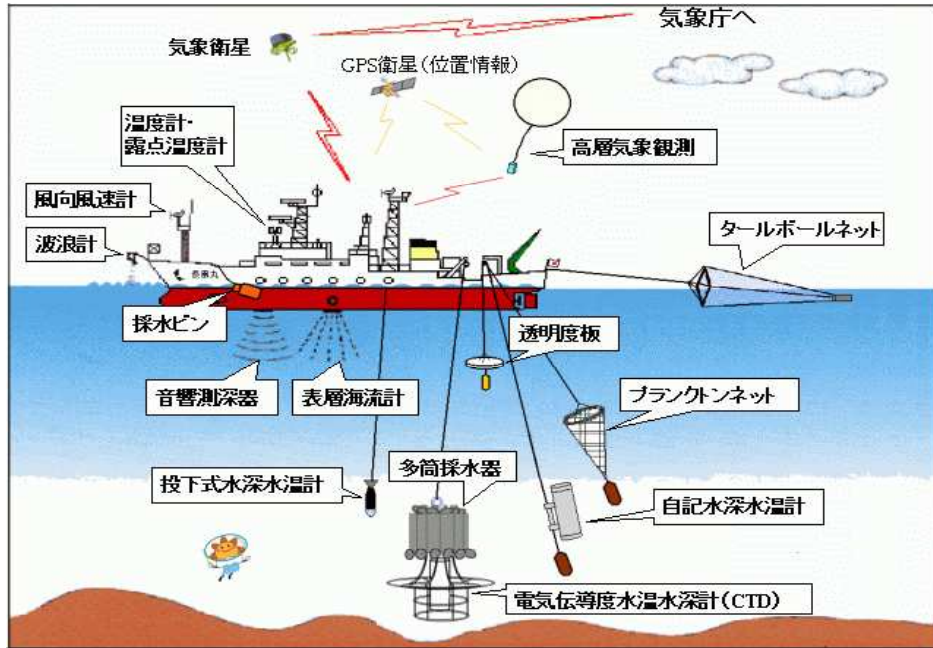


SST Anomaly
is prescribed as boundary



Ocean model is coupled

<http://www.fukuoka-jma.go.jp/nagasaki/kaiyo/kansoku/index.html#XBT>

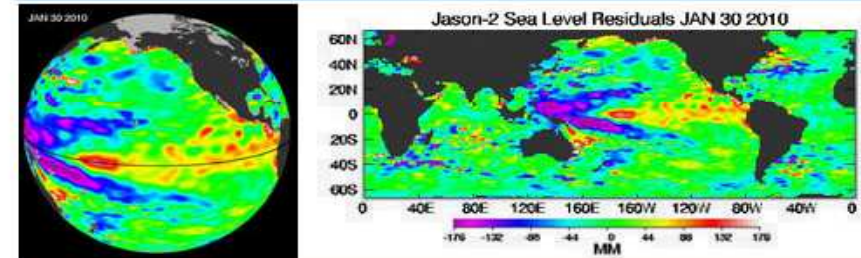


<http://topex-www.jpl.nasa.gov/science/jason1-quick-look/2009/20091201.html>

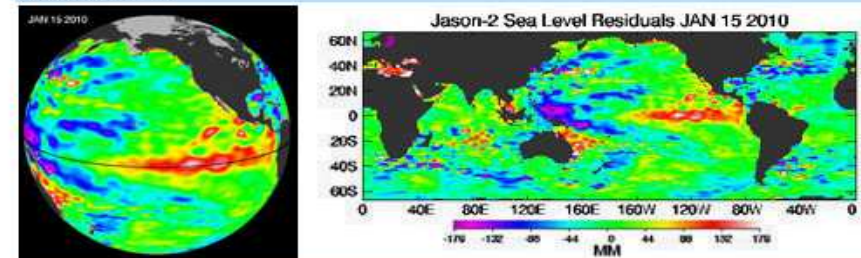
SCIENCE - El Niño/La Niña & PDO

Latest El Niño/La Niña Jason Data

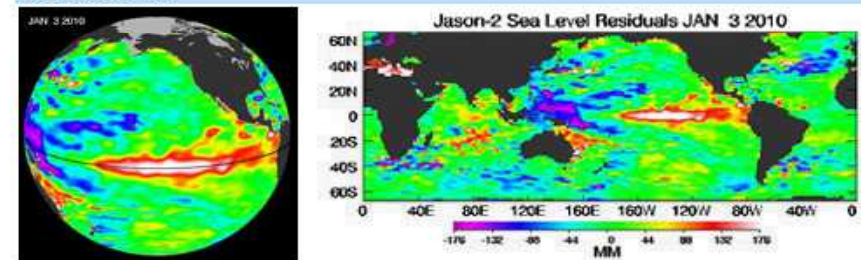
LATEST IMAGES - 01/30/2010



01/15/2010



01/03/2010



These are the latest images from the OSTM/Jason-2 satellite. Jason-2 continues providing the uninterrupted time-series that originated with TOPEX/Poseidon. Jason is using radar altimetry to collect sea surface height data of all the world's oceans. These images are processed to highlight the interannual signal of sea surface height. The mean signal, seasonal signal, and the trend have been removed.

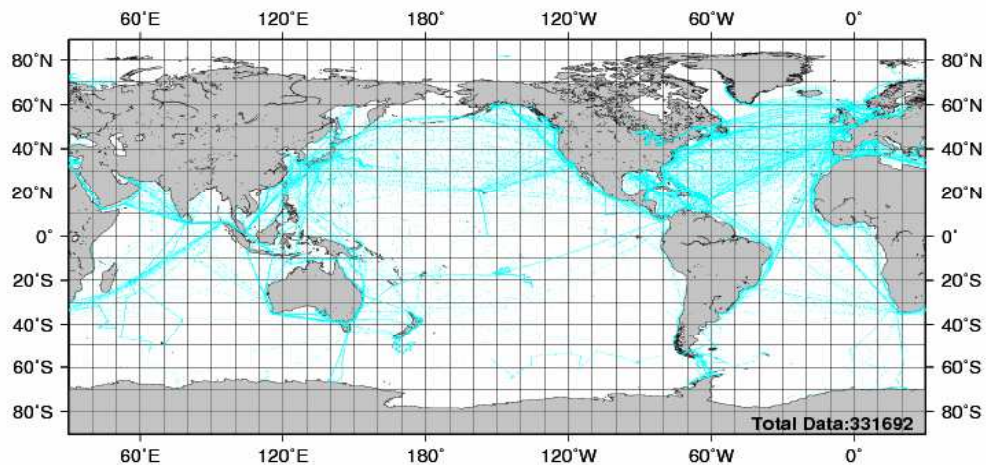
Image Archive (last 10 Images)

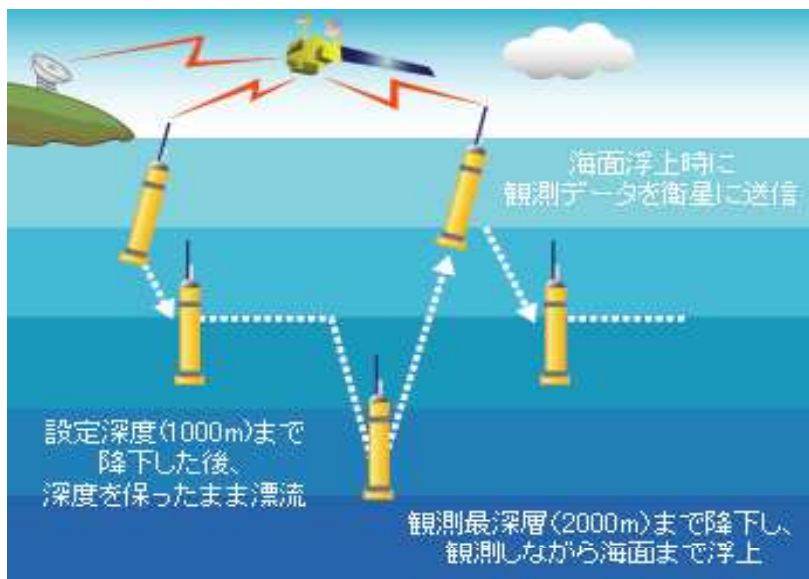
観測通報点分布図

2008年 12月 選択

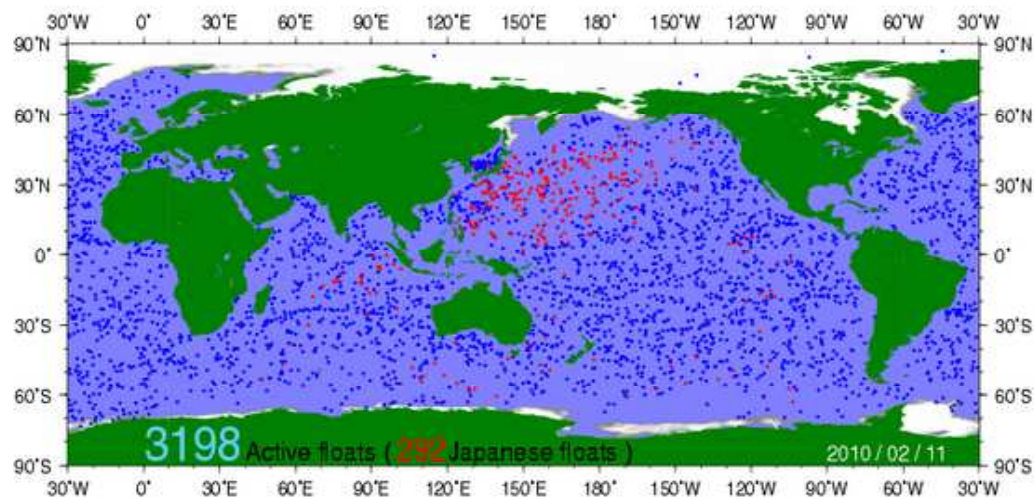
<http://www.data.kishou.go.jp/kaiyou/db/kaiyo/etc/stnplot.html>

- SHIP (海上気象実況通報式)
- BATHY・TESAC (表層水温観測・海洋観測通報式)
- BUOY (ブイ観測通報式)
- TRACKOB (航路海面観測通報式)





アルゴフロートの動作サイクル概念図



アルゴフロート投入内訳 (2010-02-11 現在)

投入国等	アメリカ	日本	オーストラリア	ドイツ	フランス	カナダ	イギリス	韓国	インド	中国	EU	その他	合計
稼働数	1805	292	233	179	156	117	106	102	70	33	14	91	3198

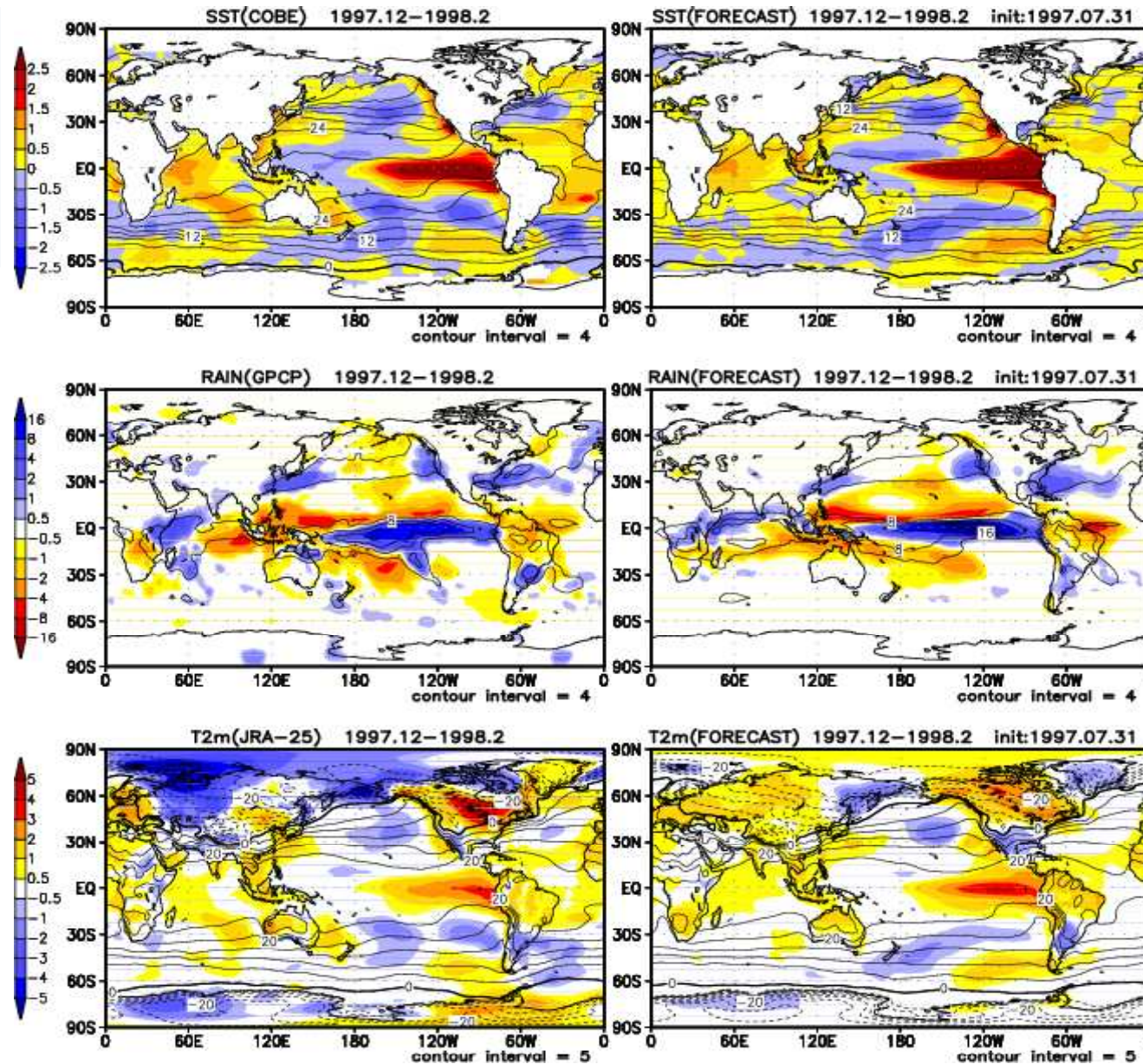
Current Seasonal Forecast is based on El Nino Predictability. (An Example of Four-month-lead Seasonal Prediction)

**Observation
(3-month
Average
from Dec. 1997
to Feb. 1998)**

SST Anomaly

**Precipitation
Anomaly**

**Surface Air
Temperature
Anomaly**

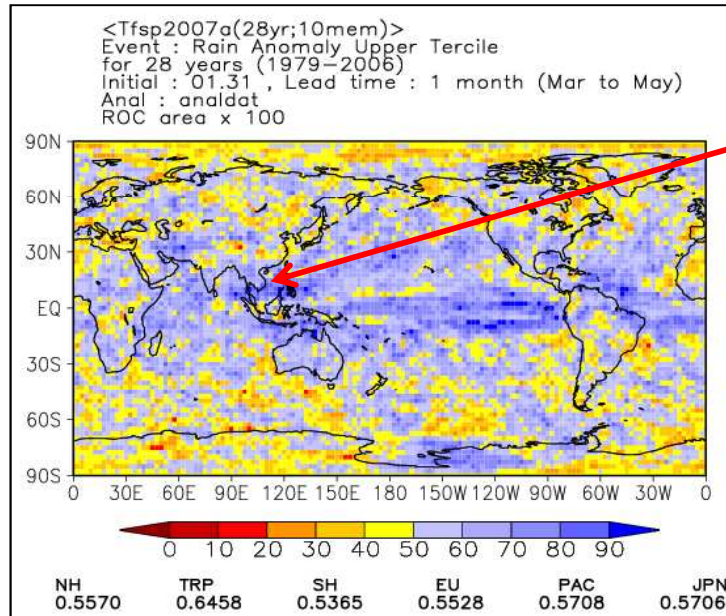


**Model Prediction
from Initials
On 31 Jul. 1997**

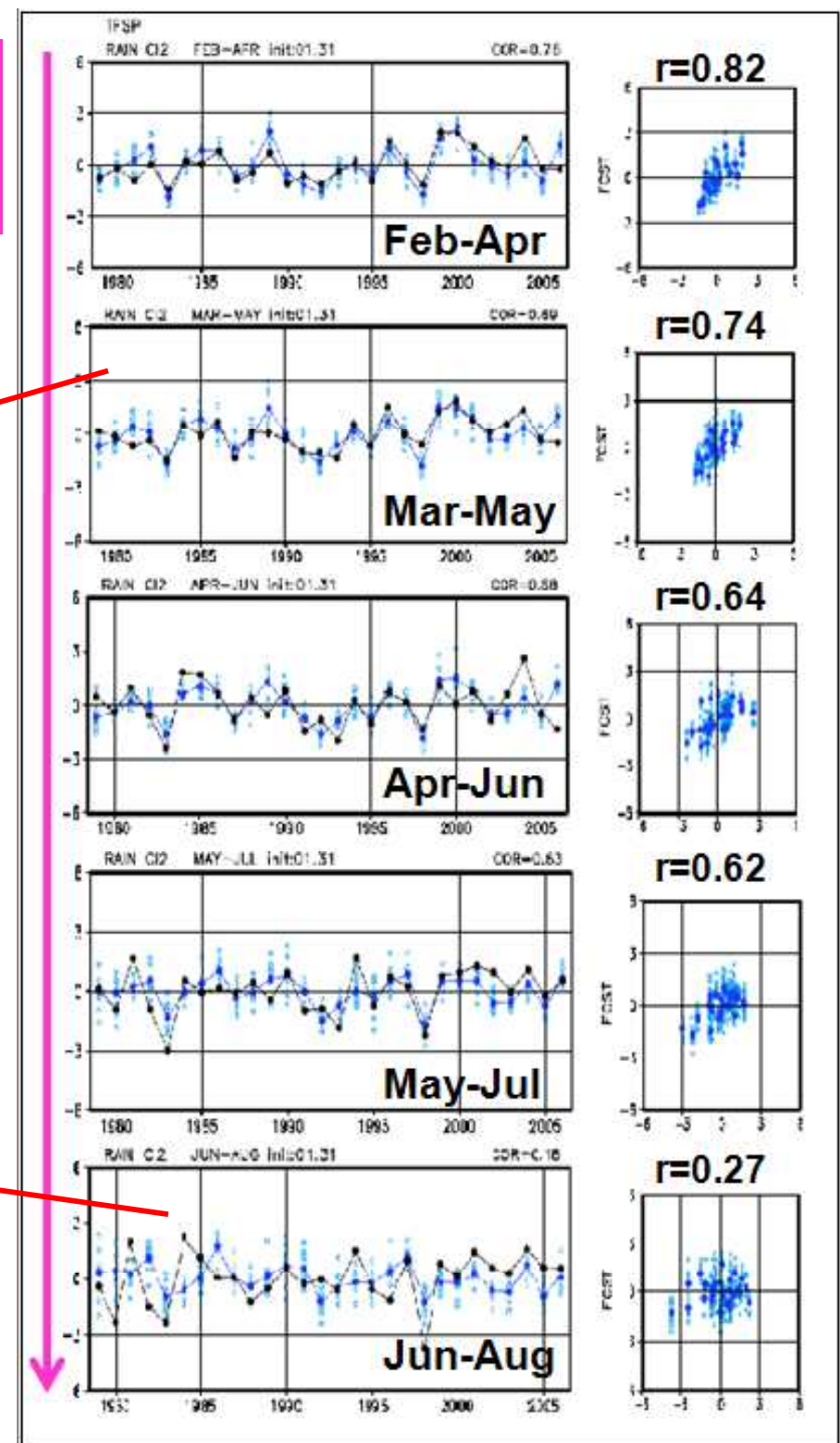
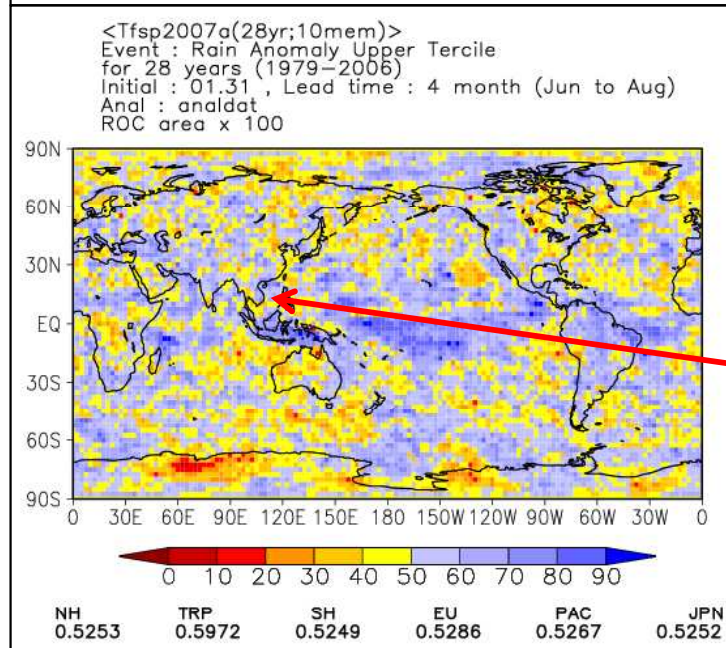
**Four-
month
Lead
Forecast**

Precipitation predictions from the initials of Jan 31 over Southeast Asia (115-140E, 10-20N)

ROC skill scores
for upper tercile of
precipitation
prediction in Mar-
May
from the initials of
Jan 31.



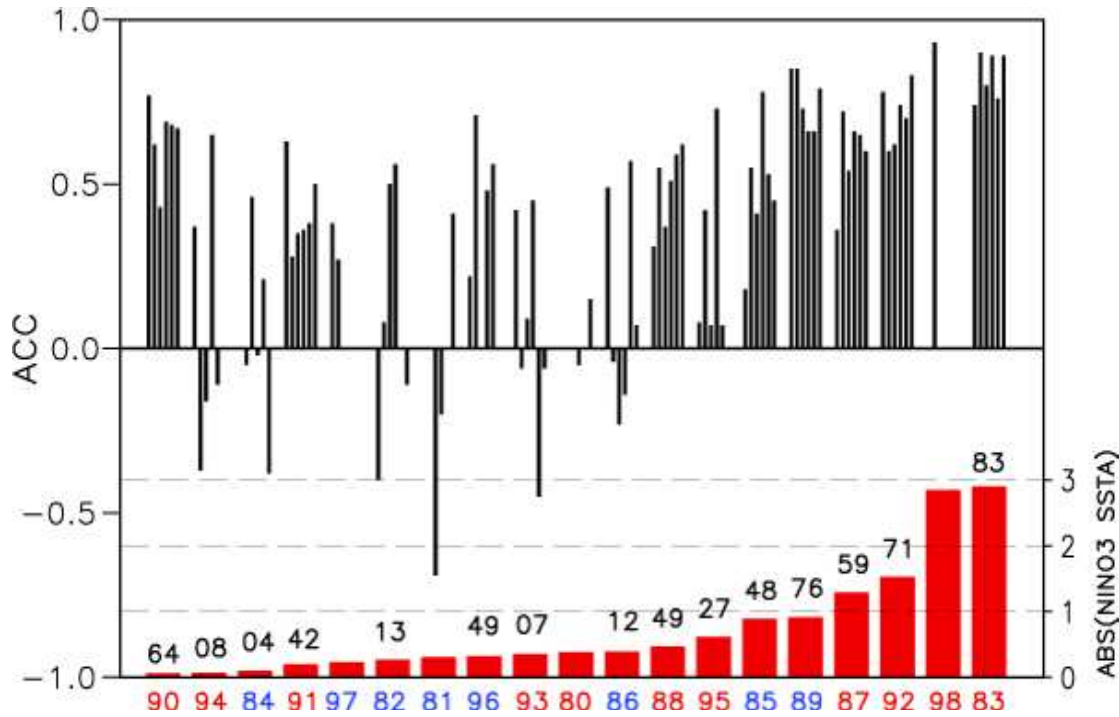
ROC skill scores
for upper tercile of
precipitation
prediction in Jun-
Aug
from the initials of
Jan 31.



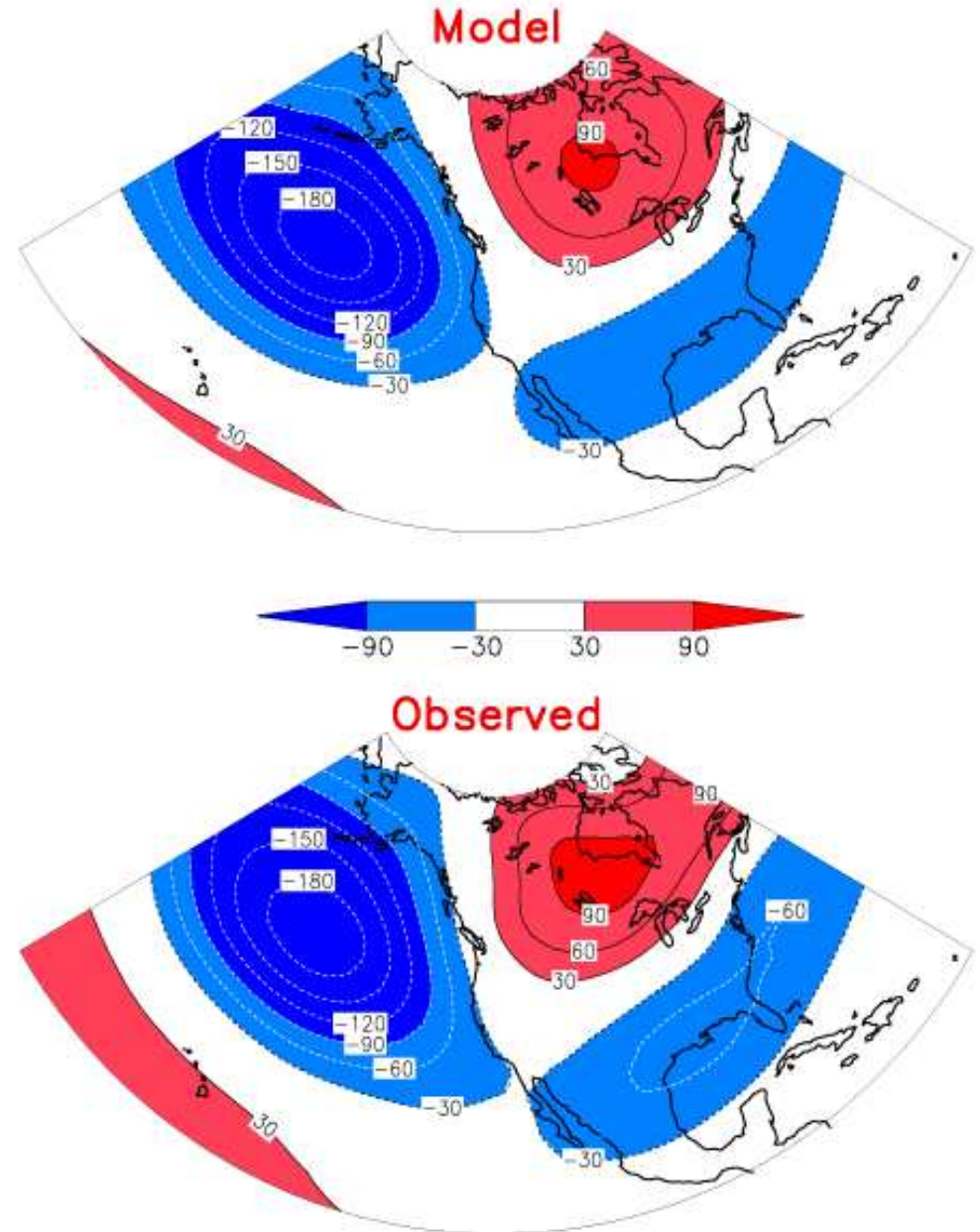
Dynamical Seasonal Prediction

Model Simulation of ENSO Effects
500 hPa height (meters) anomalies

ACC from ensemble mean JFM Z500 over PNA region and absolute value of Nino-3 SST anomalies

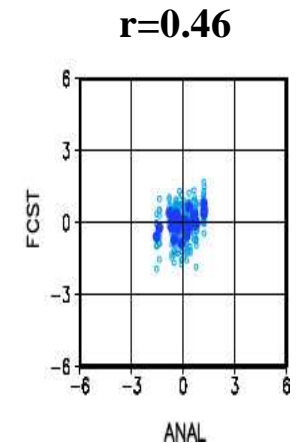
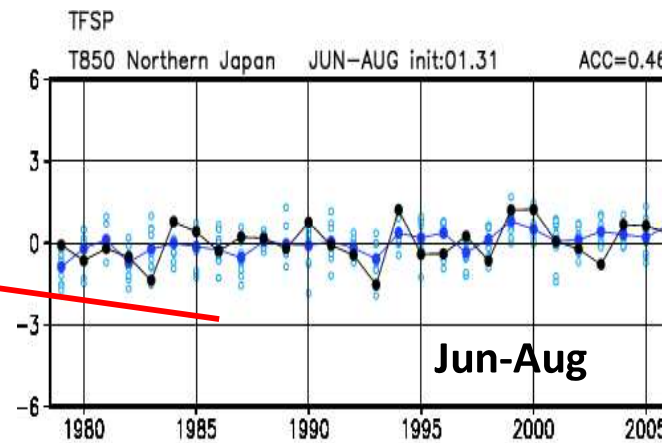
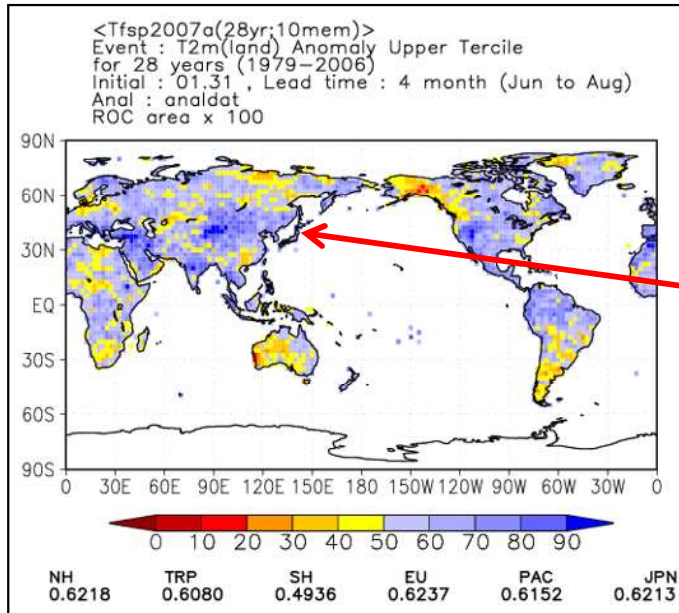


Overall, the model performance is better for larger signals.

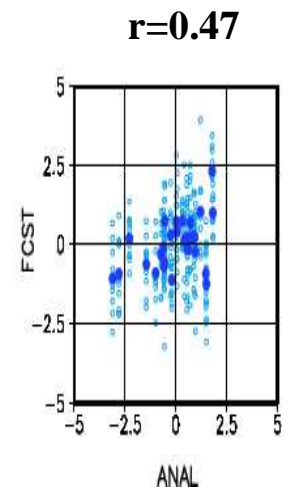
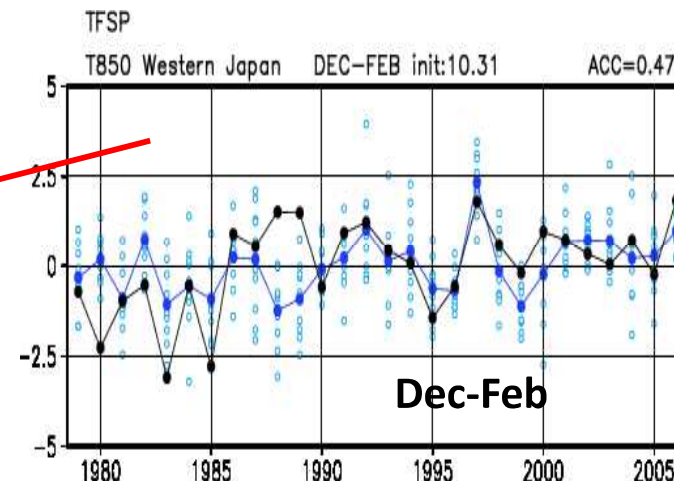
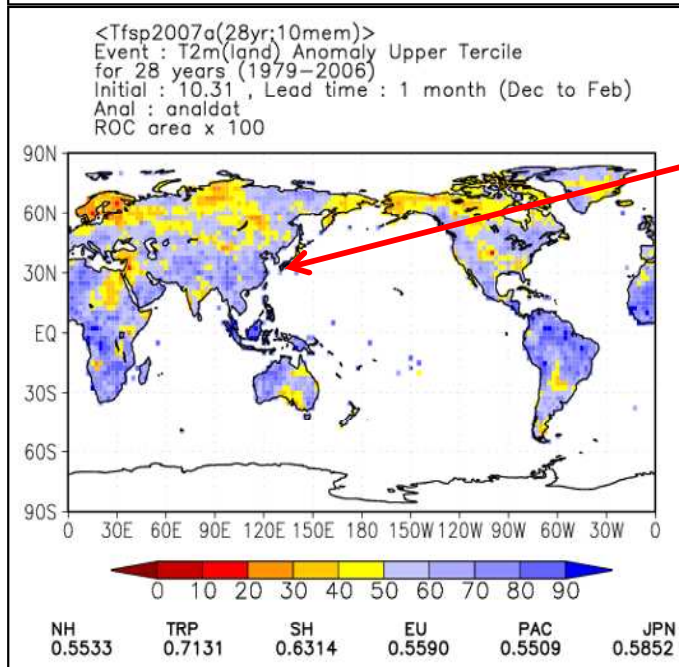


Surface air temperature over land predictions over Japan

ROC skill scores for upper tercile of surface air temperature over land prediction in Jun-Aug from the initials of Jan 31.



ROC skill scores for upper tercile of surface air temperature over land prediction in Dec-Feb from the initials of Oct 31.



DEVELOPMENT OF A EUROPEAN MULTIMODEL ENSEMBLE SYSTEM FOR SEASONAL-TO-INTERANNUAL PREDICTION (DEMETER)

BAMS, 2004, P.853-872

BY T. N. PALMER, A. ALESSANDRI, U. ANDERSEN, P. CANTELAUBE, M. DAVEY, P. DÉLÉCLUSE, M. DÉQUÉ, E. DÍEZ, F. J. DOBLAS-REYES, H. FEDDERSEN, R. GRAHAM, S. GUALDI, J.-F. GUÉRÉMY, R. HAGEDORN, M. HOSHEN, N. KEENLYSIDE, M. LATIF, A. LAZAR, E. MAISONNAVE, V. MARLETTO, A. P. MORSE, B. ORFILA, P. ROGEL, J.-M. TERRES, M. C. THOMSON

AFFILIATIONS: PALMER, DOBLAS-REYES, AND HAGEDORN—European Centre for Medium-Range Weather Forecasts, Reading, United Kingdom; ALESSANDRI AND GUALDI—Istituto Nazionale de Geofisica e Vulcanologia, Bologna, Italy; ANDERSEN AND FEDDERSEN—Danmarks Meteorologiske Institut, Copenhagen, Denmark; CANTELAUBE AND TERRES—Land Management Unit, Institute for Environment and Sustainability, Joint Research Centre, Ispra, Italy; DAVEY AND GRAHAM—Met Office, Bracknell, United Kingdom; DÉLÉCLUSE AND LAZAR—Laboratoire d’Océanographie Dynamique et de Climatologie, Paris, France; DÍEZ AND GUÉRÉMY—Centre National de Recherches Météorologiques, Météo-France, Toulouse, France; DIEZ AND ORFILA—Istituto Nazionale de Meteorologia, Madrid, Spain; HOSHEN AND MORSE—Department of Geography, University of Liverpool, Liverpool, United Kingdom; KEENLYSIDE AND LATIF—Max-Planck Institut für Meteorologie, Hamburg, Germany; MAISONNAVE AND ROGEL—European Centre for Research and Advanced Training in Scientific Computation, Toulouse, France; MARLETTO—Agenzia Regionale Prevenzione Ambiente dell’Emilia Romagna, Bologna, Italy; THOMSON—International Research Institute for Climate Prediction (IRI), The Earth Institute at Columbia University, Columbia University, New York, New York
CORRESPONDING AUTHOR: Dr. T. N. Palmer, ECMWF, Shinfield Park, RG2 9AX, Reading, United Kingdom
 E-mail: t.palmer@ecmwf.int
 DOI: 10.1175/BAMS-85-6-853
 In final form 24 November 2003
 ©2004 American Meteorological Society

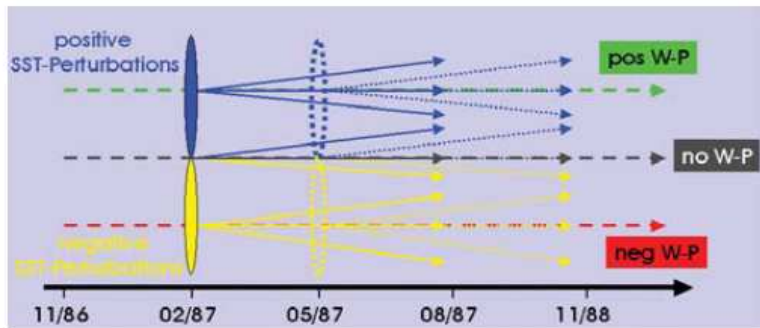


FIG. 1. Schematic representation of the ensemble generation and hindcast production strategy. Dashed lines represent the three continuous runs of ocean analyses forced by ERA-40 data, the control analysis without any wind stress perturbations (gray) and two additional analyses with positive/negative (green/red) daily wind stress perturbations applied. In order to generate nine different initial conditions for the coupled hindcasts, four SST perturbations (represented by the ellipses) are added (blue ellipse) and subtracted (yellow ellipse) to the ocean analyses. Thus, there is one member with no wind stress or SST perturbations applied and eight perturbed ensemble members. This procedure is performed every 3 months at every start date of the hindcasts.

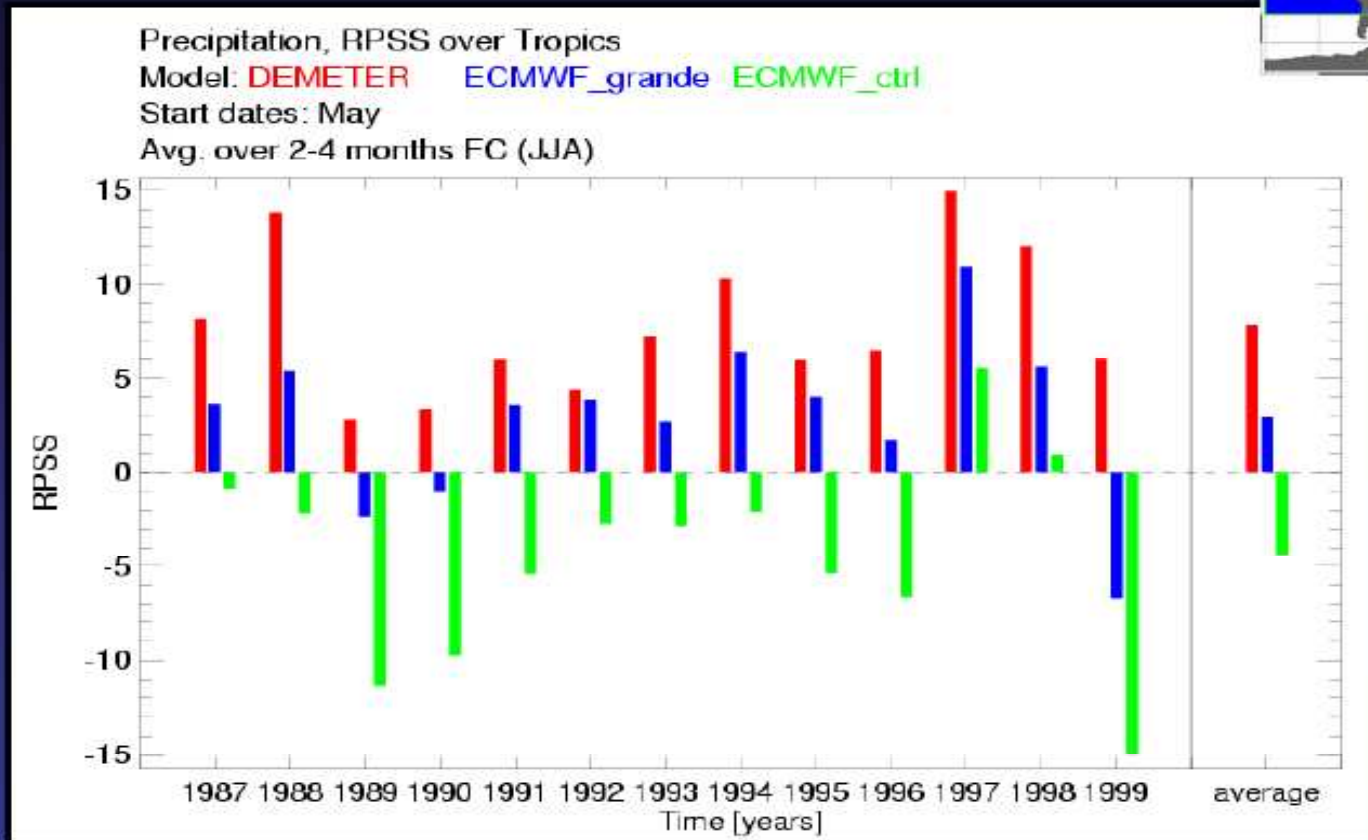
TABLE 1. Combinations of atmosphere and ocean models used by the seven partners contributing with coupled models to DEMETER. The resolution of the models and the initialization strategy are outlined as well. The modeling partners are CERFACS (European Centre for Research and Advanced Training in Scientific Computation, France), ECMWF (European Centre for Medium-Range Weather Forecasts, International Organization), INGV (Istituto Nazionale de Geofisica e Vulcanologia, Italy), LODYC (Laboratoire d’Océanographie Dynamique et de Climatologie, France), Météo-France (Centre National de Recherches Météorologiques, Météo-France, France), Met Office (United Kingdom), and MPI (Max-Planck Institut für Meteorologie, Germany).

	CERFACS	ECMWF	INGV	LODYC	Météo-France	Met Office	MPI
Atmosphere component	ARPEGE	IFS	ECHAM-4	IFS	ARPEGE	HadAM3	ECHAM-5
Resolution	T63 31 levels	T95 40 levels	T42 19 levels	T95 40 levels	T63 31 levels	2.5 × 3.75 19 levels	T42 19 levels
Atmosphere initial conditions	ERA-40	ERA-40	Coupled AMIP-type experiment	ERA-40	ERA-40	ERA-40	Coupled run relaxed to observed SSTs
Reference	Déqué (2001)	Gregory et al. (2000)	Roedner (1996)	Gregory et al. (2000)	Déqué (2001)	Pope et al. (2000)	Roedner (1996)
Ocean component	OPA 8.2	HOPE-E	OPA 8.1	OPA 8.2	OPA 8.0	GloSea OGCM, based on HadCM3	MPI-OM1
Resolution	2.0° × 2.0° 31 levels	1.4° × 0.3°–1.4° 29 levels	2.0° × 0.5°–1.5° 31 levels	2.0° × 2.0° 31 levels	182 GP × 152 GP 31 levels	1.25° × 0.3°–1.25° 40 levels	2.5° × 0.5°–2.5° 23 levels
Ocean initial conditions	Ocean analyses forced by ERA-40	Ocean analyses forced by ERA-40	Ocean analyses forced by ERA-40	Ocean analyses forced by ERA-40	Ocean analyses forced by ERA-40	Ocean analyses forced by ERA-40	Coupled run relaxed to observed SSTs
Reference	Delecluse and Madec (1999)	Wolff et al. (1997)	Madec et al. (1998)	Delecluse and Madec (1999)	Madec et al. (1997)	Gordon et al. (2000)	Marsland et al. (2003)
Ensemble generation	Wind stress and SST perturbations	Wind stress and SST perturbations	Wind stress and SST perturbations	Wind stress and SST perturbations	Wind stress and SST perturbations	Wind stress and SST perturbations	Nine different atmospheric conditions from the coupled initialization run (lagged method)

European DEMETER Project

Impact of ensemble size: Precip (JJA)

Multi-model (54 members) single model (54) single model (9)



APCN Symposium



7 October 2003

Multi-model ensemble skill out-performs single model ensemble with the same member size

RPSS: Rank Probability Skill Score (Wilks 1995)

From ECMWF Web Page

Malaria early warnings based on seasonal climate forecasts from multi-model ensembles

M. C. Thomson¹, F. J. Doblas-Reyes², S. J. Mason¹, R. Hagedorn², S. J. Connor¹, T. Phindela³, A. P. Morse⁴ & T. N. Palmer²

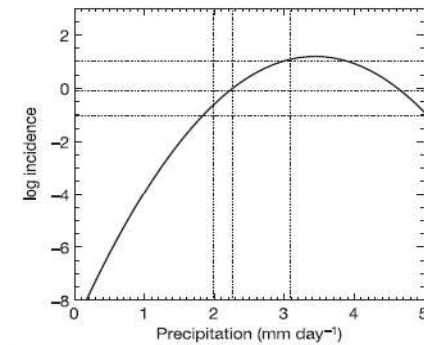


Figure 3 | Relationship between standardized log malaria annual incidence and summer precipitation for Botswana. Standardized log malaria annual incidence (per 1,000 population) versus November–February CMAP precipitation for the period 1982–2002 as obtained from fitting a quadratic function to observations⁴. The quadratic function is $y = -8.9 + 5.9x - 0.8x^2$, where x denotes precipitation (measured in mm day^{-1}) and y the standardized log malaria incidence index. The horizontal and vertical dotted lines denote the quartiles of the standardized log malaria incidence index, and precipitation, respectively.

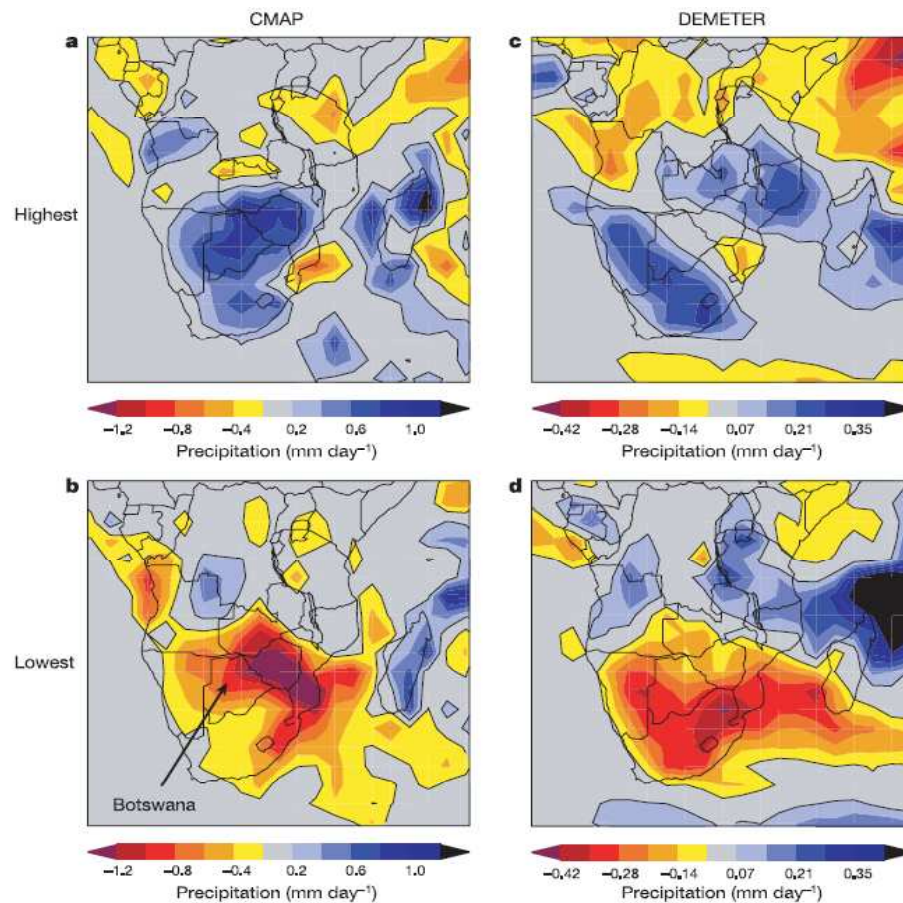


Figure 2 | Composites of austral summer precipitation for central and southern Africa as a function of the standardized malaria annual incidence for Botswana. Mean precipitation anomalies for the five years with the highest (a, c) and lowest (b, d) malaria annual incidence in Botswana for November–February CMAP (a, b) and DEMETER (c, d) ensemble-mean

precipitation. A different colour scale was used for the observed (CMAP) and re-forecast (DEMETER) precipitation because of the unavoidable reduction in amplitude of the predicted anomalies when averaging the 27 ensemble members.

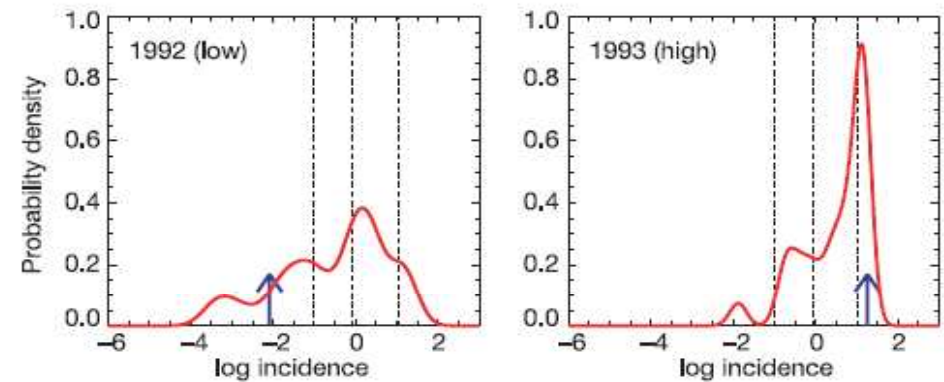
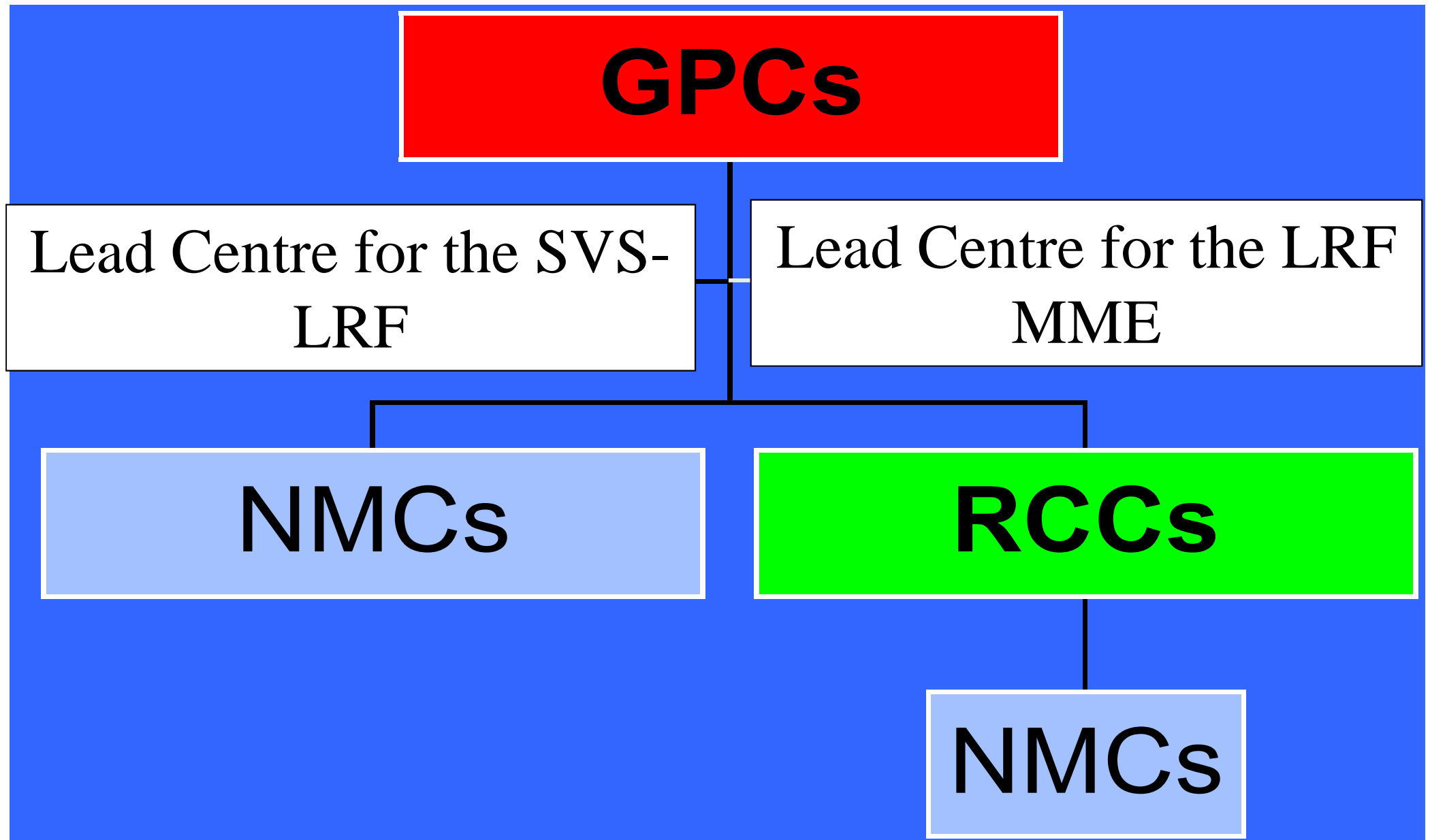


Figure 4 | Forecast probability distribution function of standardized log malaria annual incidence for Botswana. The probability distribution functions of predicted standardized log malaria annual incidence for the years 1992 (anomalously low incidence, left) and 1993 (anomalously high incidence, right) computed with the DEMETER multi-model ensemble forecast system are depicted in red. The vertical dashed lines denote the quartiles of the distribution of the standardized log malaria incidence index and the vertical blue arrows indicate the values recorded by the Botswana Ministry of Health.

WMO Long-Range Forecasts (LRF) Centres



JJA forecasts (Precip) init: May

lon: -30 to 390
lat: -40 to 60

GPCP Beijing
lat=-40 60
lon=-30 390
lev=0
Precipitation : JJA2012

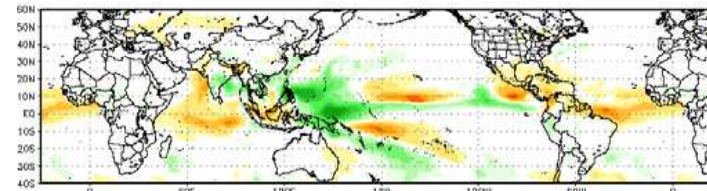
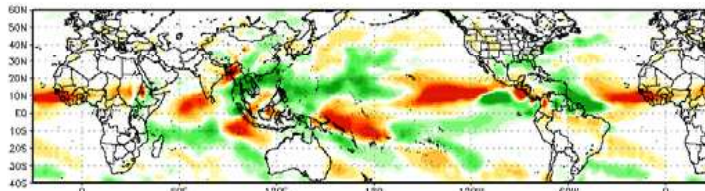
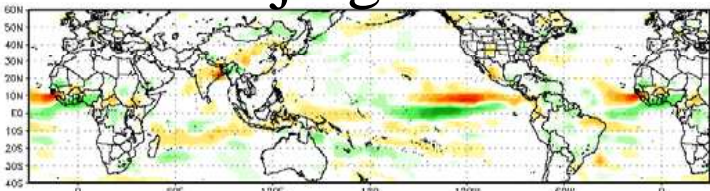
GPCP CPTC
lat=-40 60
lon=-30 390
lev=0
Precipitation : JJ, 2012

ECMWF
lat=-40 60
lon=-30 390
lev=0
Precipitation : JJA2012

From WMO Lead Centre
<http://www.wmo.int>
Downloaded on May 17, 2012

CPTEC

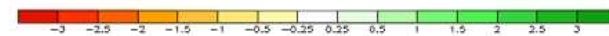
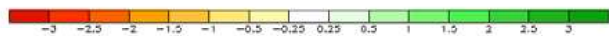
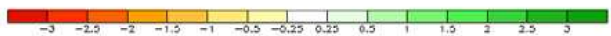
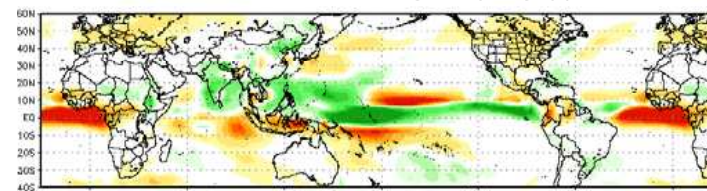
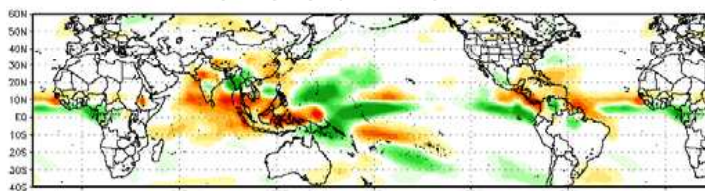
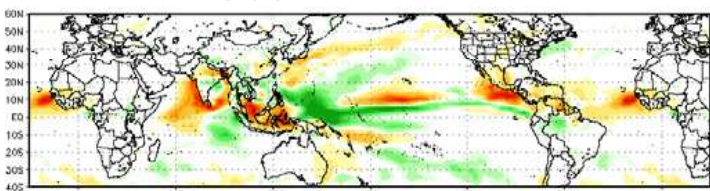
ECMWF



Exeter

Melbourne

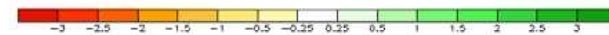
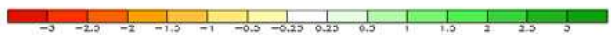
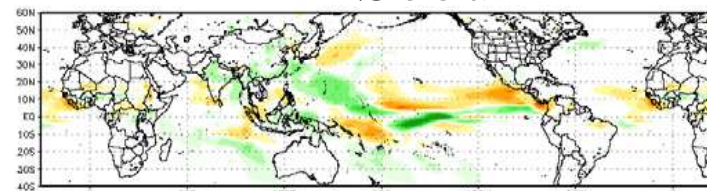
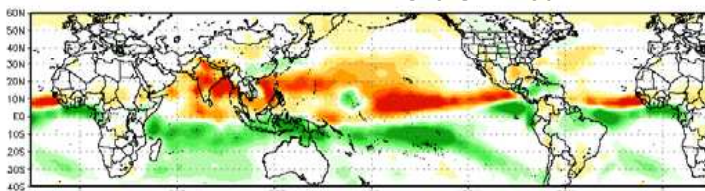
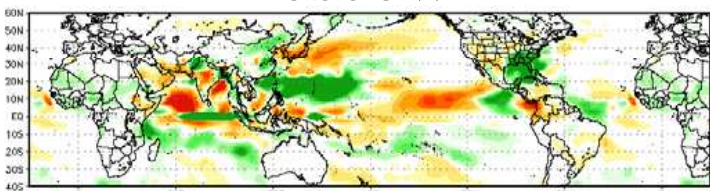
Montreal



Moscow

Pretoria

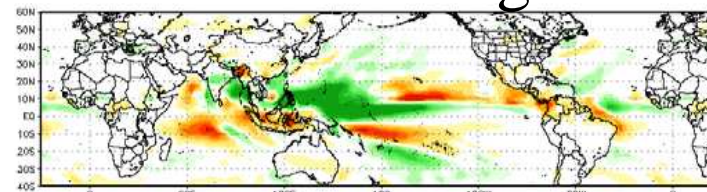
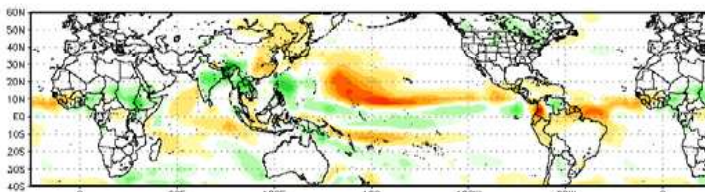
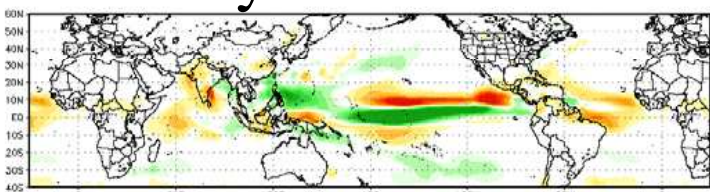
Seoul



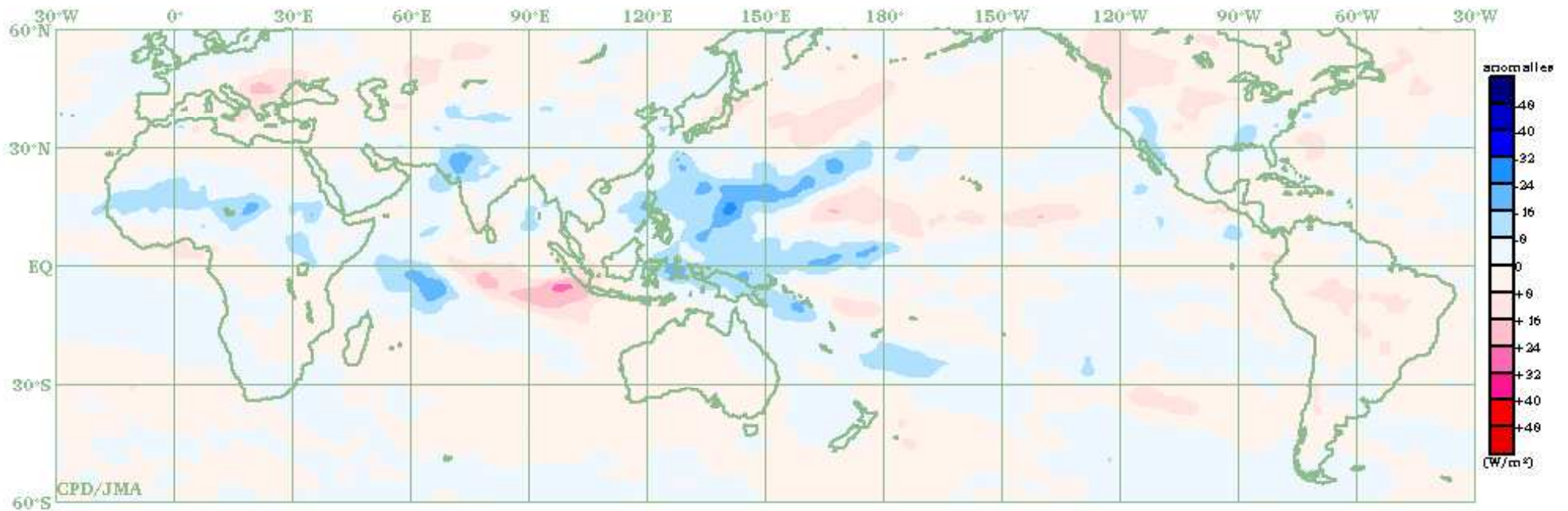
Tokyo

Toulouse

Washington



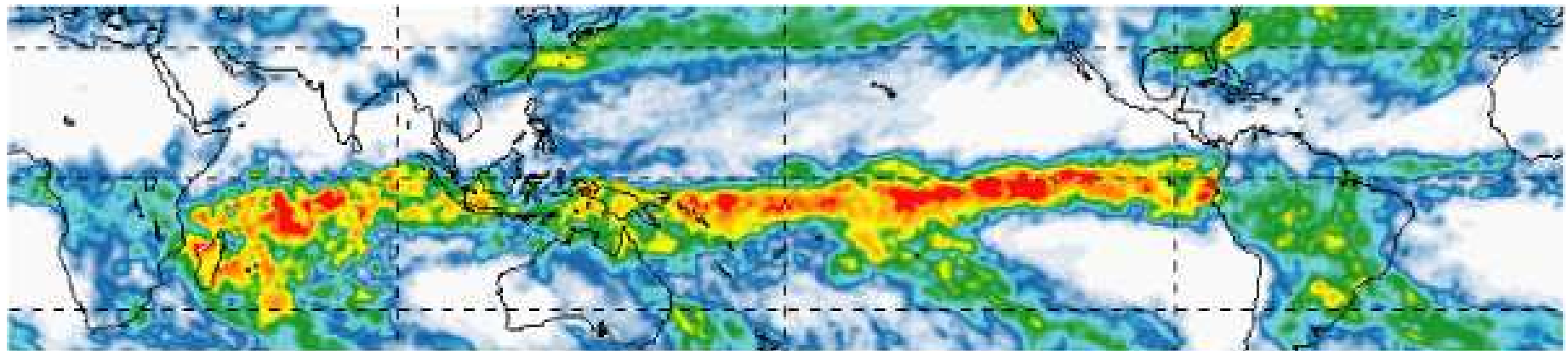
2012 JJA OLR anomaly



THREE-MONTH MEAN OUTGOING LONGWAVE RADIATION (OLR) ANOMALY
The base period for the normal is 1981-2010. Original data provided by NOAA.

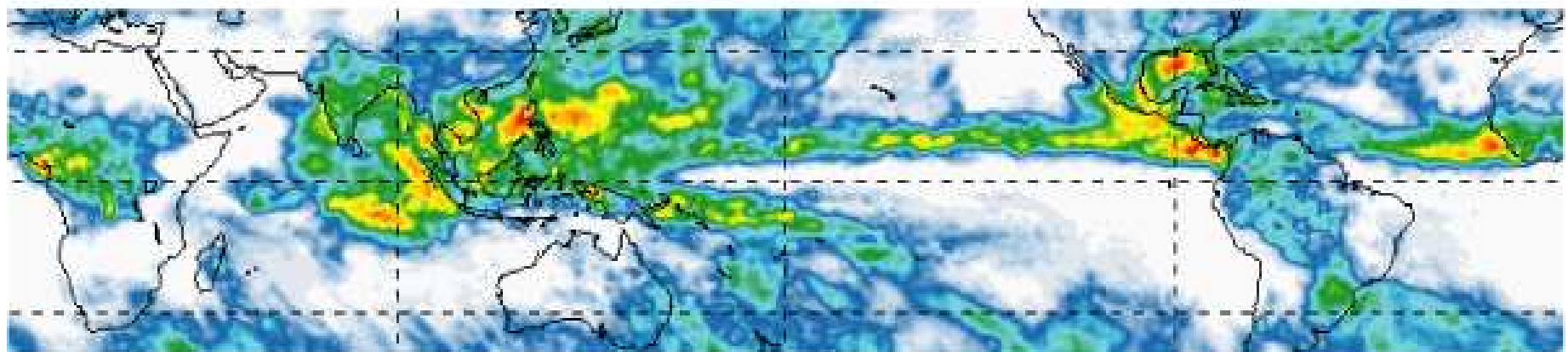
(Jul.-Sep. 2012)

G2: Variability of the Asian-Australian Monsoon System



TRMM + Other Sat Precip Feb 1998

(mm/d)



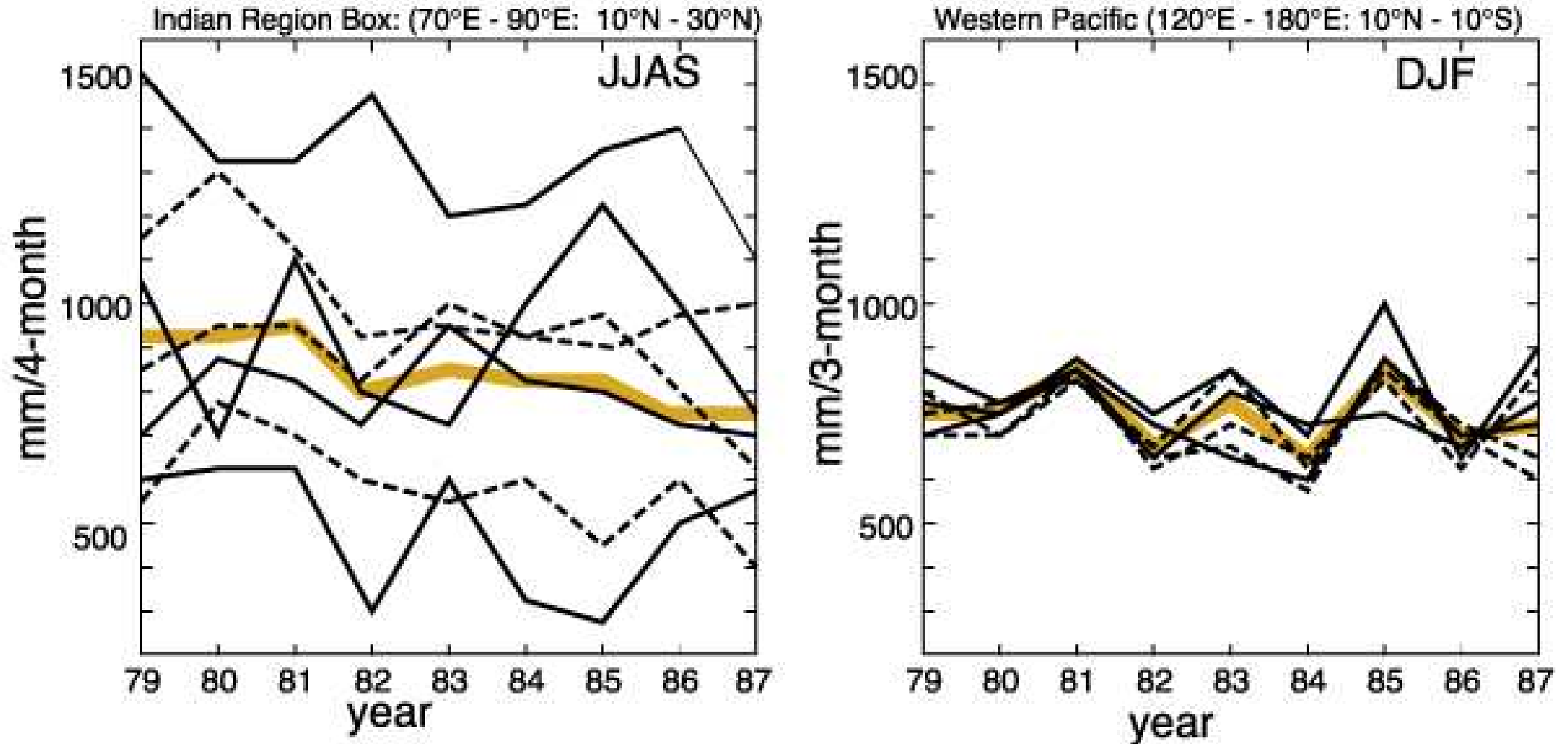
TRMM + Other Sat Precip Sep 1998

(mm/day)



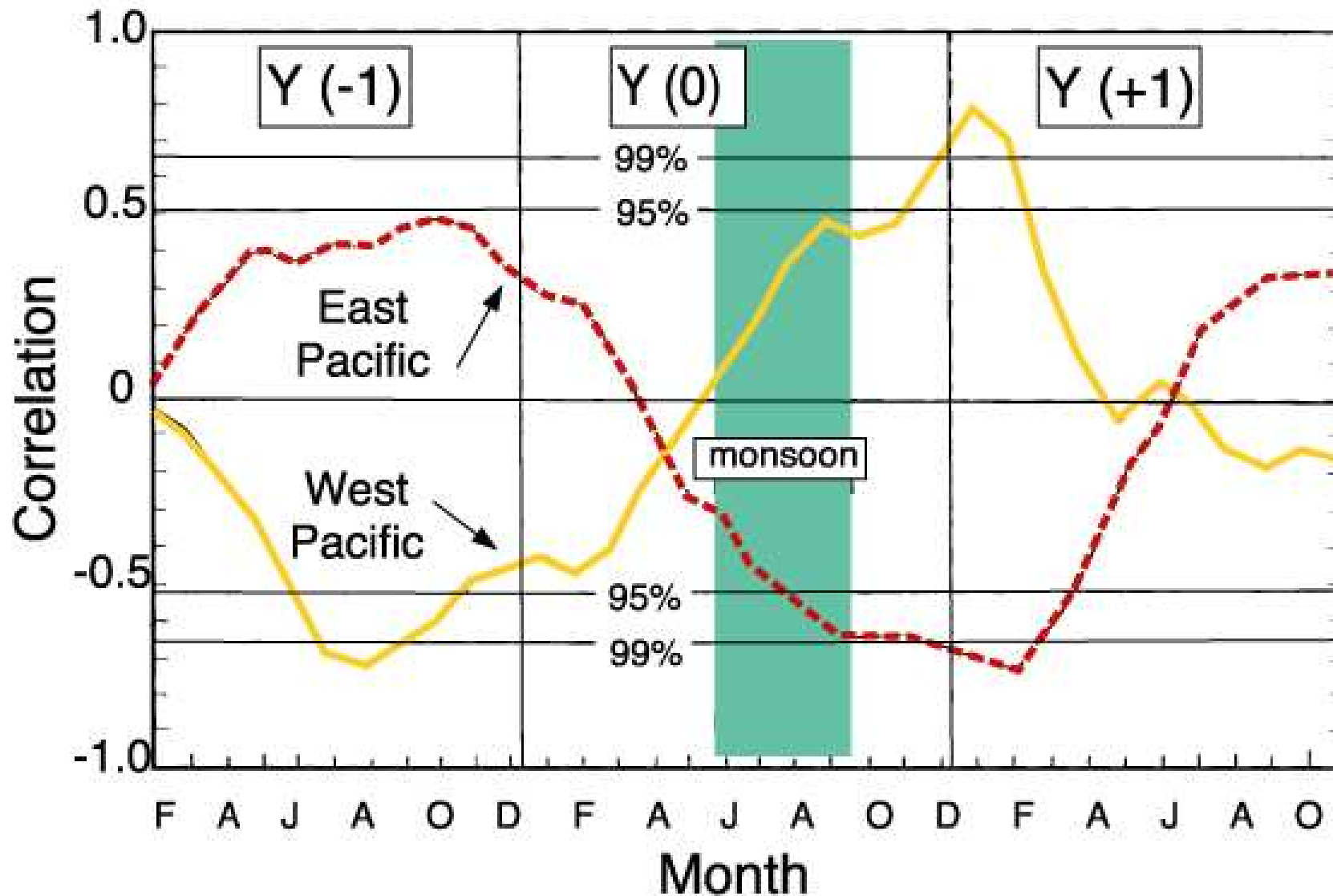
Composite monthly mean precipitation estimates obtained from TRMM data and other satellite precipitation for February and September 1998. In February 1998 the anomalous high precipitation due to the warm ENSO event 1997/98 can clearly be seen over the central and eastern equatorial Pacific. The September image documents the rapid change to cold La Nina conditions with the absence of precipitation extending almost over the entire equatorial Pacific (courtesy of NASA/TRMM).

Modeling the Asian-Australian Monsoon: AMIP models



Comparison of AMIP normalized annual precipitation estimates of 8 models for (left) north India and for (right) the western Pacific Ocean warm pool. Gray curve represents the ensemble mean (Webster 1998).

ENSO-Monsoon relationship



Lagged correlations between the Indian monsoon rainfall anomaly and the SST anomaly in the western Pacific Ocean ($0-8^{\circ}$ N, 130° - 150° E; solid curve) and the eastern Pacific Ocean ($0-8^{\circ}$ N, 170° - 150° W; dashed curve). Y(0) denotes the reference year, and Y(-1) and Y(+1) refer to the year before and after the reference year. From Yasunari (1990, Meteor. Atmos. Phys., 44, 29-41).

Unraveling the Mystery of Indian Monsoon Failure During El Niño

K. Krishna Kumar,¹ Balaji Rajagopalan,^{2,3} Martin Hoerling,^{4*} Gary Bates,⁴ Mark Cane⁵

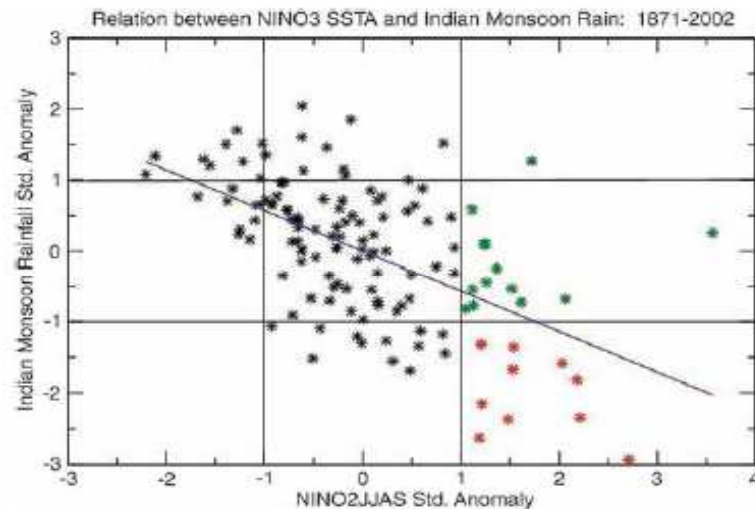


Fig. 1. Plot of standardized, all-India summer [June to September (JJAS)] monsoon rainfall and summer NINO3 anomaly index. Severe drought and drought-free years during El Niño events (standardized NINO3 anomalies > 1) are shown in red and green, respectively.

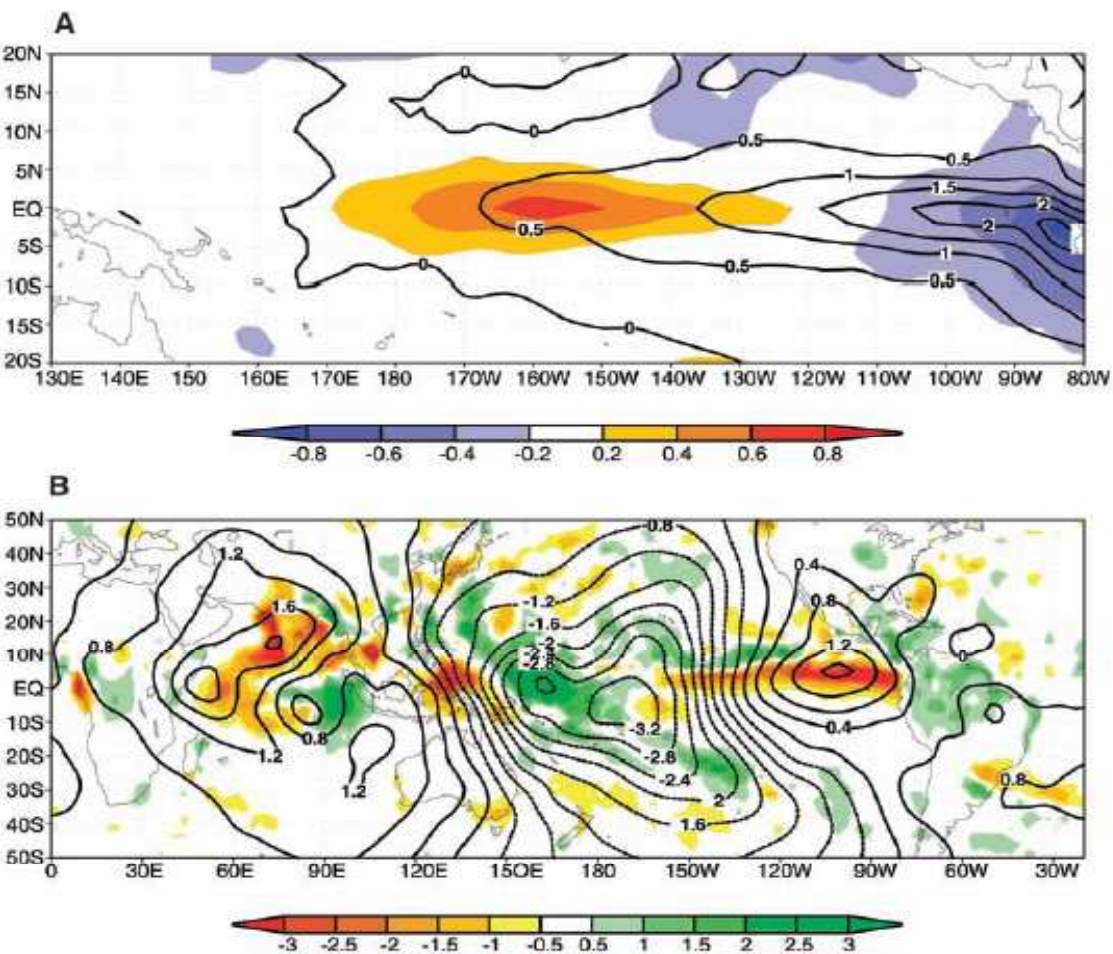
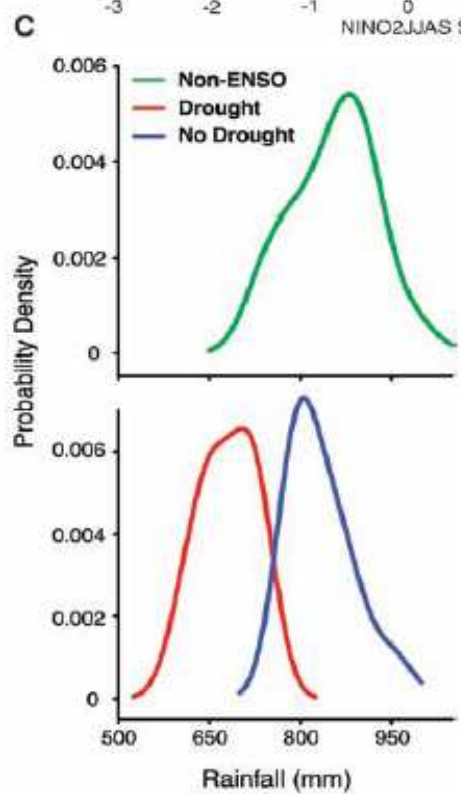


Fig. 2. (A) Composite SST difference pattern between severe drought (shaded) and drought-free El Niño years. Composite SST anomaly patterns of drought-free years are shown as contours. (B) Composite difference pattern between severe drought and drought-free years of velocity potential (contours) and rainfall (shaded). (C) PDF of all-India summer monsoon

rainfall from severe-drought (red curve) and drought-free (blue curve) years associated with El Niño occurrence and from the non-ENSO years (green curve). SST and velocity potential composite differences are based on 1950 to 2004, rainfall composites are based on 1979 to 2004, and PDFs are based on 1873 to 2004.

Unraveling the Mystery of Indian Monsoon Failure During El Niño

Science, 2006

K. Krishna Kumar,¹ Balaji Rajagopalan,^{2,3} Martin Hoerling,^{4*} Gary Bates,⁴ Mark Cane⁵

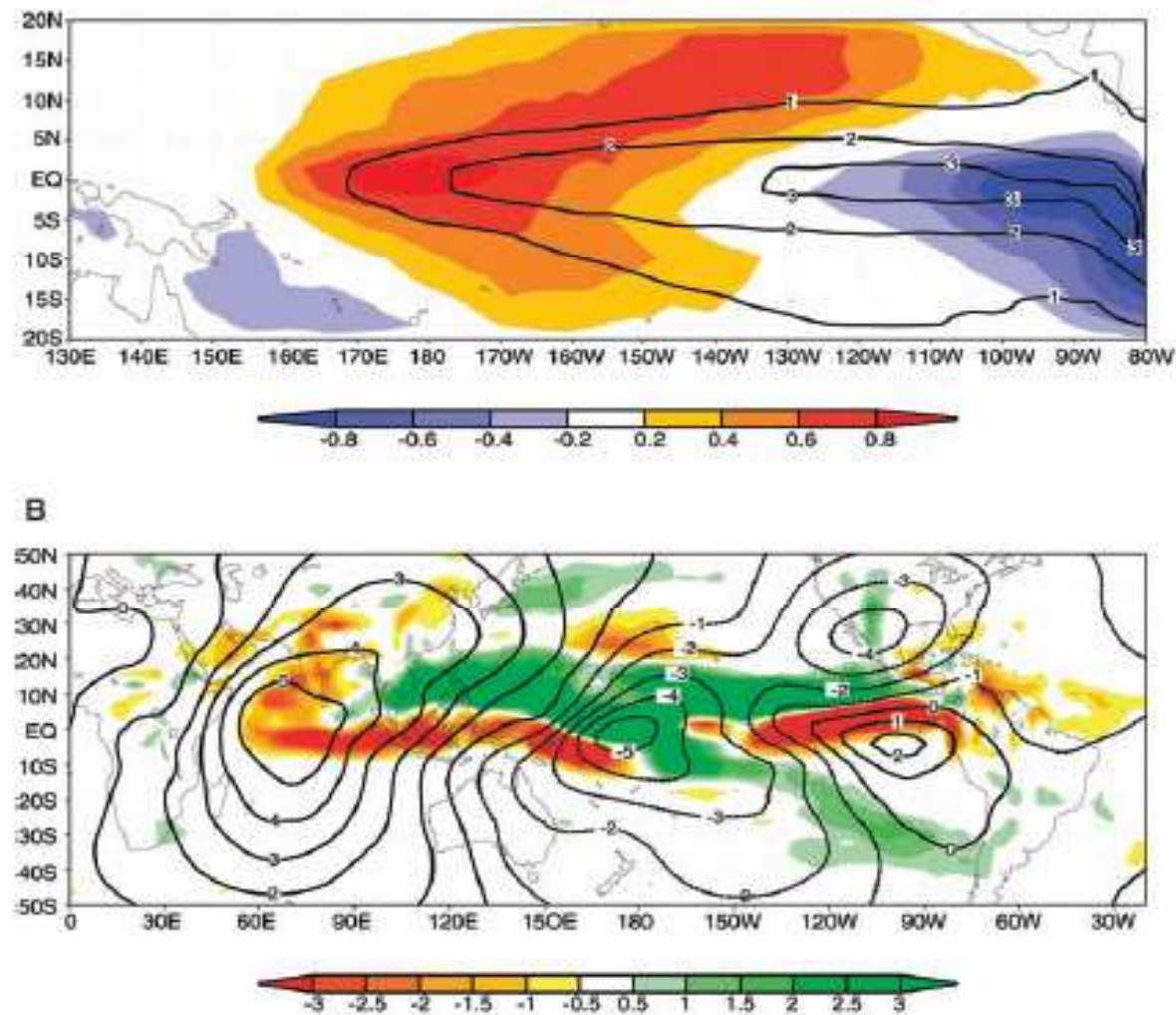
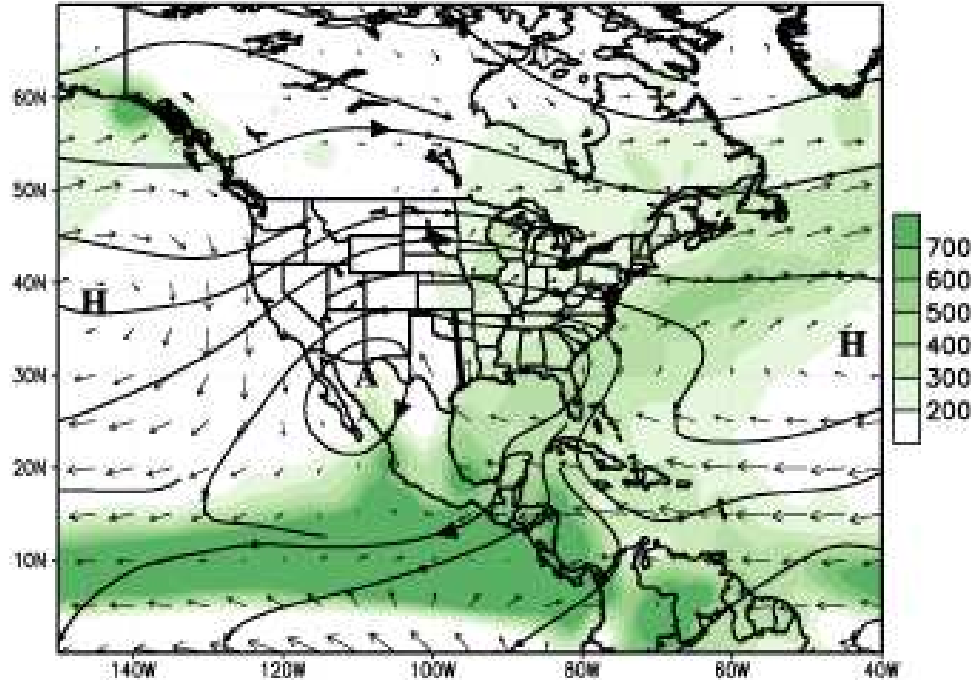


Fig. 4. (A) Contours are of the +2 SD experiment (iii) and are analogous to the amplitude and structure of the composite El Niño SSTs for drought-free years in Fig. 2A. Shadings are of the difference between the +2 SD SST forcings of experiments (ii) and (iii) and are analogous to the observed SST structure that discriminates severe drought from drought-free El Niño years. (B) The ensemble mean rainfall (shading) and 200 hPa velocity potential (contour) differences between experiments (ii) and (iii). (C) The PDF of the

Indian monsoon rainfall corresponding to (top) the control, or unforced, experiment (i) green curve; and (middle and bottom) the forced experiments (ii) red curve, (iii) blue curve, and (iv) dashed line with +1 SD (middle) and +2 SD (bottom) imposed SST anomalies. For forced experiment (iv), only the median value (dashed line) is shown. For the forced experiments, each PDF is estimated from 30 ensembles. The model rainfall has been averaged over the Indian monsoon region of 8° to 30°N, 70° to 90°E.

G3: Variability of the American Monsoon Systems

a)



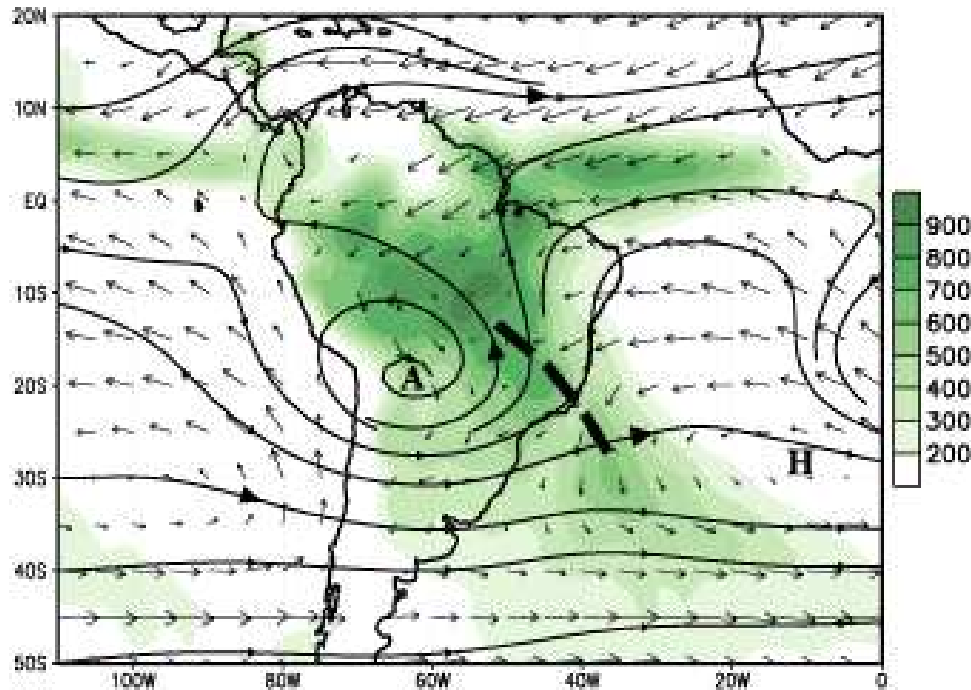
July-September

A: American North Monsoon High

H: Bermuda and North Pacific subtropical high

Solid line: Great Plains low-level jet

b)

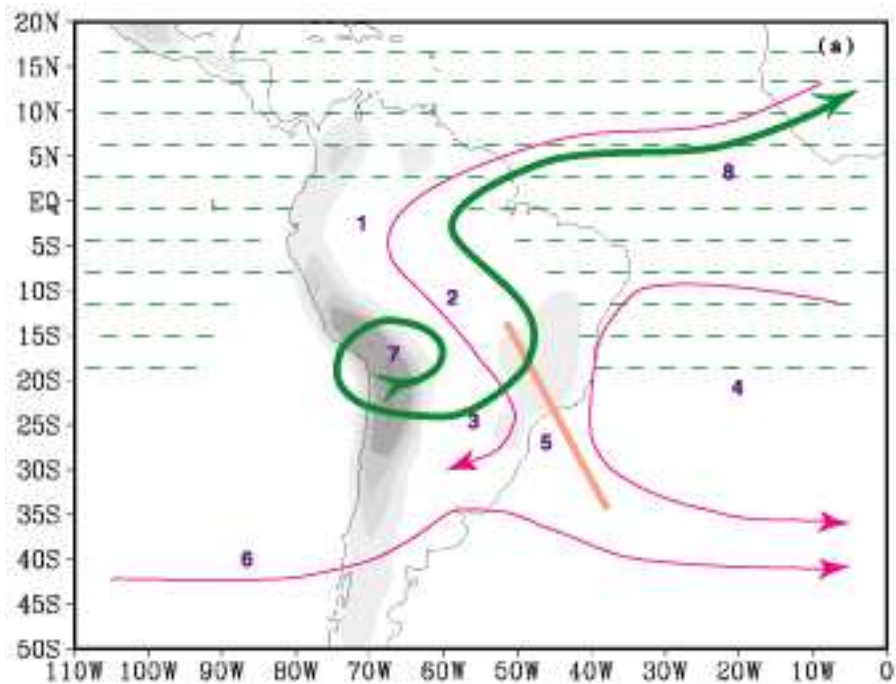


December-February

A: Bolivian High

H: South Atlantic subtropical high

Dashed line: South Atlantic Convergence Zone



Elementary features for (a) the South American Summer Monsoon and (b) the East Asian Summer Monsoon.

Dashed lines: easterlies

1: low-level cross equatorial flow

2: northwesterlies vs. southwesterlies

3: Gran Chaco low vs. EASM trough

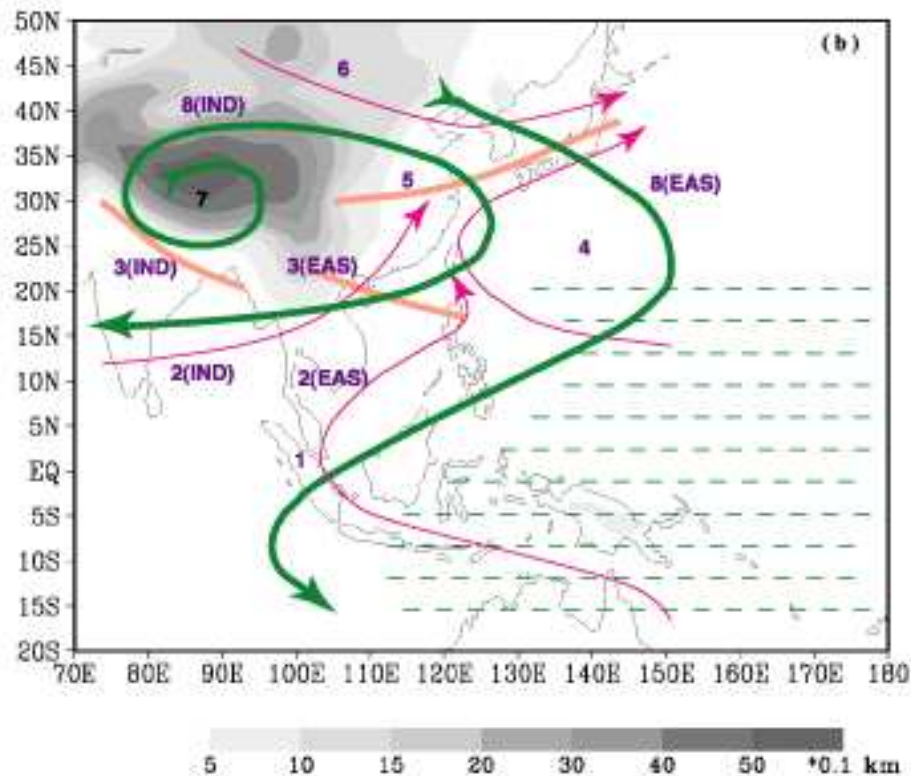
4: subtropical high

5: SACZ vs. Mei-Yu/Baiu front zone

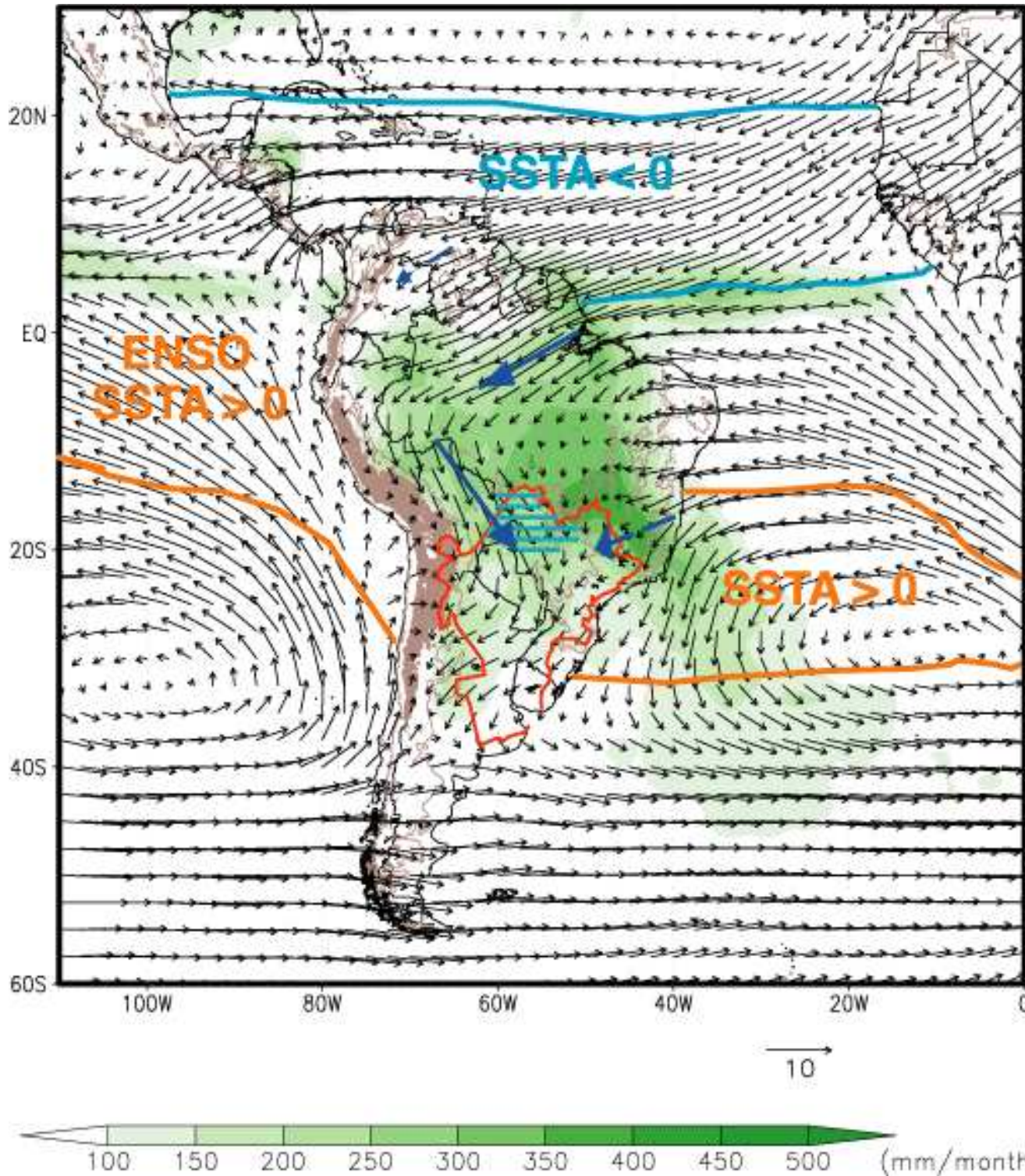
6: midlatitude westerlies

7: Bolivian high vs. Tibetan high

8: upper level return flow

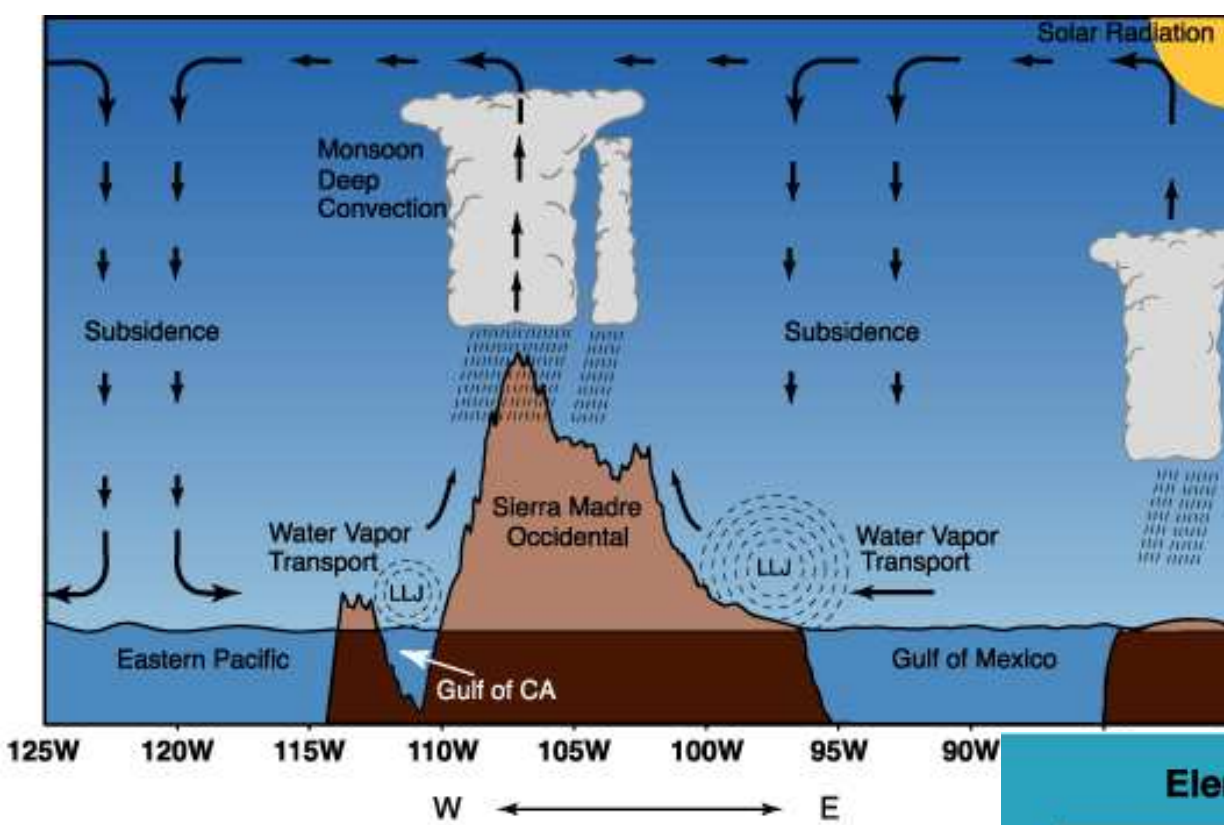


South American Monsoon Modulation by SST Anomalies

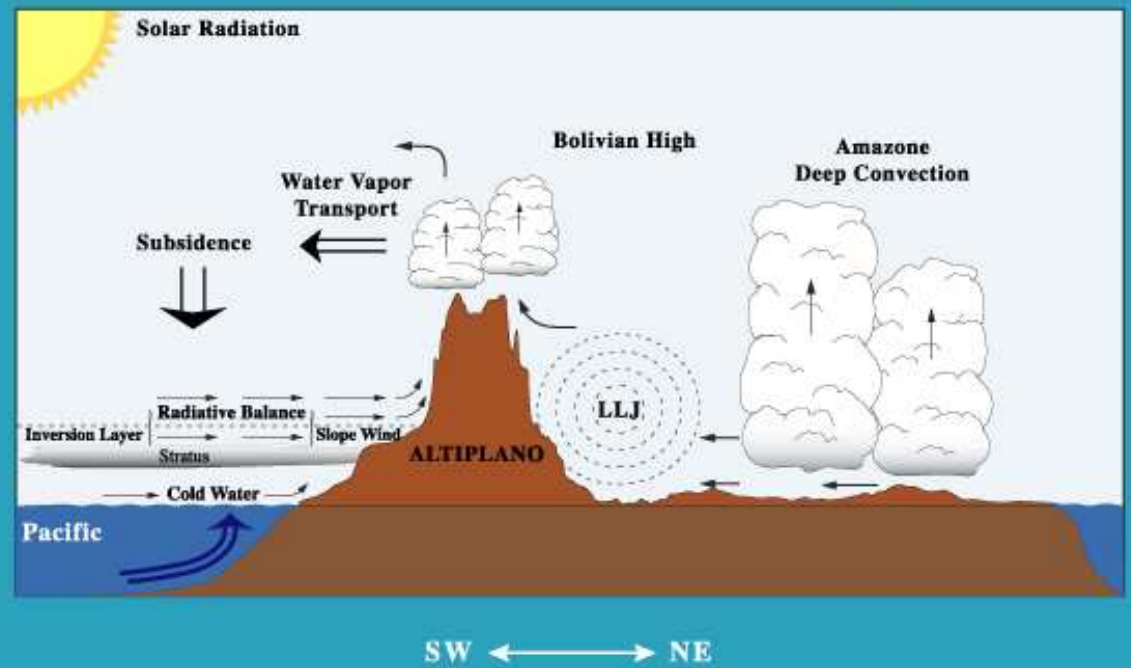


Links between climate variability in the Rio de la Plata basin (area encircled by the red curve) and SST anomalies for the southern warm season (December-February). Green shading corresponds to precipitation (mm/month), black arrows to 925 hPa winds, thick blue arrows to maxima in vertically integrated moisture transport, and the blue hatched region to the Pantanal. The configuration of SST anomalies corresponds to enhanced precipitation in the basin.

North American (Mexican) and South American Monsoon System

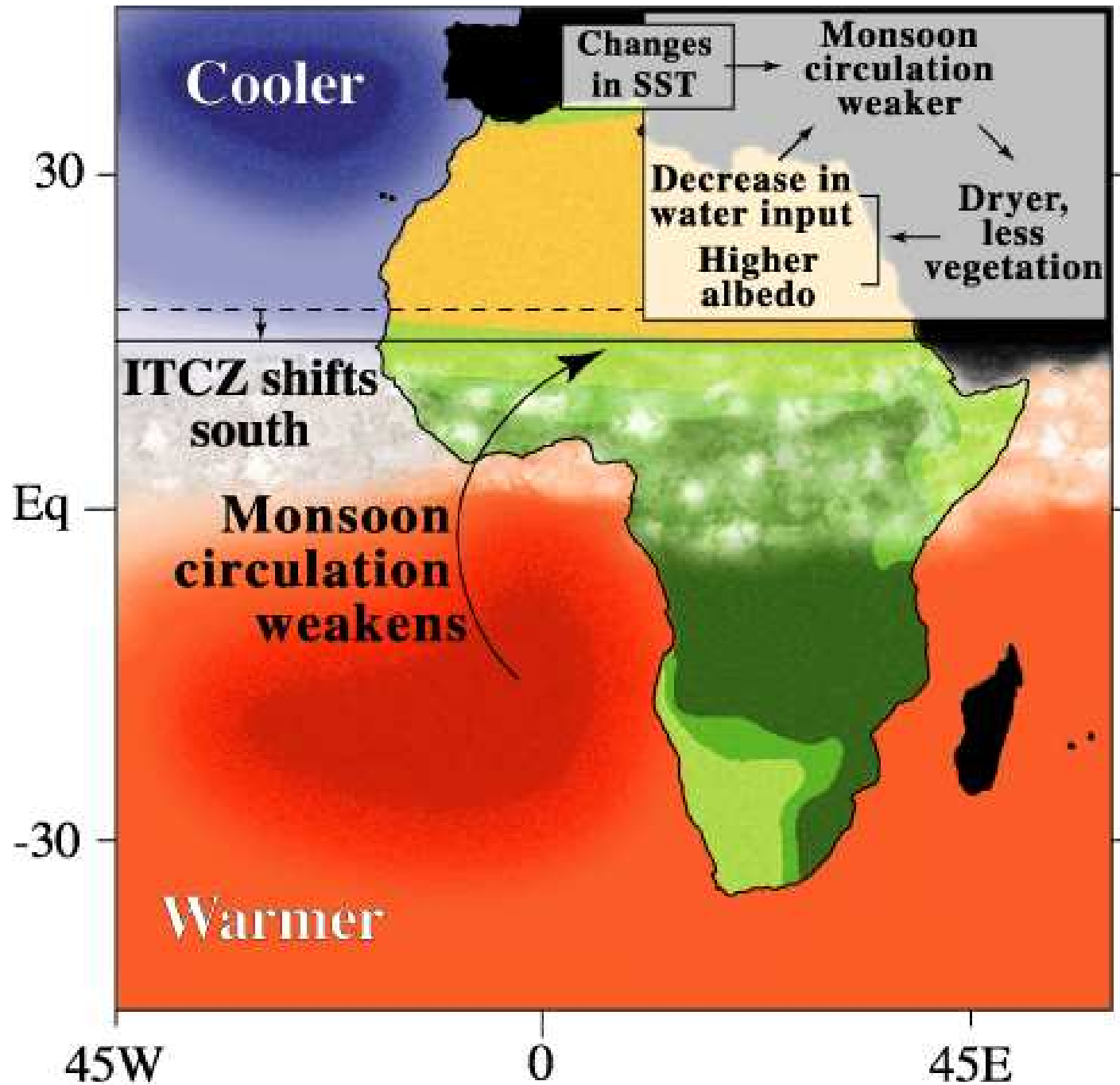


Elements of the South American Monsoon System



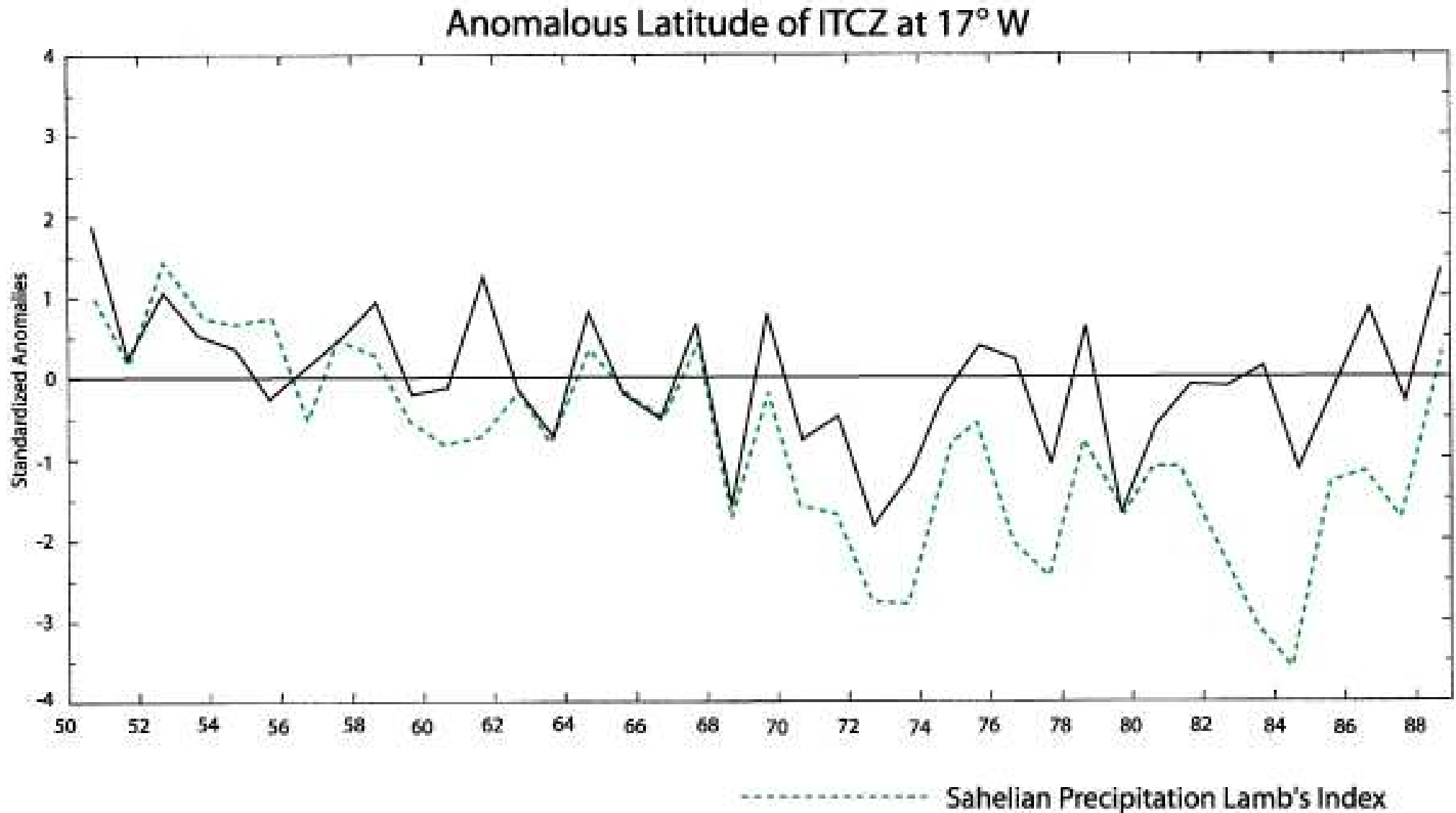
Section across South America displaying schematically the major large-scale elements affecting the South American Monsoon System

G4: African Climate Variability



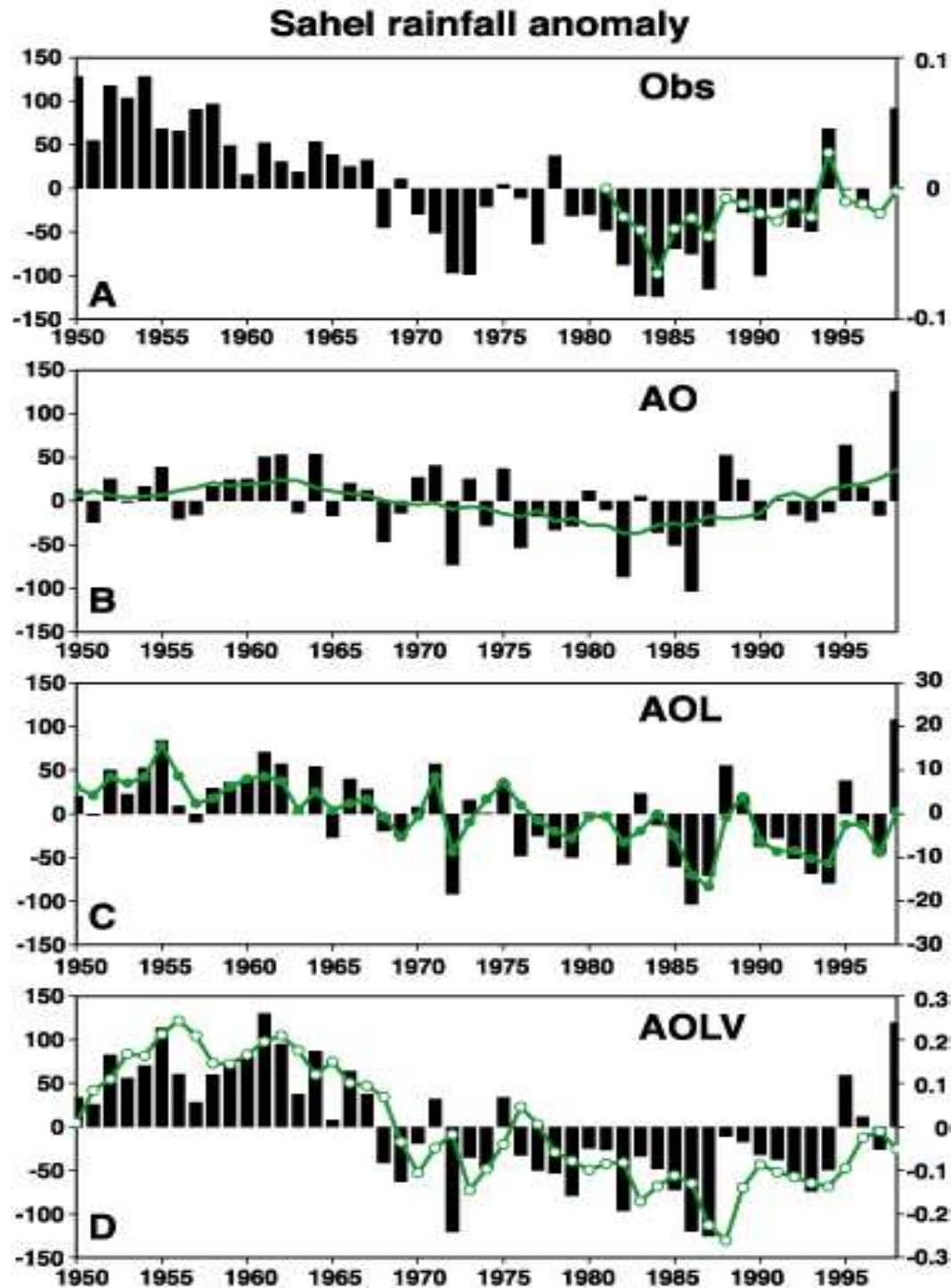
SST – Rainfall –
Vegetation feedback
over the Sahel region

Variability of the Sahelian Rainfall



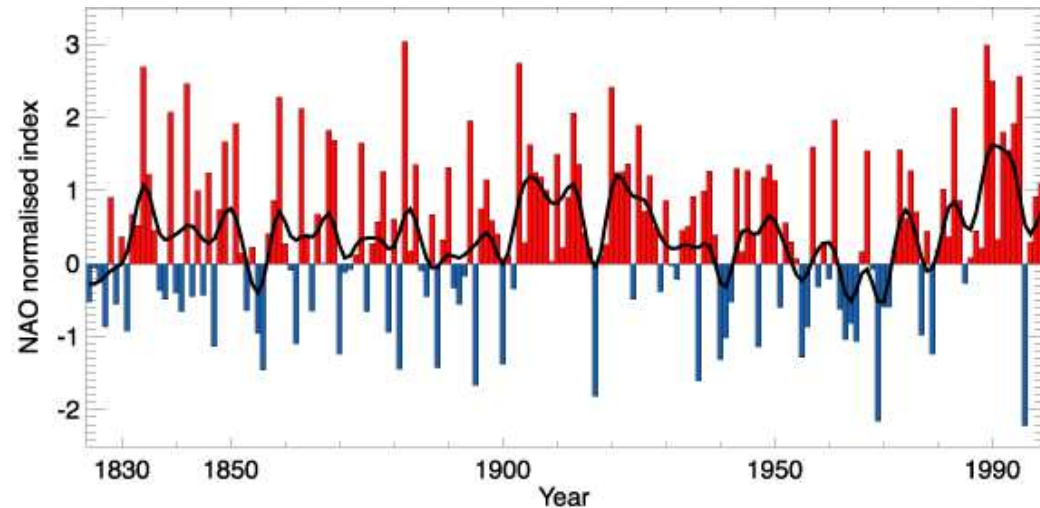
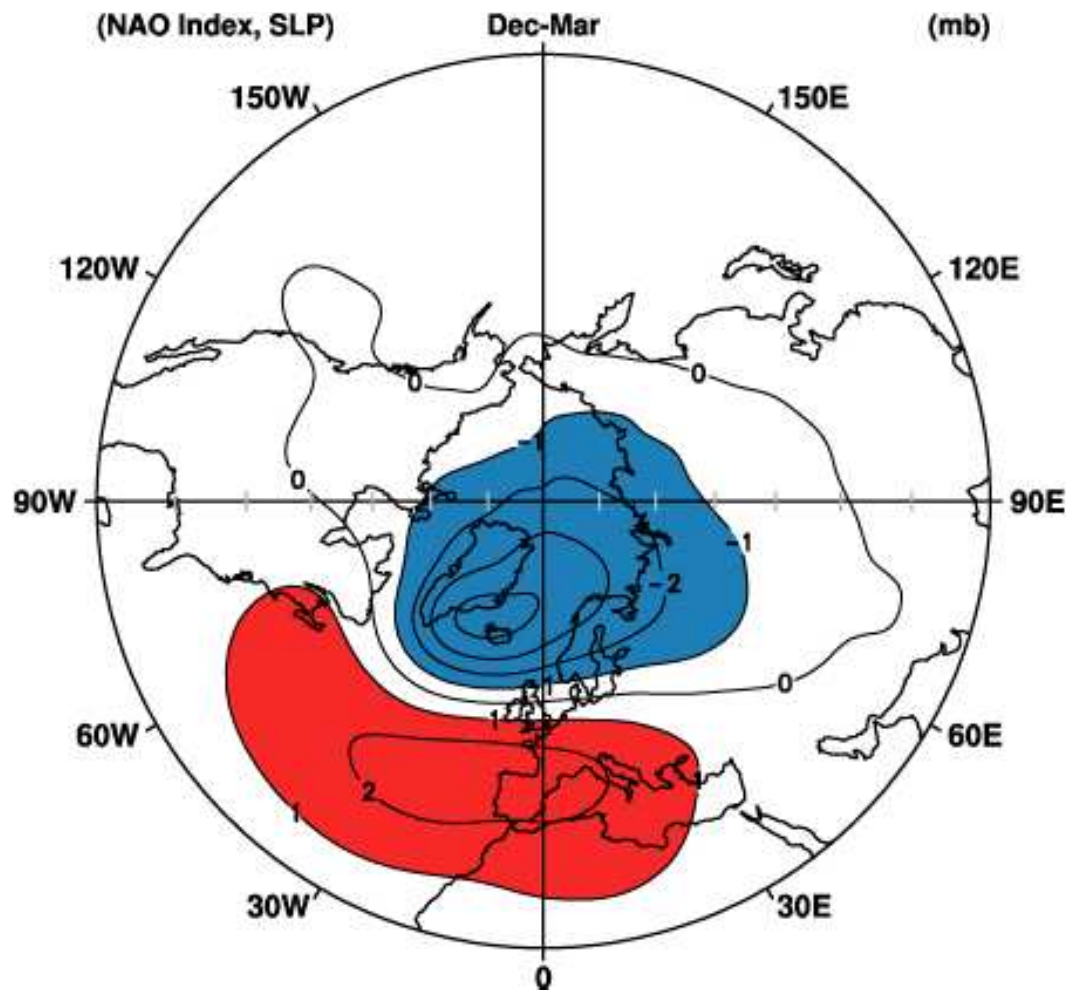
Sahelian rainfall variability is closely linked to the latitudinal position of the Intertropical Convergence Zone (ITCZ) and the meridional SST gradient in the tropical Atlantic. The latitude of the ITCZ depends upon both local conditions and remote forcings. The North Atlantic Oscillation (NAO) also generates a component of climate variability over the northern rim of the continent and over Western Africa (Tourre and Lamb 1997).

GCM Simulation of the Sahelian Rainfall



The dramatic drying trend in the Sahel from the 1950s to the 1980s is initially forced by SST (b) but amplified by soil moisture (c) and vegetation (d).

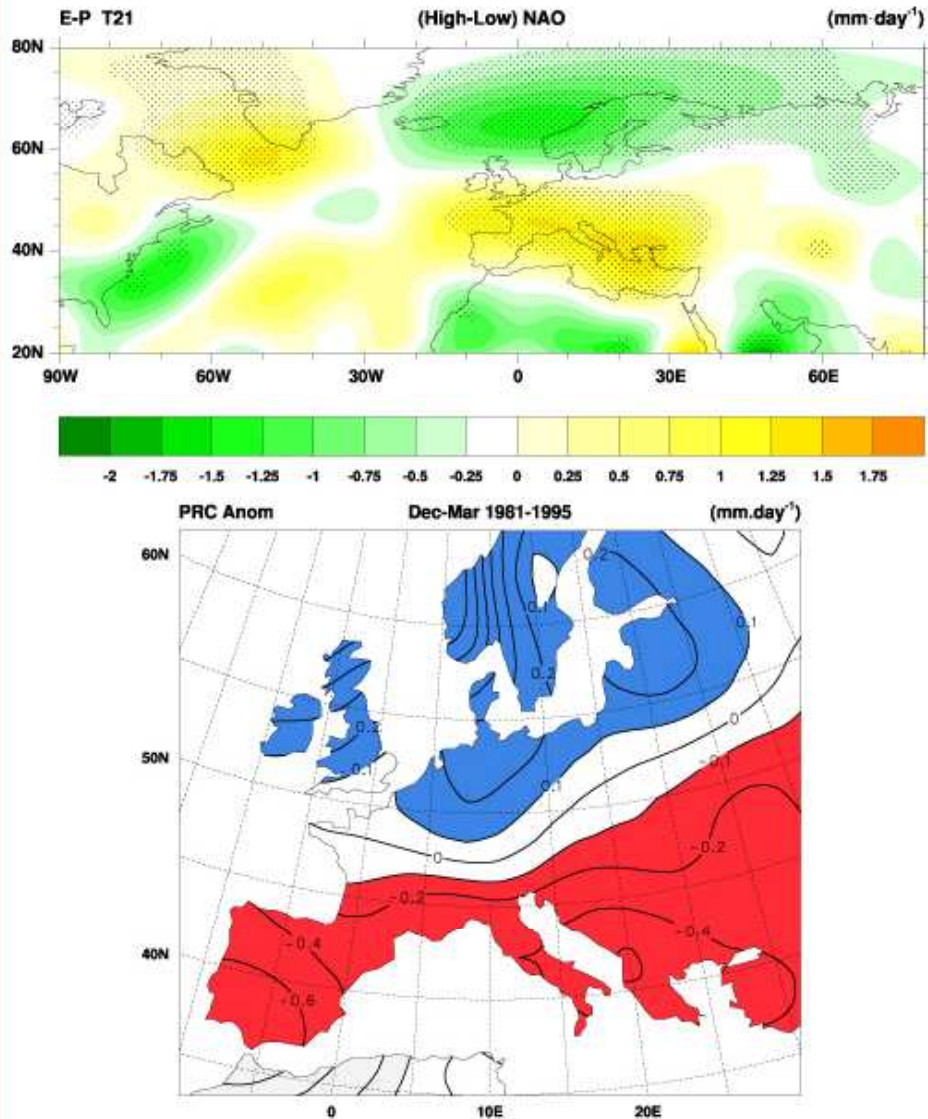
D1: The North Atlantic Oscillation



NAO index based on the difference of normalized SLP between Portugal and Iceland from 1864 to 1995.

Observed Dec-Mar change in SLP associated with a 1 standard deviation in the NAO index (after Hurrell 1995).

Impacts of the NAO

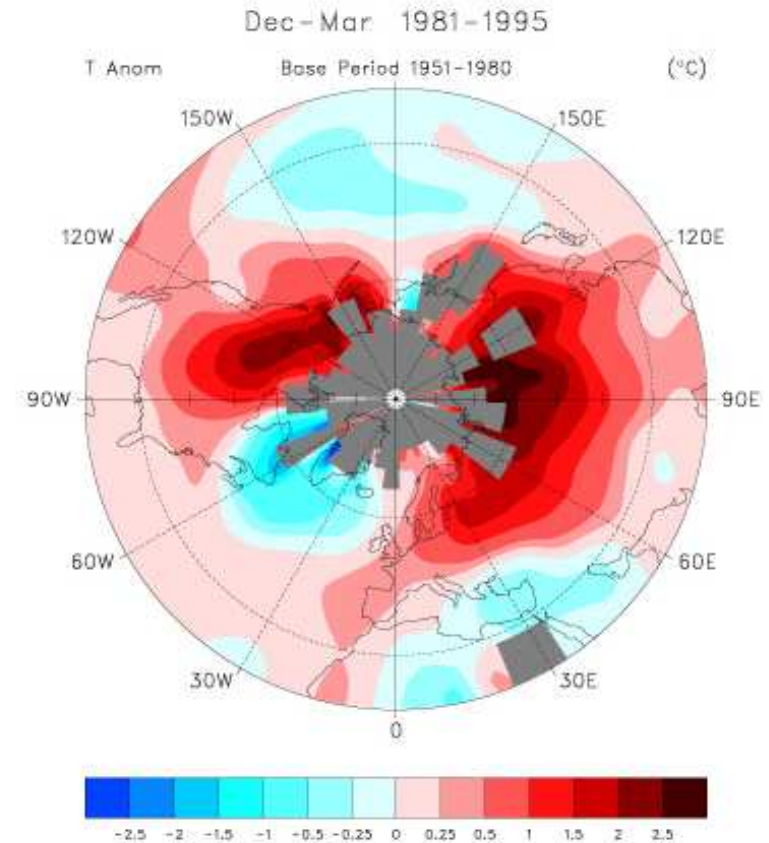


Upper panel: Above: Precipitation anomalies associated with the NAO; E-P is plotted, computed as a residual of the atmospheric moisture budget using ECMWF global analyses, for high NAO index minus low index winters (see Hurrell, 1995, Science, 269, 676-679).

Lower panel: Right: 1981-94 average precipitation anomalies expressed as departures from 1951-80 mean, from station data in Eischeid et al. (1991) data set (courtesy of J. Hurrell)

LB/D1/99-4

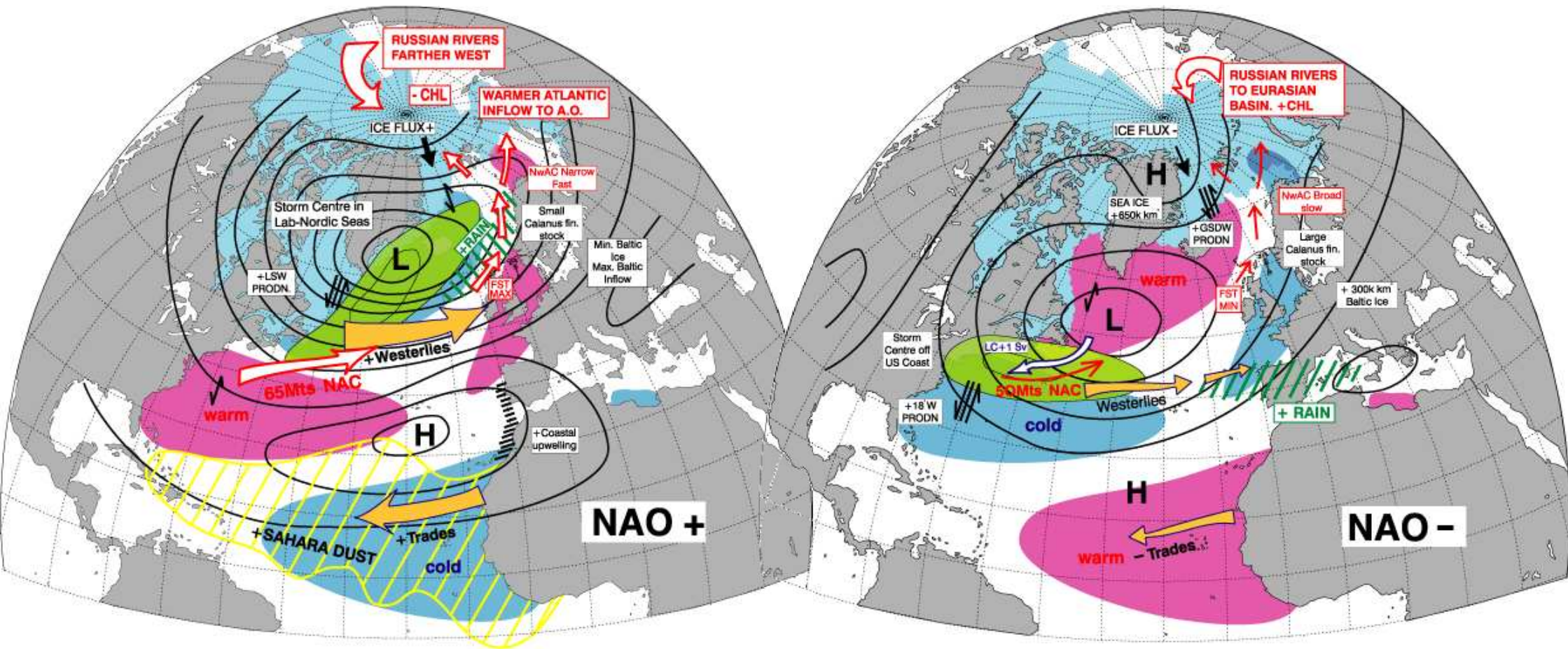
Impacts of the NAO



Observed Dec-March surface temperature anomalies associated with a high NAO index; the period 1981-1995, when the NAO was high, relative to the period 1951-1980, when the NAO was low (after Hurrell, 1996). The temperature data consists of land surface temperature blended with SST data (Jones and Briffa, 1992, The Holocene, 2, 174-188).

LB/D1/99-5

The two phases of the NAO

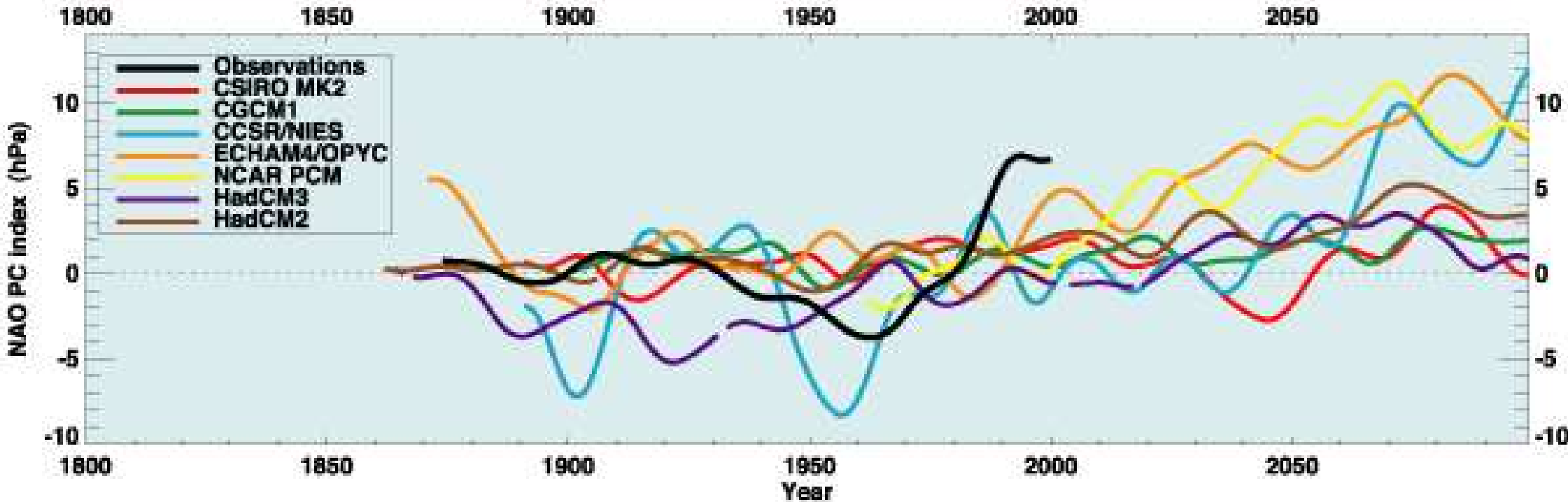


High phase: westerlies in the North Atlantic are enhanced, resulting in mild and wet winter conditions over Northern Europe

Low phase: westerlies in the North Atlantic are weakened, resulting in cold and dry winter conditions over Northern Europe

Changes in the NAO due to Climate Change?

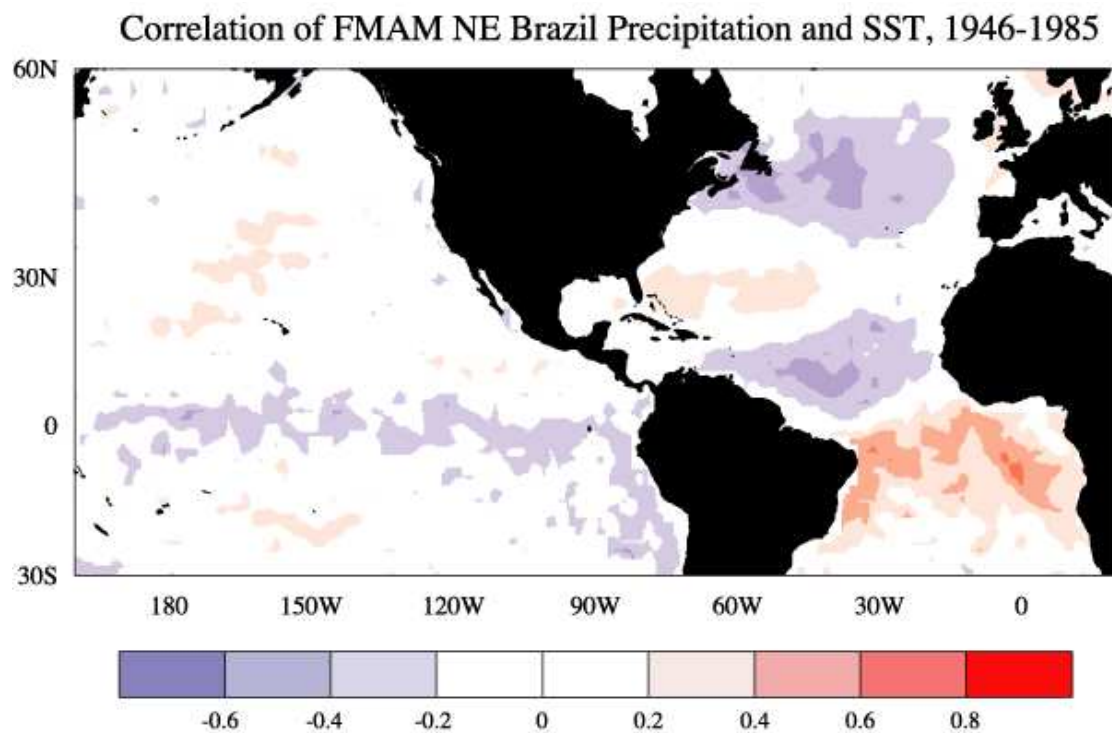
Observed and simulated (winter) North Atlantic Oscillation



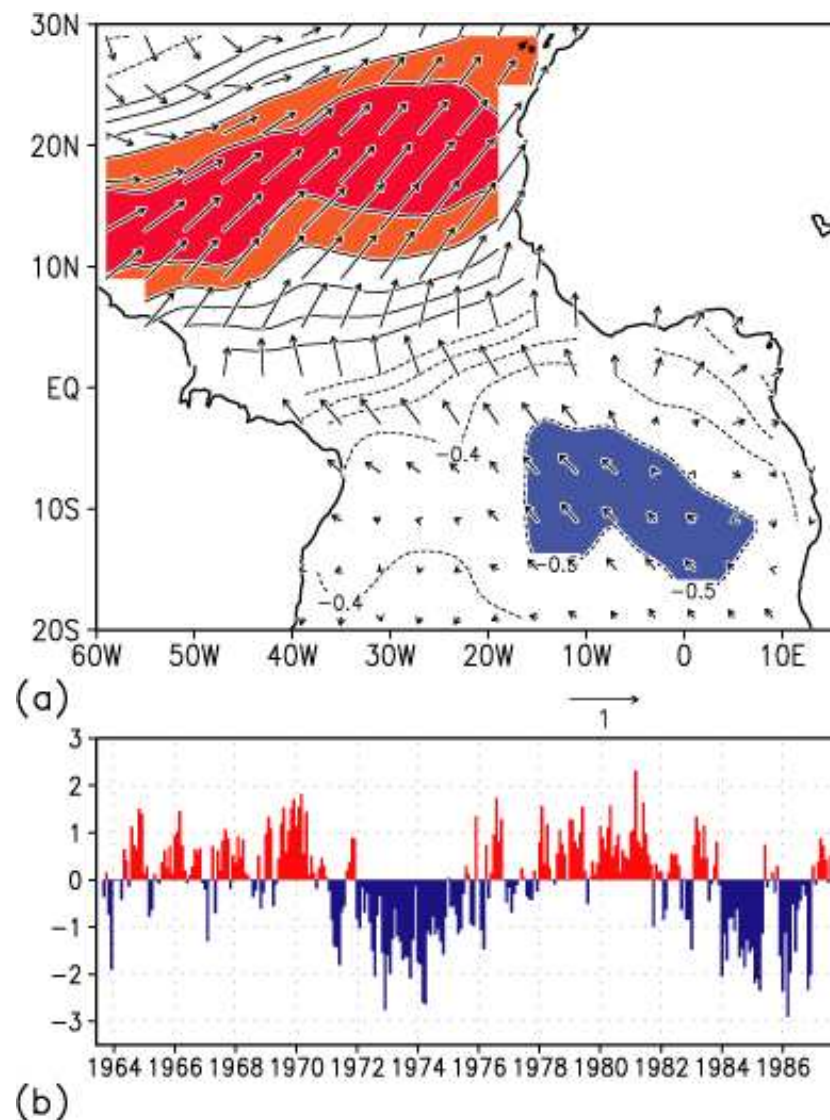
Winter NAO indices from observations (black) and from seven model simulations forced with increased CO₂ concentrations showing a shift towards positive NAO index.

D2: Tropical Atlantic Variability

CLIVAR AV/D2/99-7,99-8

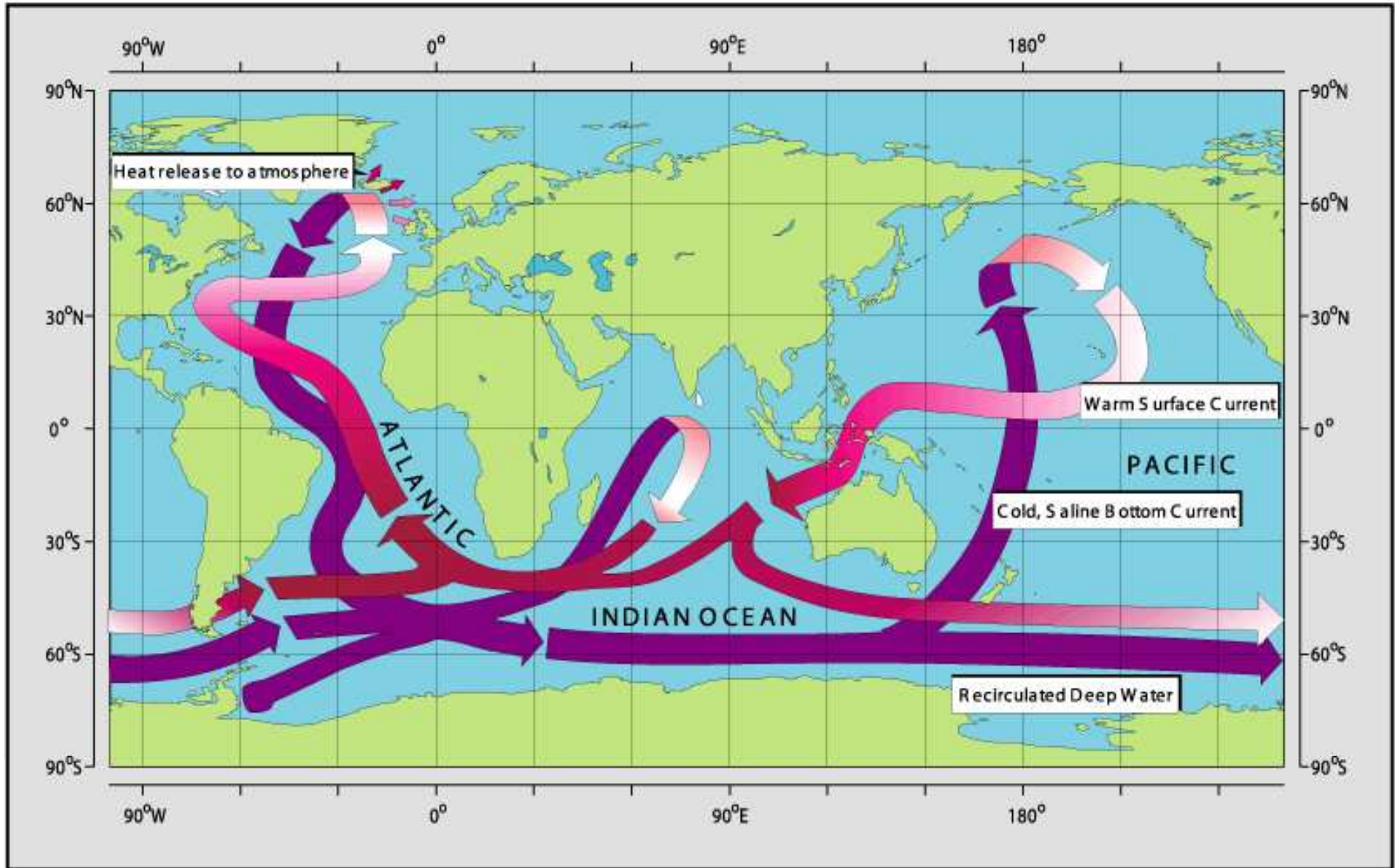


Northeast Brazil rainfall tends to be more strongly correlated with Atlantic SST than with Pacific SST.



Dominant joint patterns of SST and surface wind stress variability over the Atlantic for 1963-1987.

D3: The Atlantic Thermohaline Circulation



Schematic diagram of the global ocean circulation pathways, the 'conveyor' belt (after W. Broecker, modified by E. Maier-Reimer).

DATA

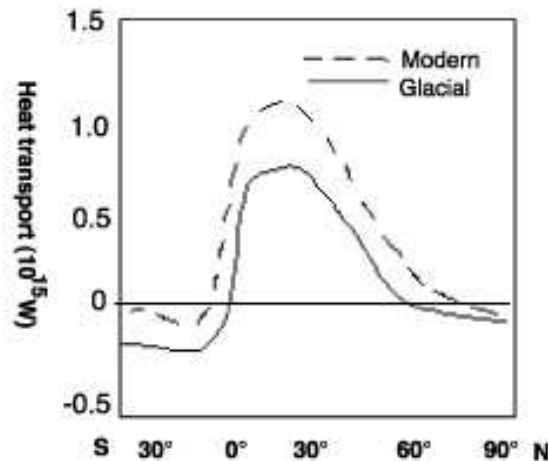
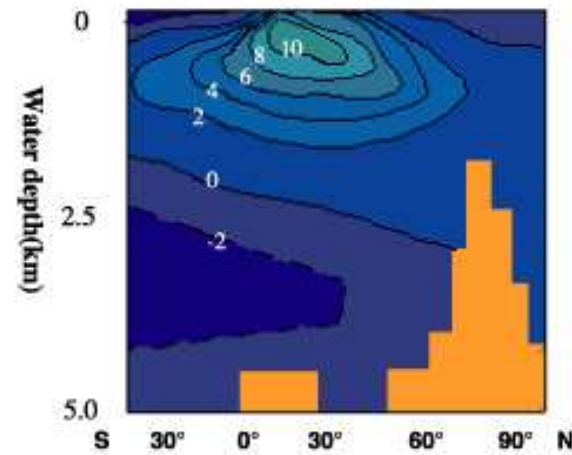
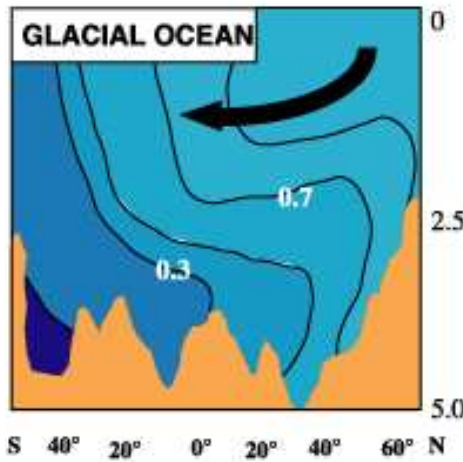
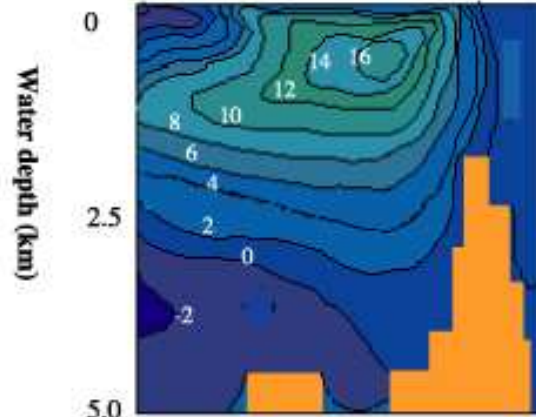
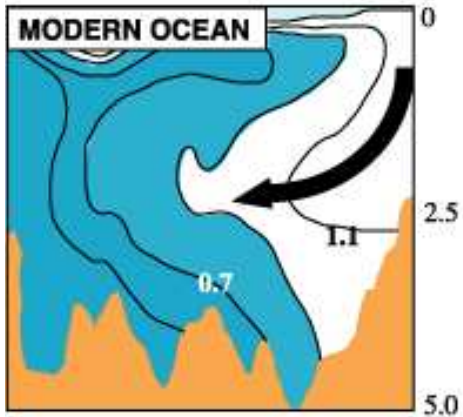
2D - OCEAN MODEL

Sudden Changes in the Thermohaline Circulation

Left: reconstruction of the ^{13}C changes across the Atlantic ocean for the modern period (upper panel) and the Last Glacial Maximum (LGM, lower panel); adapted from Duplessy et al., 1988.

Right: contour of the mean annual meridional overturning stream-function in the Atlantic basin for the modern conditions (upper panel) and the LGM (middle panel) calculated by the ocean model (Fichefel et al., 1994).

The lower panel shows the mean annual meridional heat transport computed for the present and the LGM boundary conditions.



Atlantic Thermohaline Circulation Changes

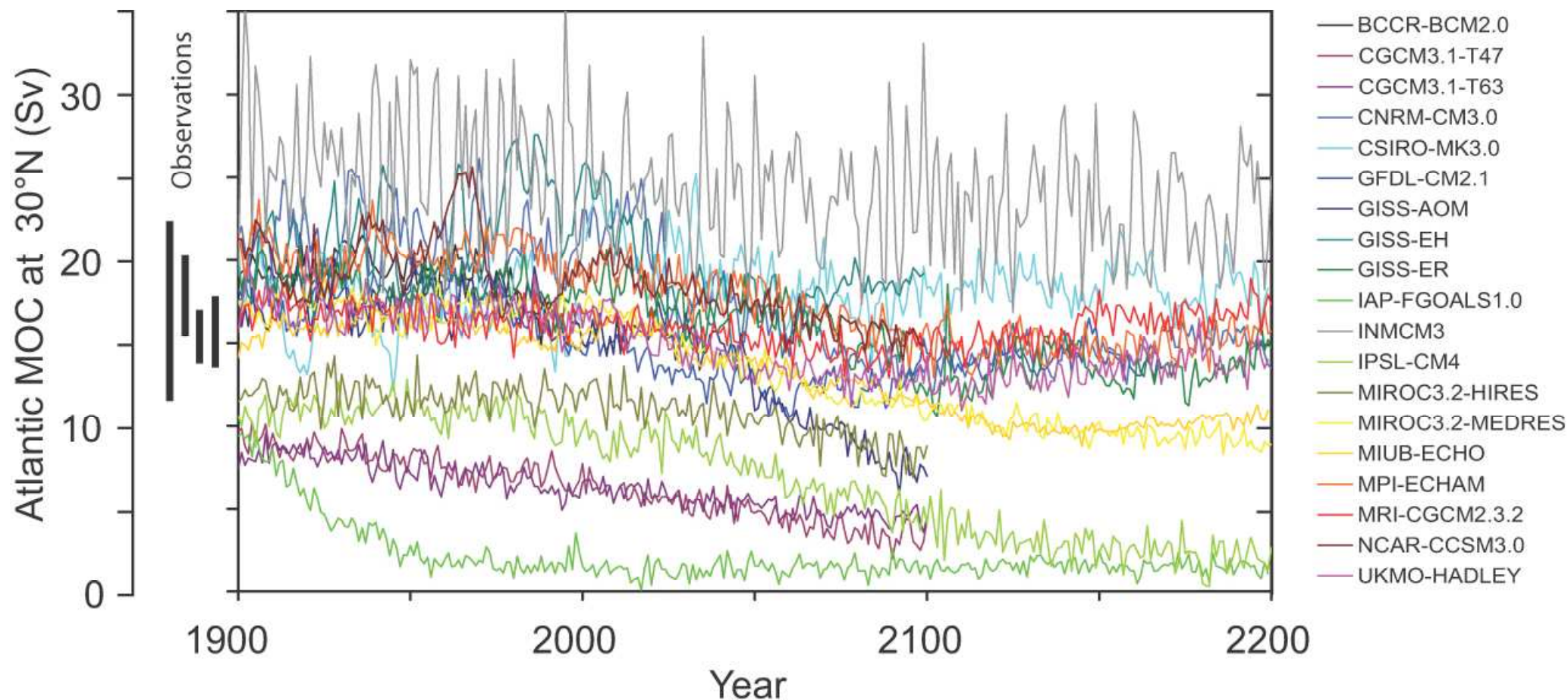
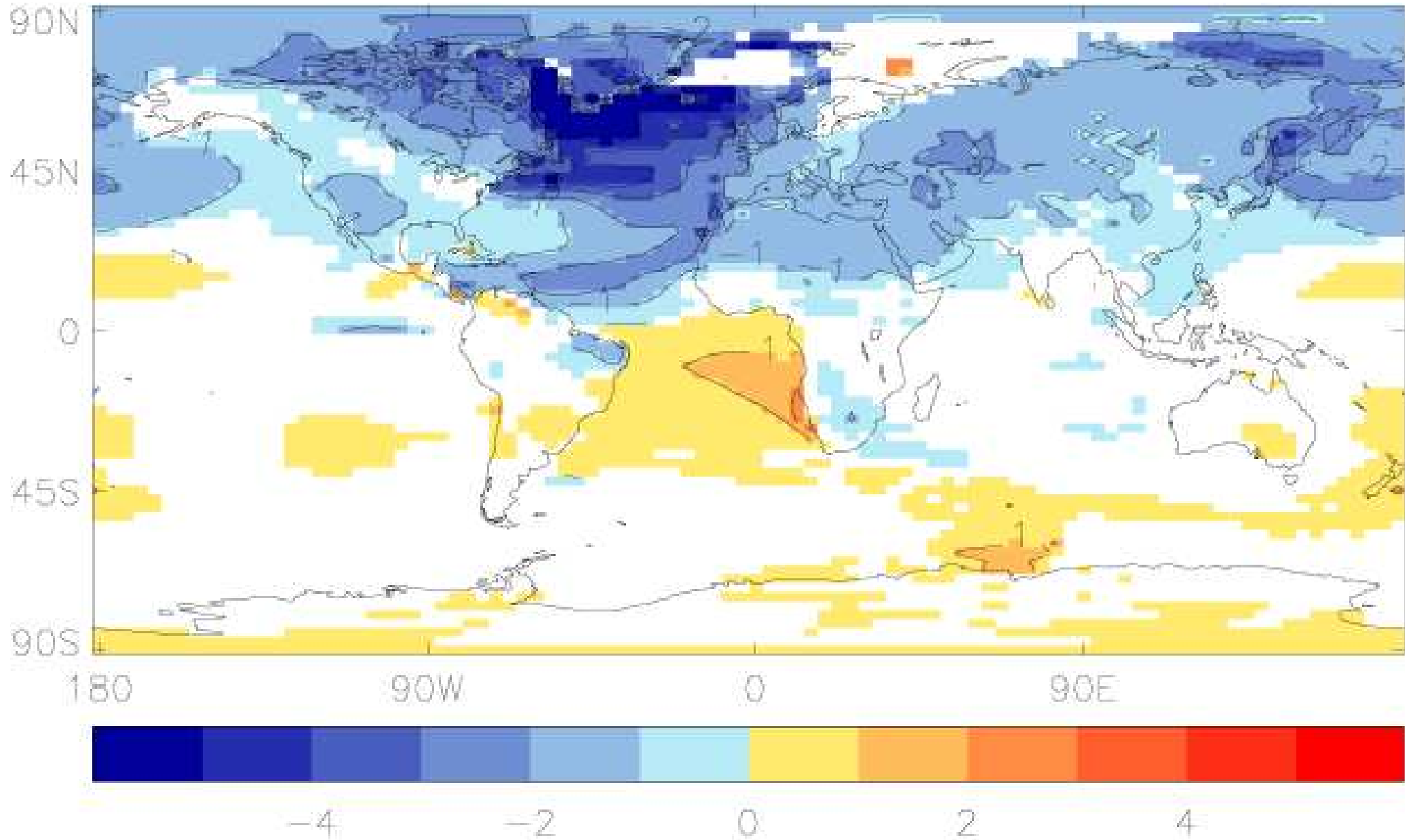


Figure 10.15. Evolution of the Atlantic meridional overturning circulation (MOC) at 30° N in simulations with the suite of comprehensive coupled climate models (see Table 8.1 for model details) from 1850 to 2100 using 20th Century Climate in Coupled Models (20C3M) simulations for 1850 to 1999 and the SRES A1B emissions scenario for 1999 to 2100. Some of the models continue the integration to year 2200 with the forcing held constant at the values of year 2100. Observationally based estimates of late-20th century MOC are shown as vertical bars on the left. Three simulations show a steady or rapid slow down of the MOC that is unrelated to the forcing; a few others have late-20th century simulated values that are inconsistent with observational estimates. Of the model simulations consistent with the late-20th century observational estimates, no simulation shows an increase in the MOC during the 21st century; reductions range from indistinguishable within the simulated natural variability to over 50% relative to the 1960 to 1990 mean; and none of the models projects an abrupt transition to an off state of the MOC. Adapted from Schmittner et al. (2005) with additions.

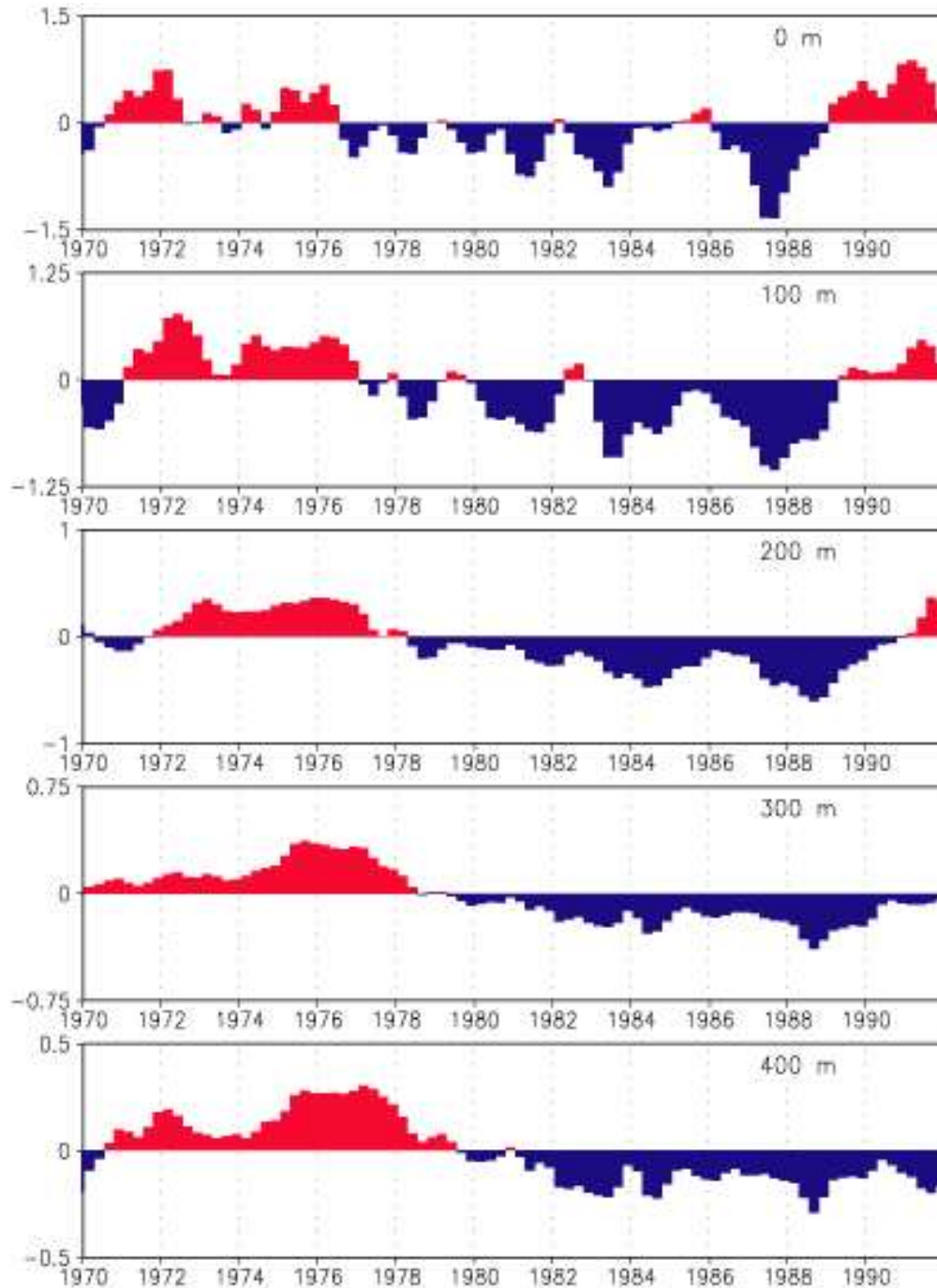
SAT Change after a collapse of the THC



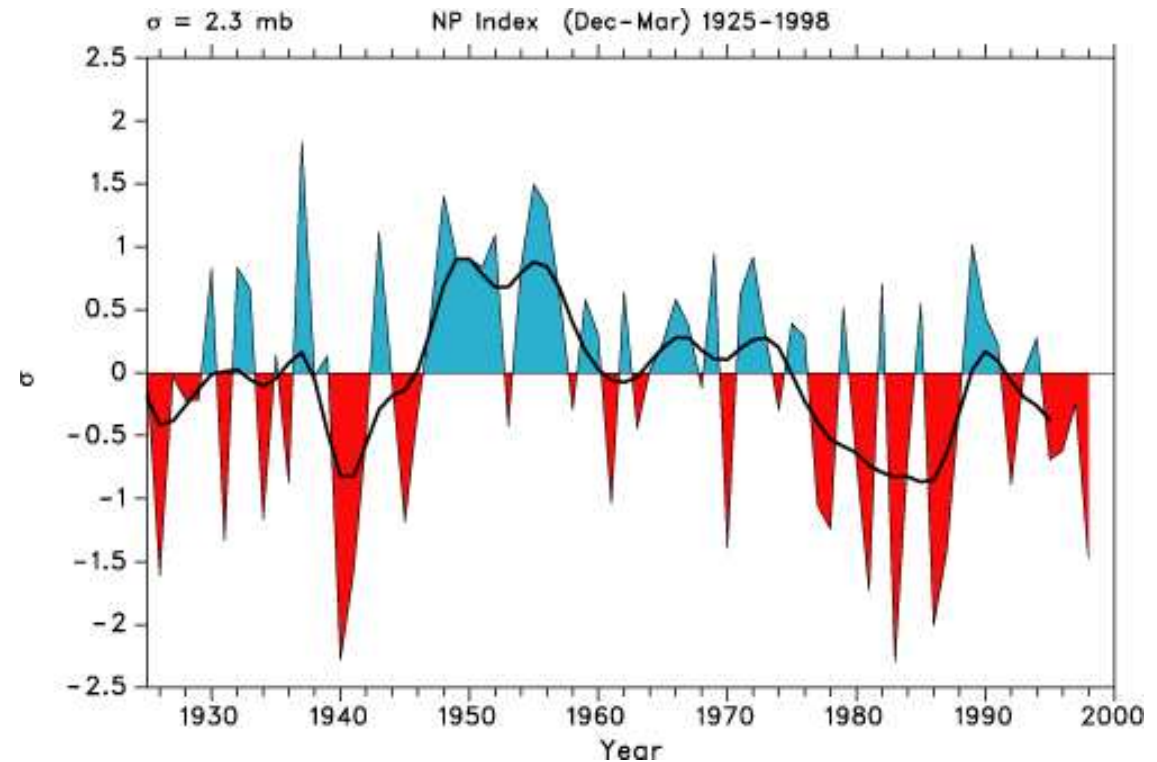
Annual mean surface air temperature change over the years 50-100 after a collapse of the THC in HadCM3.

Vellinga et al., 2002 CC

D4: Pacific and Indian Ocean Decadal Variability



Seasonal temperature anomalies in the central Pacific region at selected depths from 1970 to 1992 (Deser et al., 1996, JC).

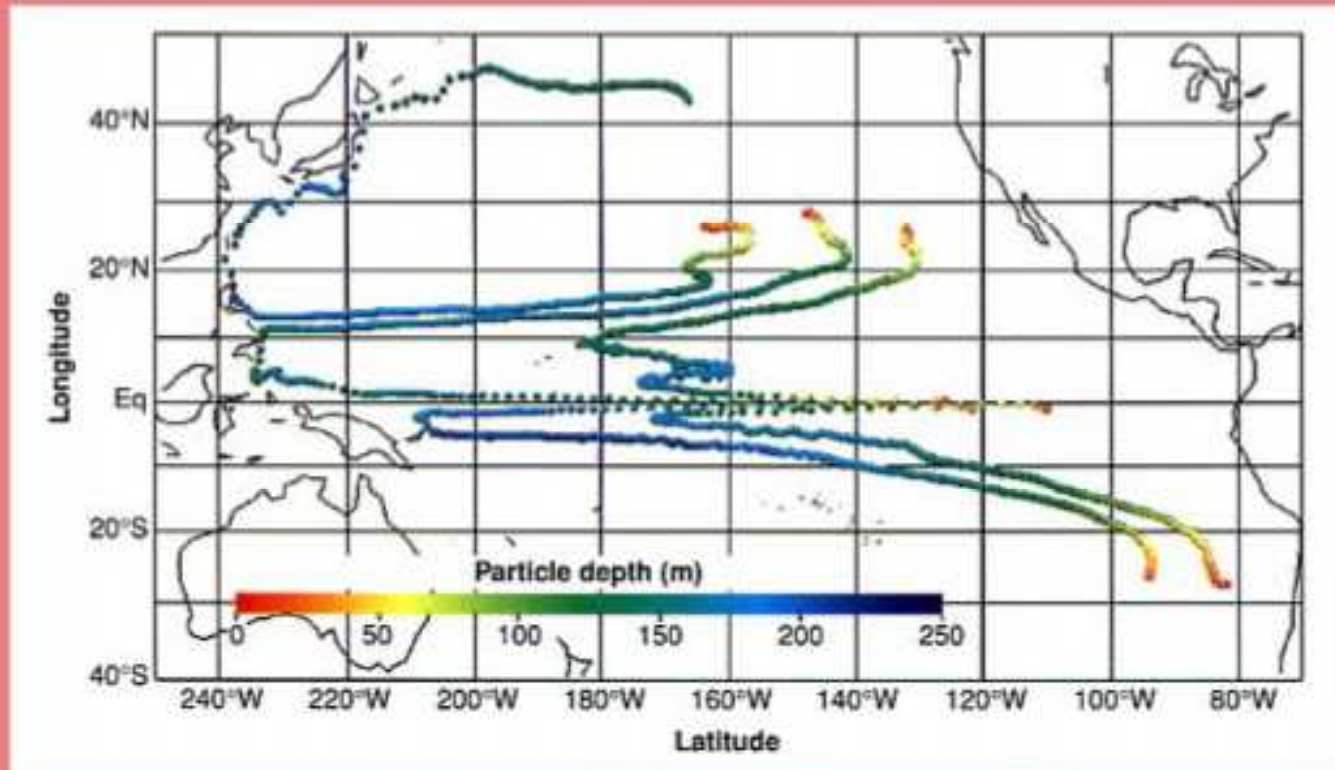


Area-averaged SLP over the region 30N-50N, 160E-140W shows a decadal time scale variability (Trenberth and Hurrell, 1994, CD).

Possible Mechanisms of the North Pacific Decadal Variability

Decadal Variability in the North Pacific

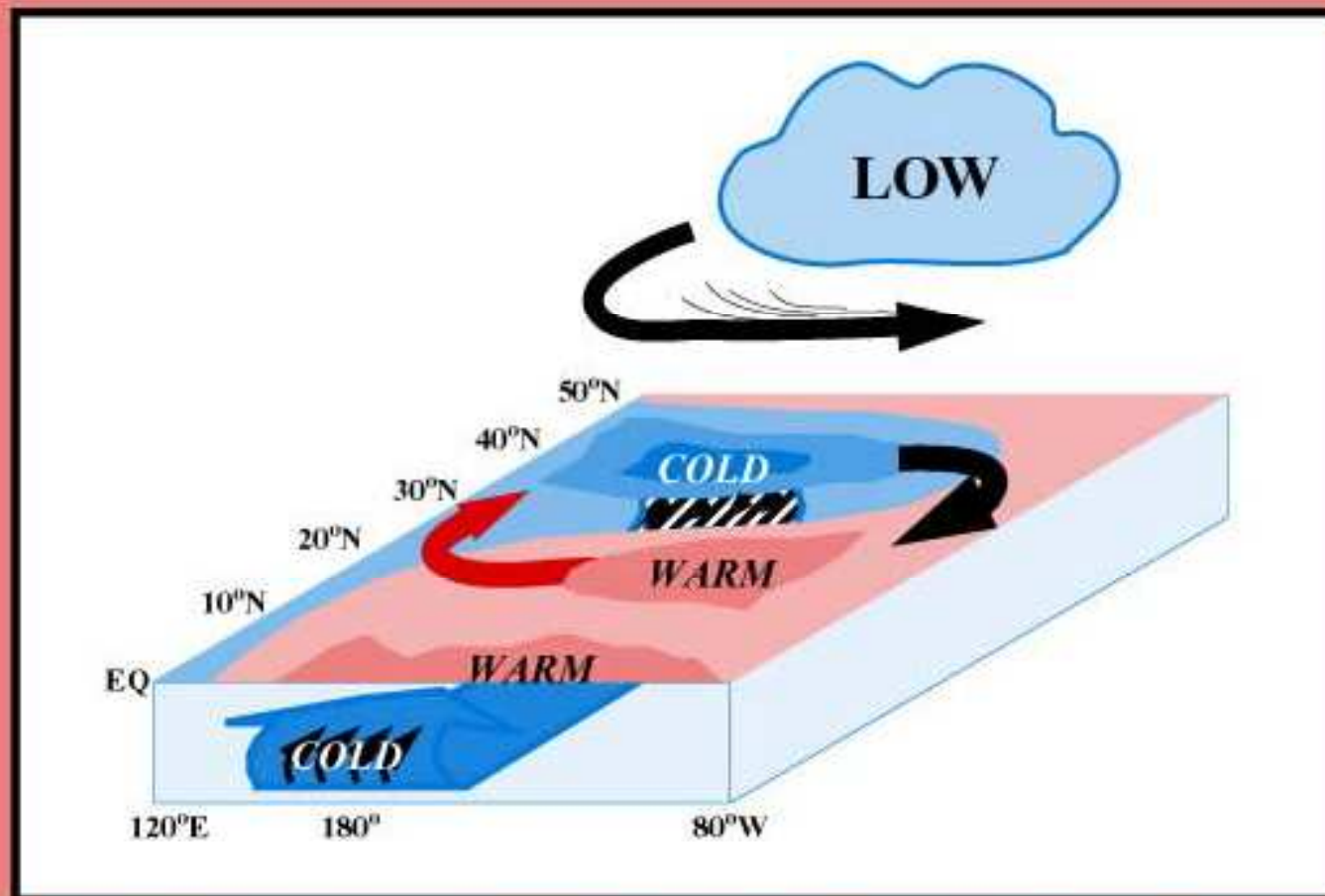
- The Subduction Hypothesis -



The paths of water parcels over a period of 16 years after subduction off the coasts of California and Peru as simulated by means of a realistic oceanic general circulation model forced with the observed climatological winds. From the colours, which indicate the depth of the parcels, it is evident that parcels move downward, westward, and equatorward unless they start too far to the west off California, in which case they join the Kuroshio Current. Along the equator they rise to the surface while being carried eastward by the swift Equatorial Undercurrent (Gu, Philander, 1997, *Science*, 275, 805-807).

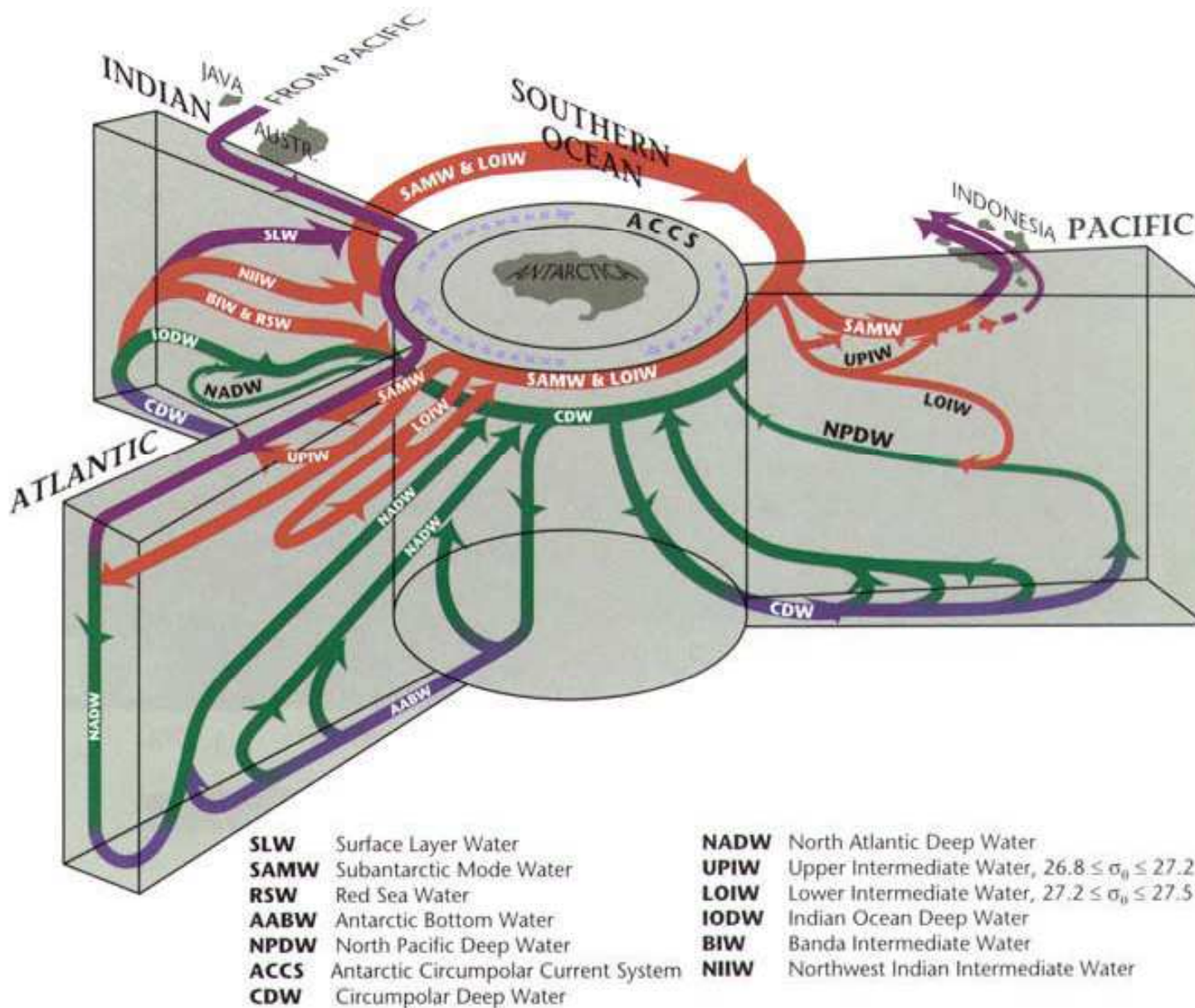
AV/D4/99-2

Decadal Variability in the North Pacific - Possible Mechanisms -



Schematic diagram of possible mechanisms of decadal climate variability. Extratropical decadal climate variability may be caused by a cycle involving unstable air-sea interactions between the subtropical gyre circulation in the North Pacific and the Aleutian low-pressure system. Long-term fluctuations of the tropical SSTs may, presumably, be induced by an influx of water from higher latitudes which subducts in the North Pacific and flows southeastward along the surfaces of constant density before equatorial upwelling brings it back to the surface. The tropical SST anomalies may in turn also affect the Aleutian low-pressure system (S. Venkze, 1998, Ocean-atmosphere interactions of decadal timescales, Thesis, Max-Planck-Institut für Meteorologie, Hamburg, 100pp).

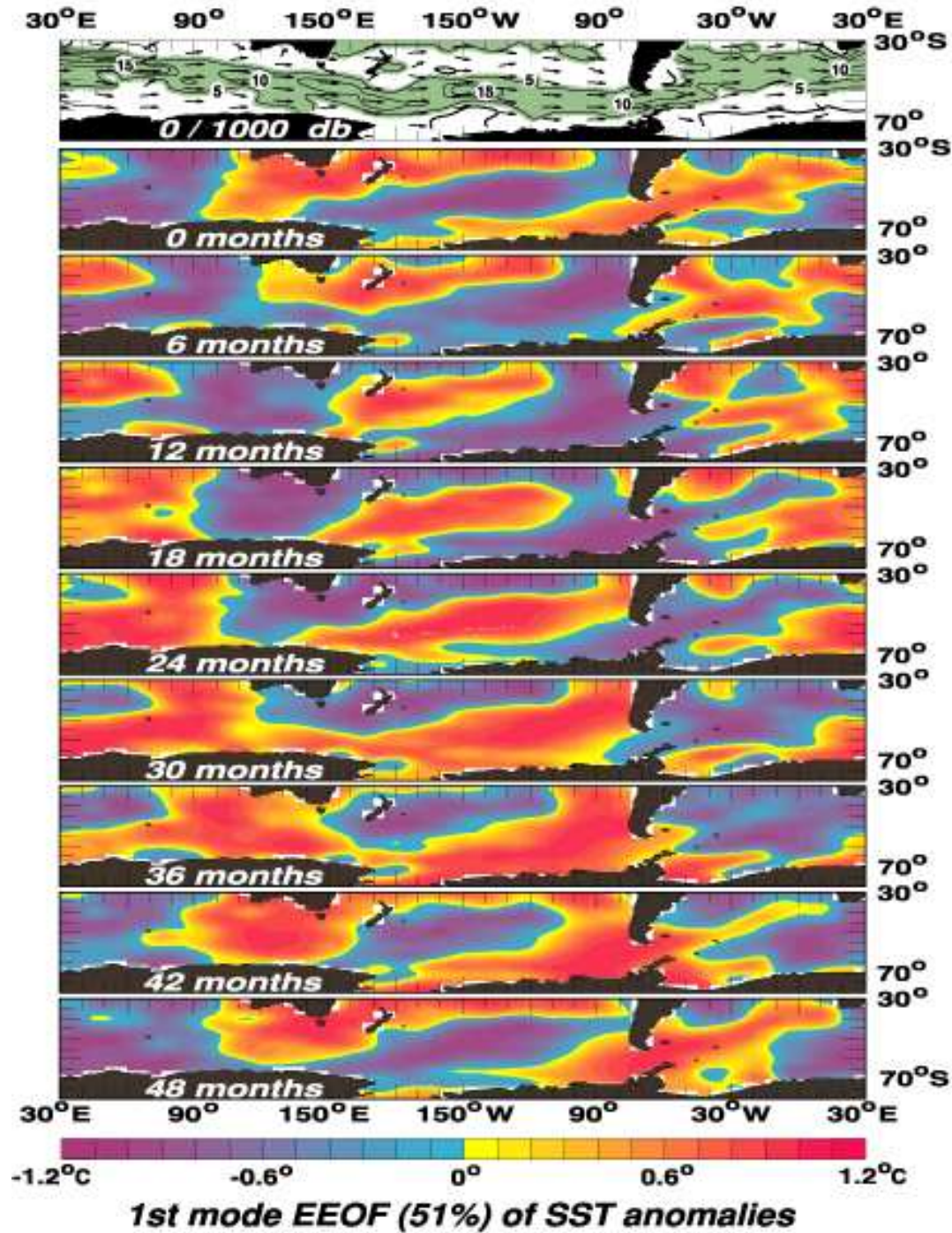
D5: Southern Ocean Climate Variability



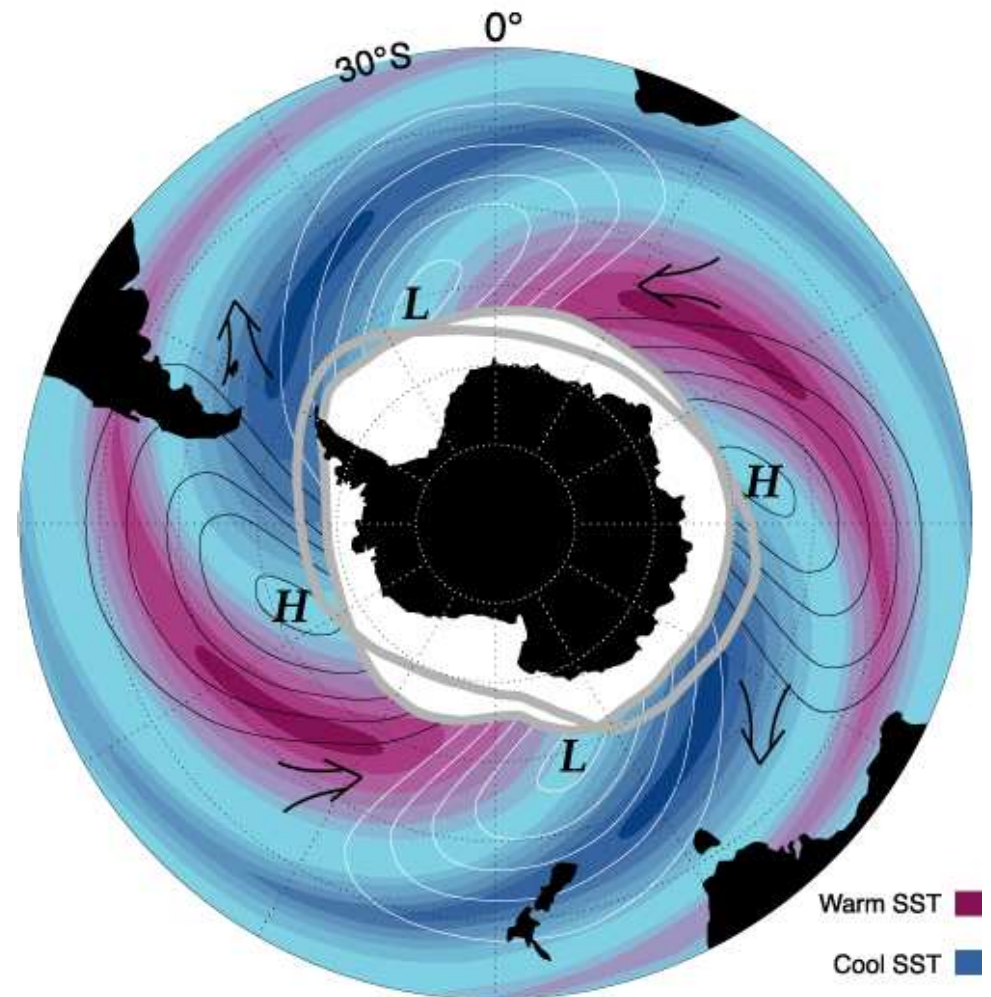
Water mass transformations in the Southern Ocean close the overturning circulations by converting deep water which upwells at high latitude into lighter intermediate waters and denser bottom waters.

The Antarctic Circumpolar Current connects the ocean basins, allowing a global overturning circulation to exist, and allowing anomalies to propagate between basins and influence the climate downstream.

The Antarctic Circumpolar Wave

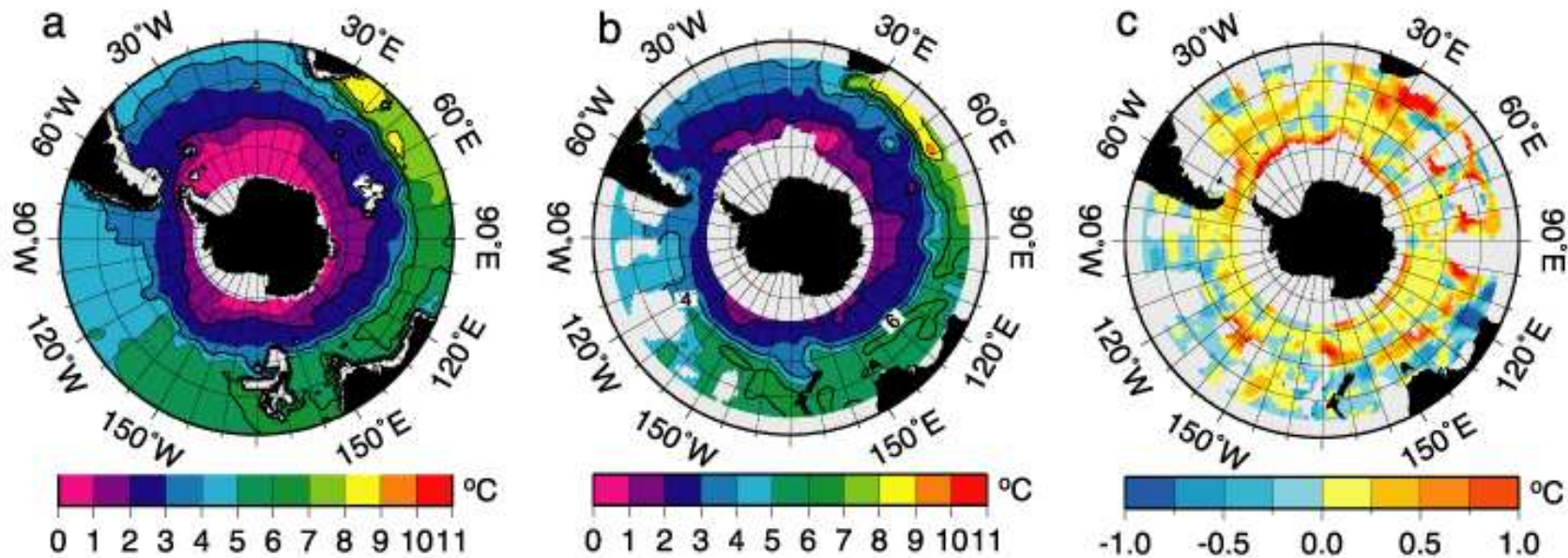


Schematic summary of SST, SLP, meridional wind and sea-ice extent

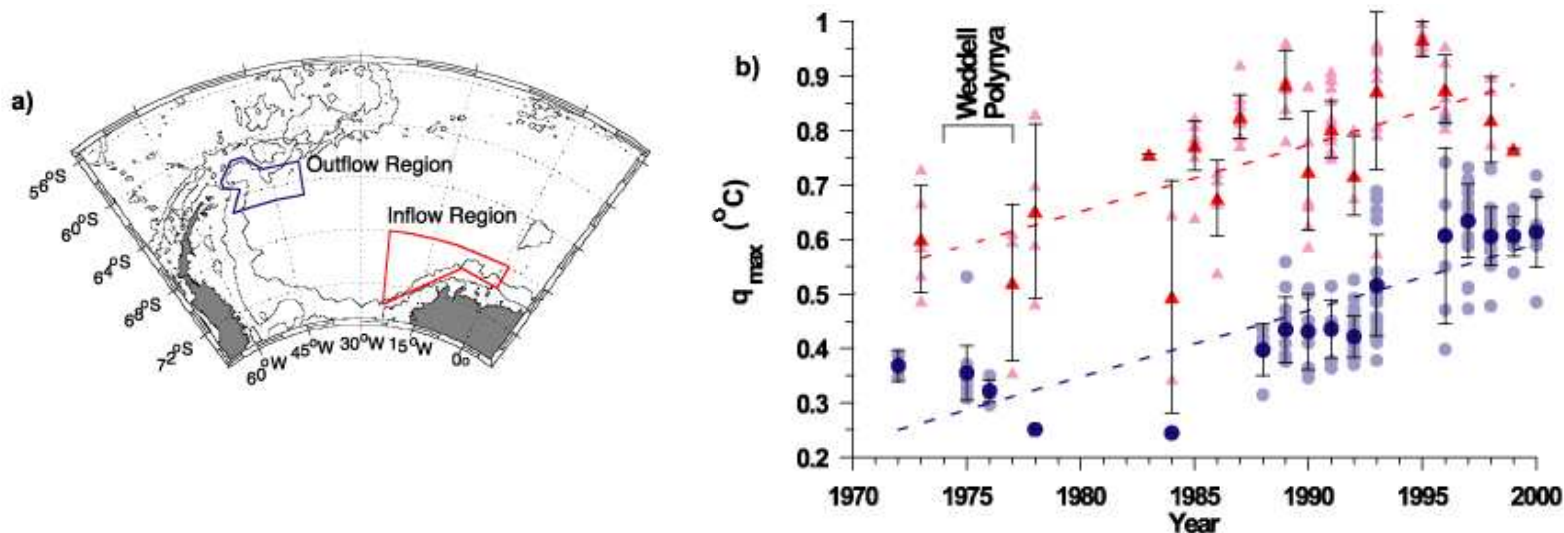


White and Peterson, 1996, Nature

Warming of the Southern Ocean



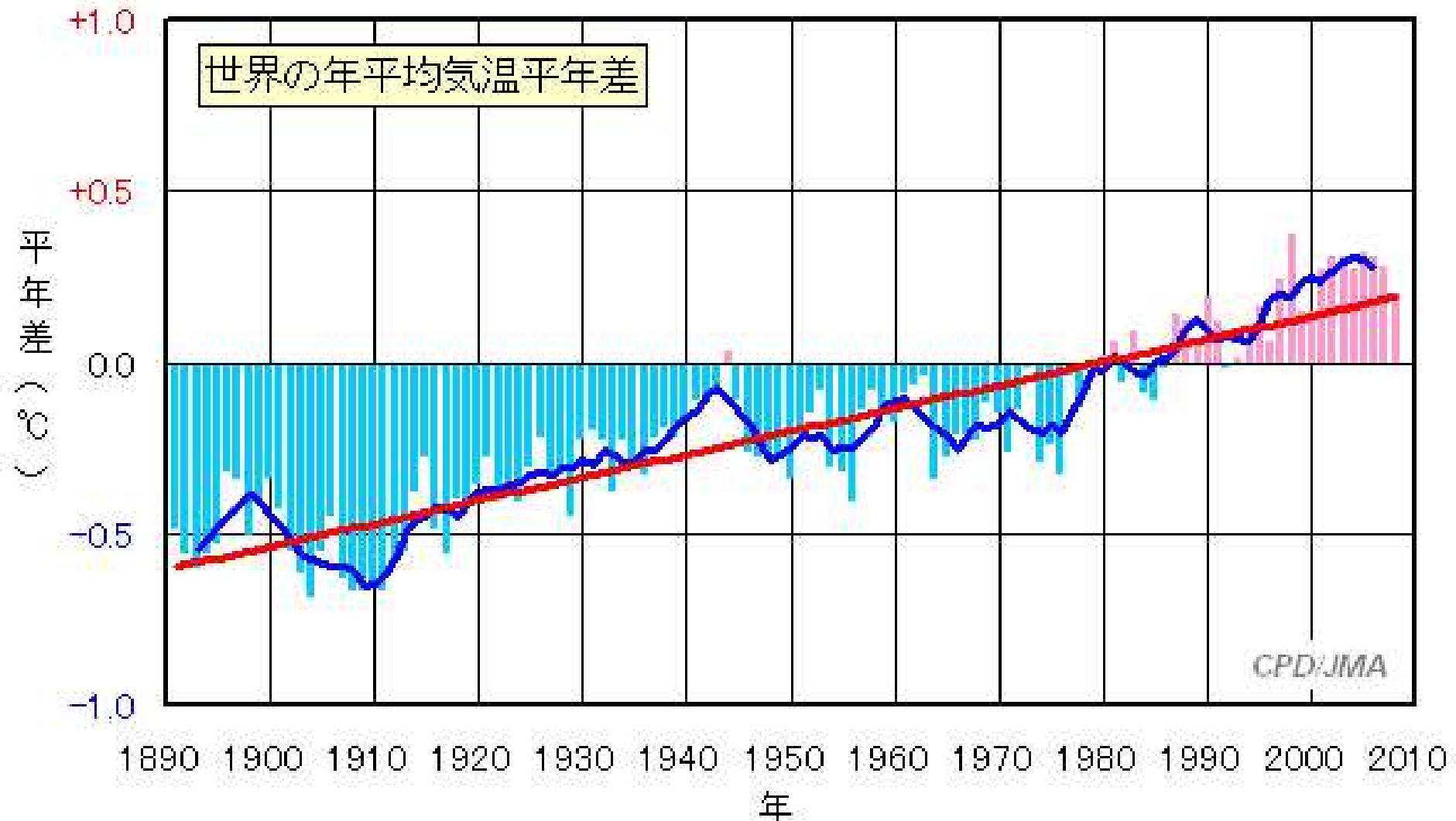
(a) Hydrographic temperature at 900 m prior to 1990. (b) ALACE floats temperature at 900 m since 1990. (c) (b) minus (a).



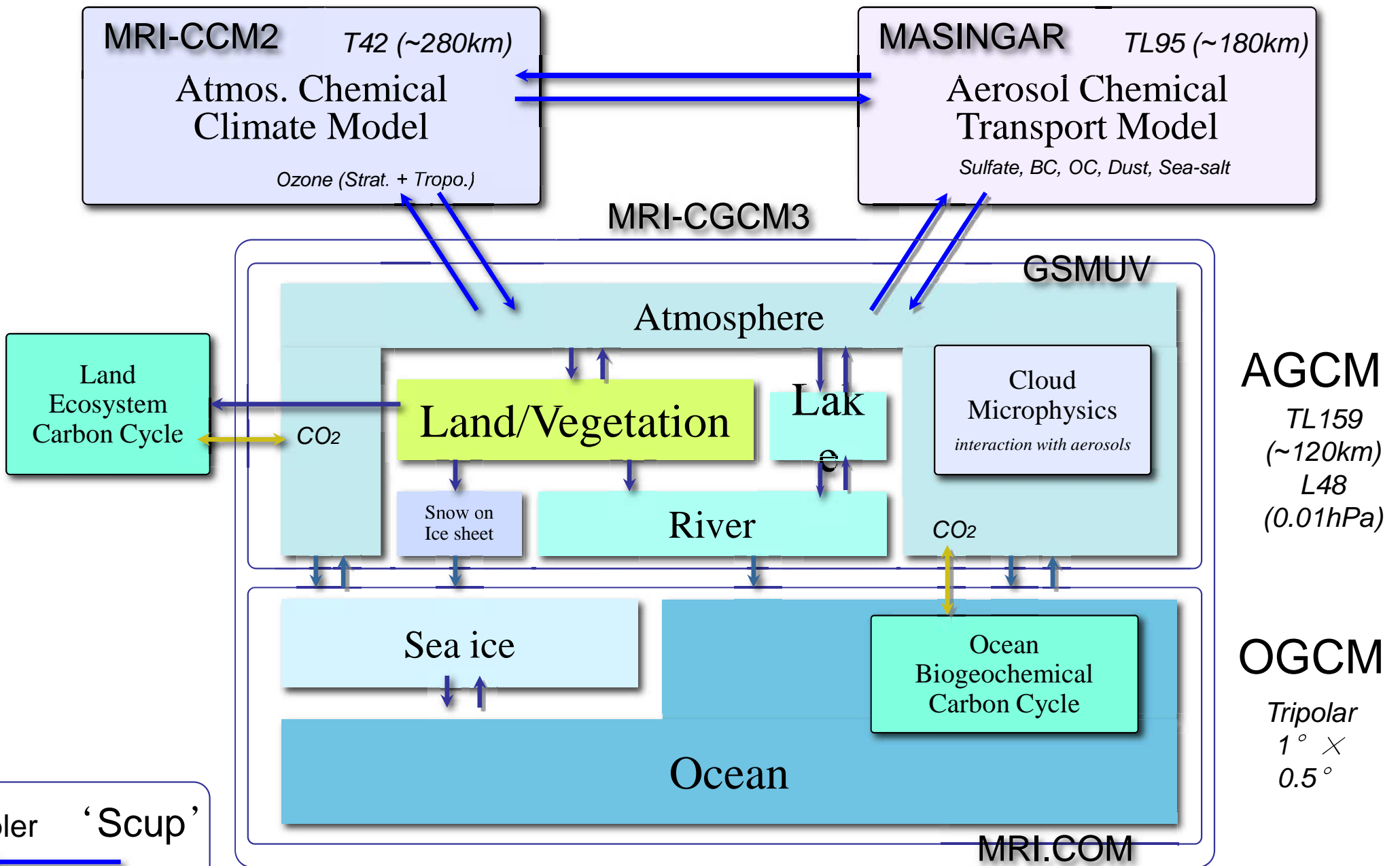
Long-term warming of Weddell Sea Deep Water.

A1: Climate Change Prediction

Global mean surface air temperature

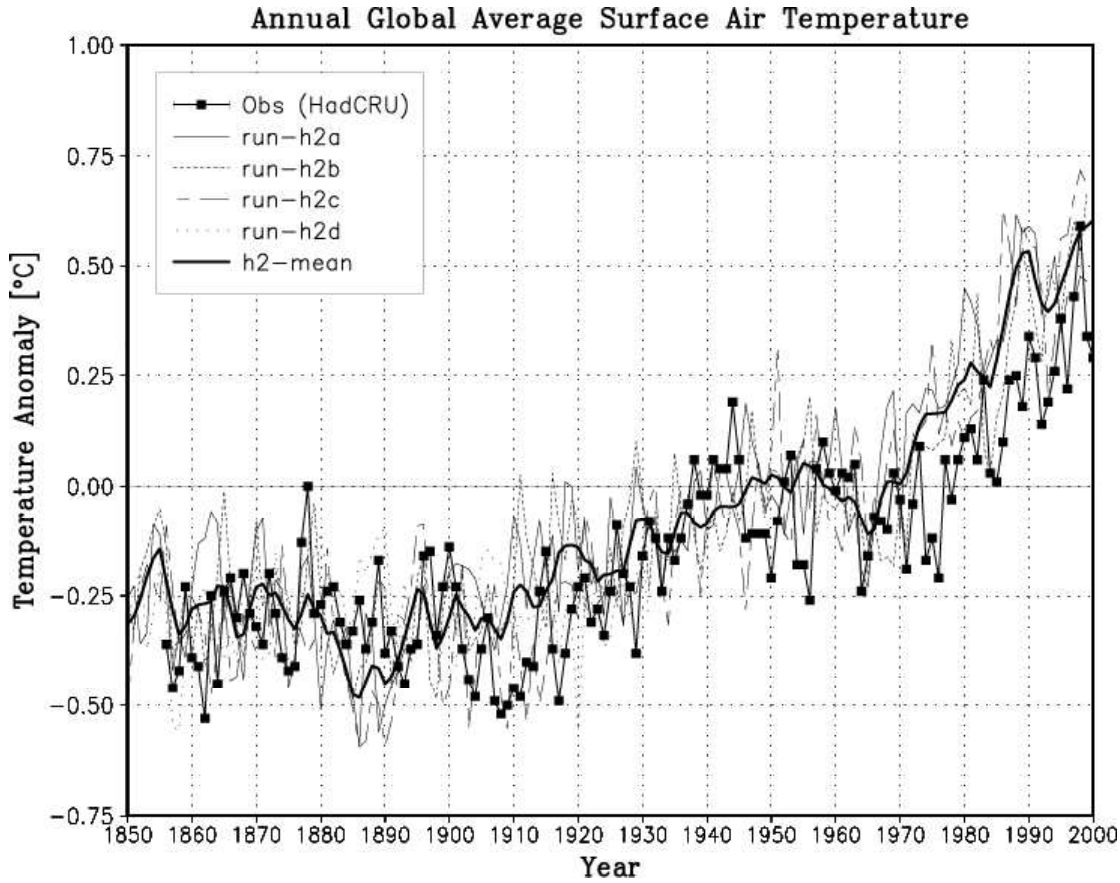


MRI Earth System Model

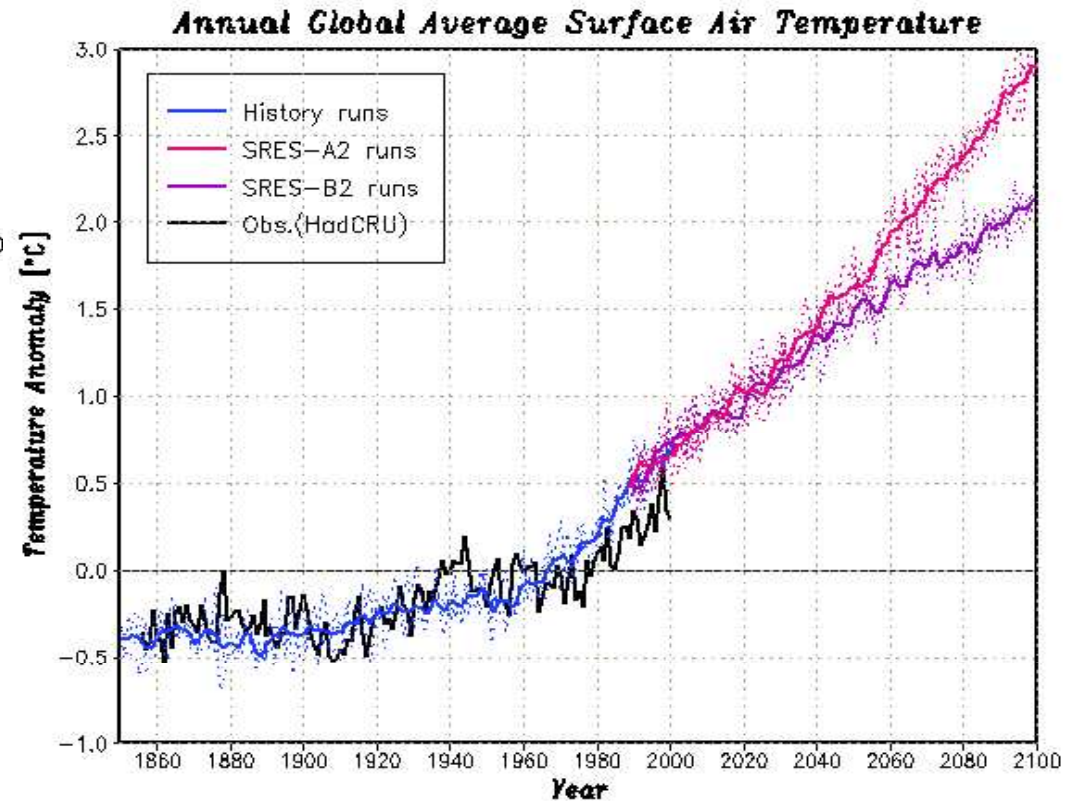


Each component can be coupled with different resolutions

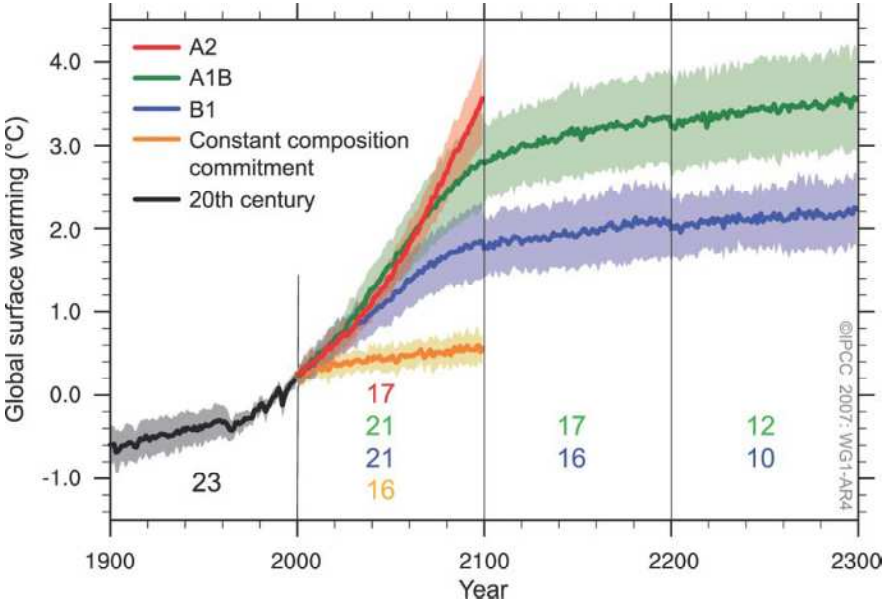
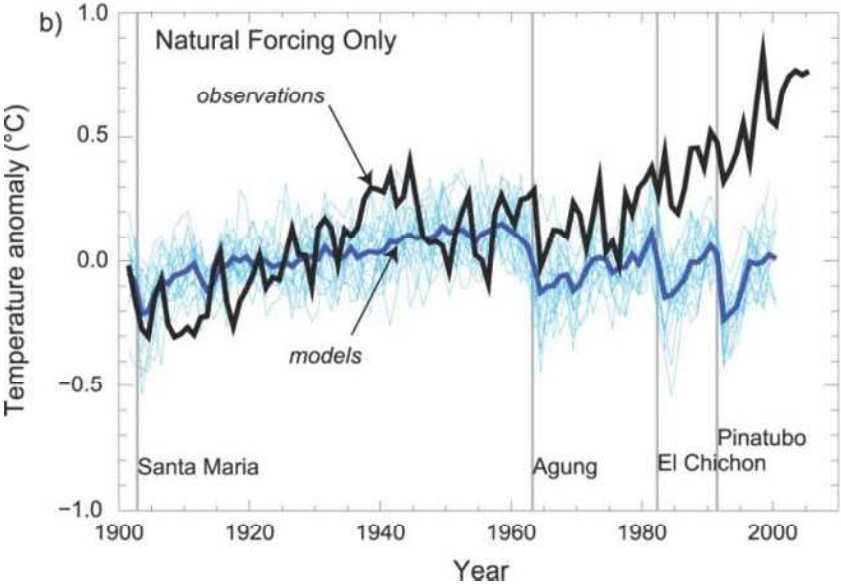
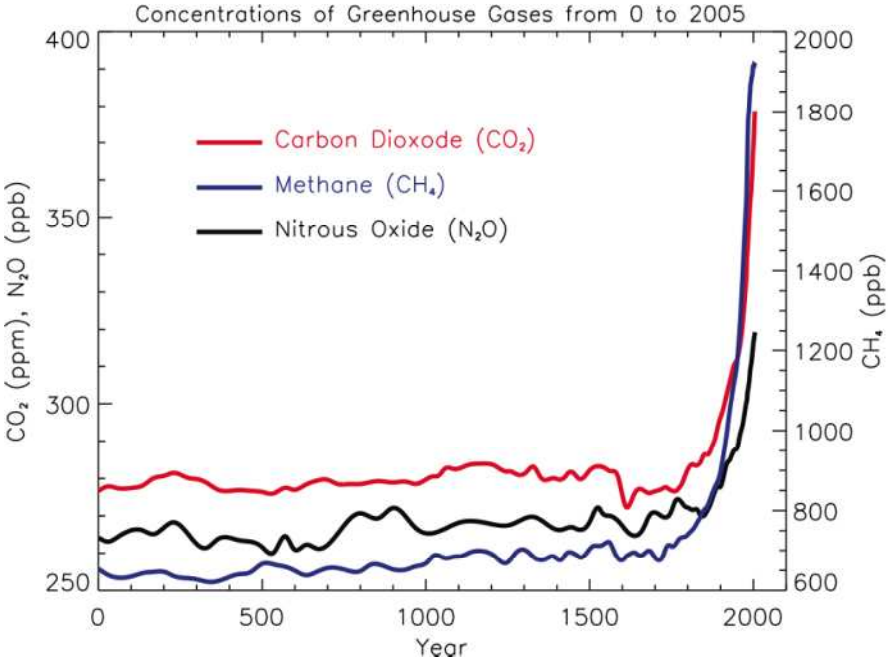
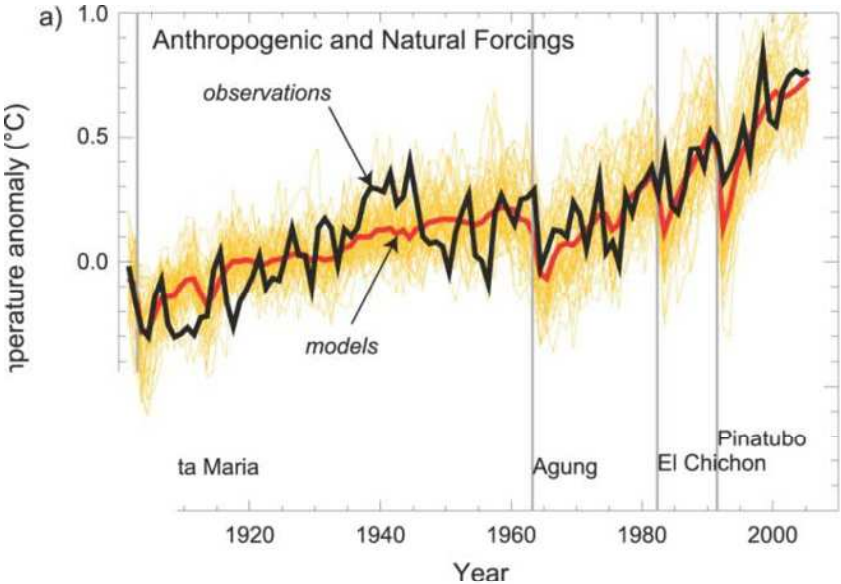
Simulation of Global Average Surface Air Temperature by MRI-CGCM2



- 0.75 C increase at 1990s
- Rapid warming starts 1970s, 10 years earlier than observation
- Model reproduced temperature trend and interdecadal change



AR4 Global Mean Temperature Simulation



Projected Change of DJF and JJA Precipitation

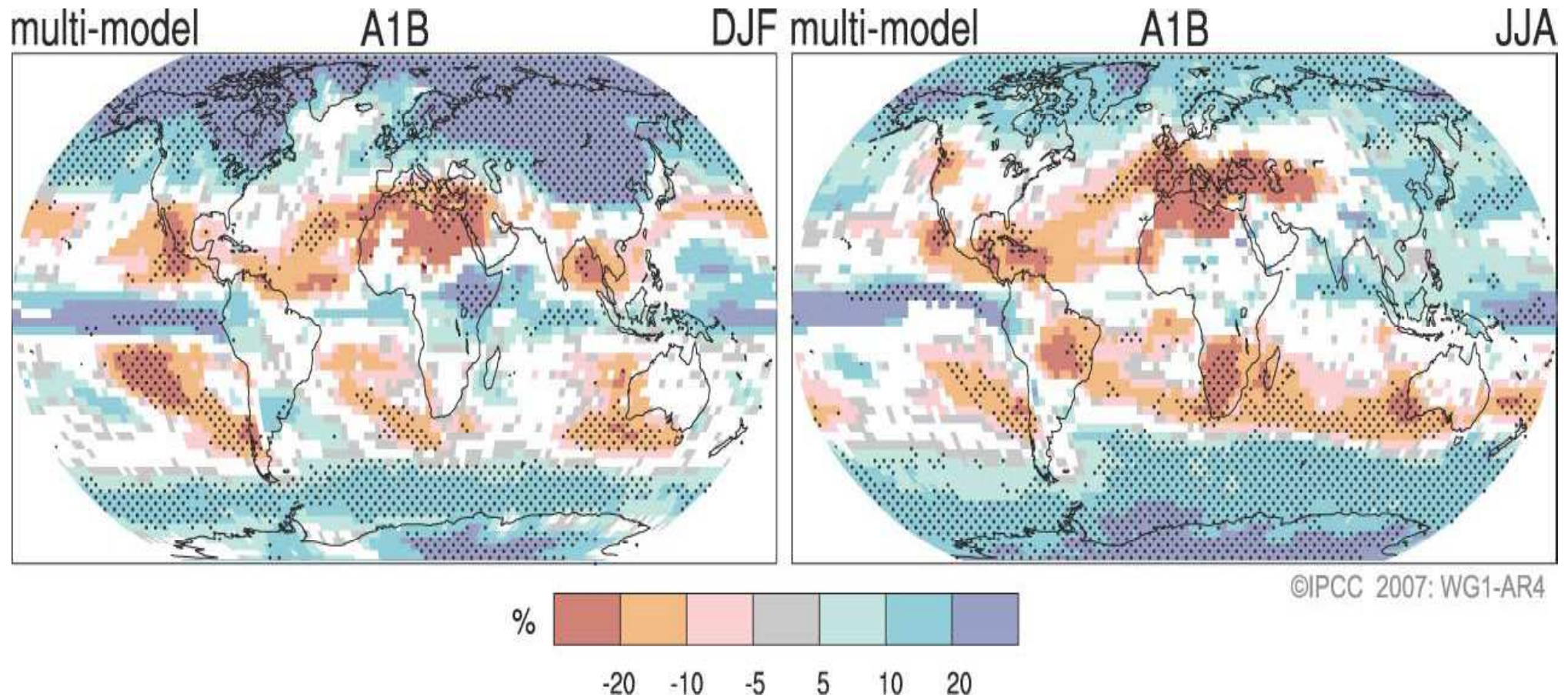


Figure SPM.7. *Relative changes in precipitation (in percent) for the period 2090–2099, relative to 1980–1999. Values are multi-model averages based on the SRES A1B scenario for December to February (left) and June to August (right). White areas are where less than 66% of the models agree in the sign of the change and stippled areas are where more than 90% of the models agree in the sign of the change. {Figure 10.9}*

Precipitation Intensity and Dry days

From <http://www.ipcc.ch>

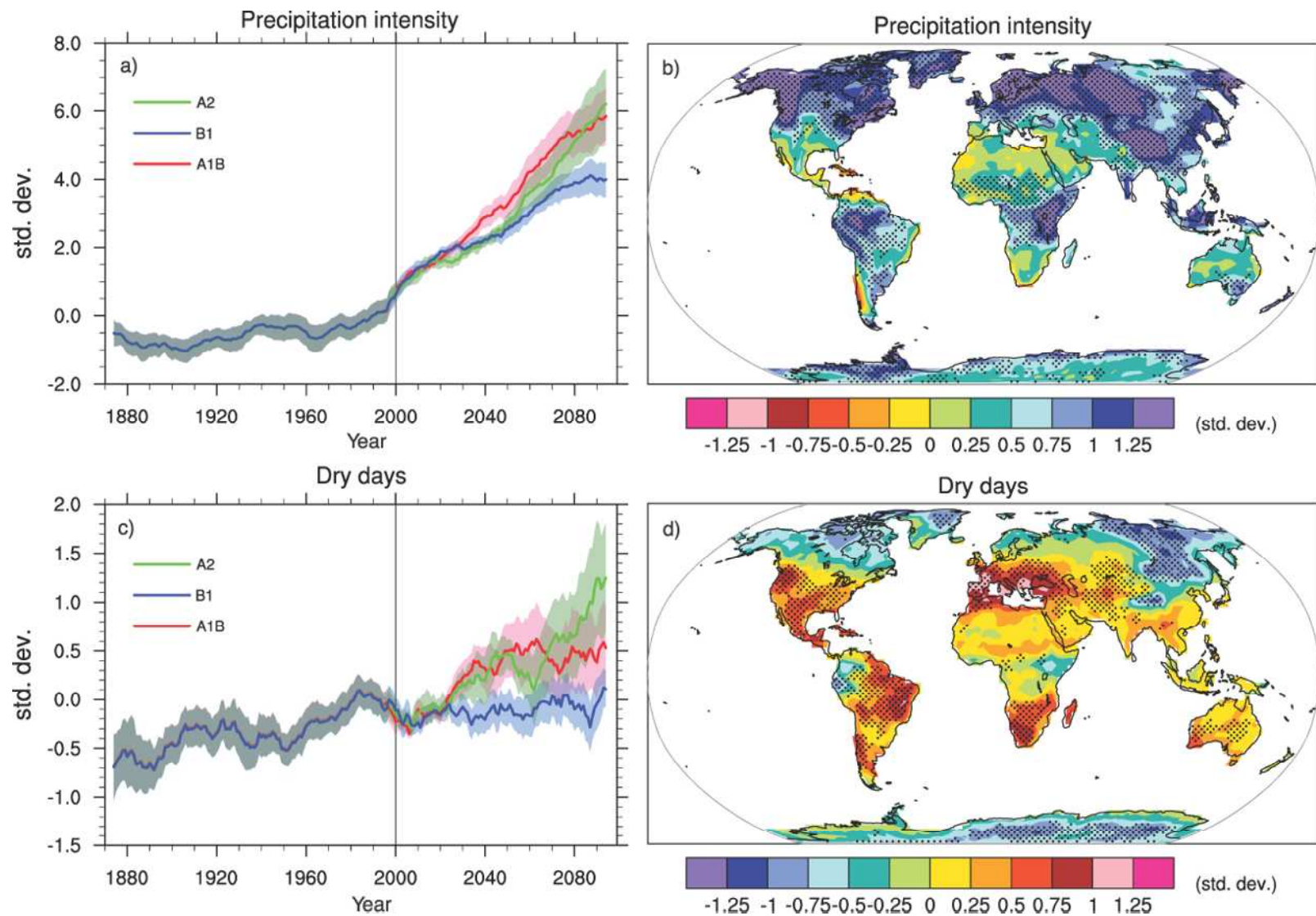


Figure 10.18. Changes in extremes based on multi-model simulations from nine global coupled climate models, adapted from Tebaldi et al. (2006). (a) Globally averaged changes in precipitation intensity (defined as the annual total precipitation divided by the number of wet days) for a low (SRES B1), middle (SRES A1B) and high (SRES A2) scenario. (b) Changes in spatial patterns of simulated precipitation intensity between two 20-year means (2080–2099 minus 1980–1999) for the A1B scenario. (c) Globally averaged changes in dry days (defined as the annual maximum number of consecutive dry days). (d) Changes in spatial patterns of simulated dry days between two 20-year means (2080–2099 minus 1980–1999) for the A1B scenario. Solid lines in (a) and (c) are the 10-year smoothed multi-model ensemble means; the envelope indicates the ensemble mean standard deviation. Stippling in (b) and (d) denotes areas where at least five of the nine models concur in determining that the change is statistically significant. Extreme indices are calculated only over land following Frich et al. (2002). Each model's time series was centred on its 1980 to 1999 average and normalised (rescaled) by its standard deviation computed (after de-trending) over the period 1960 to 2099. The models were then aggregated into an ensemble average, both at the global and at the grid-box level. Thus, changes are given in units of standard deviations.

Sea Level Change

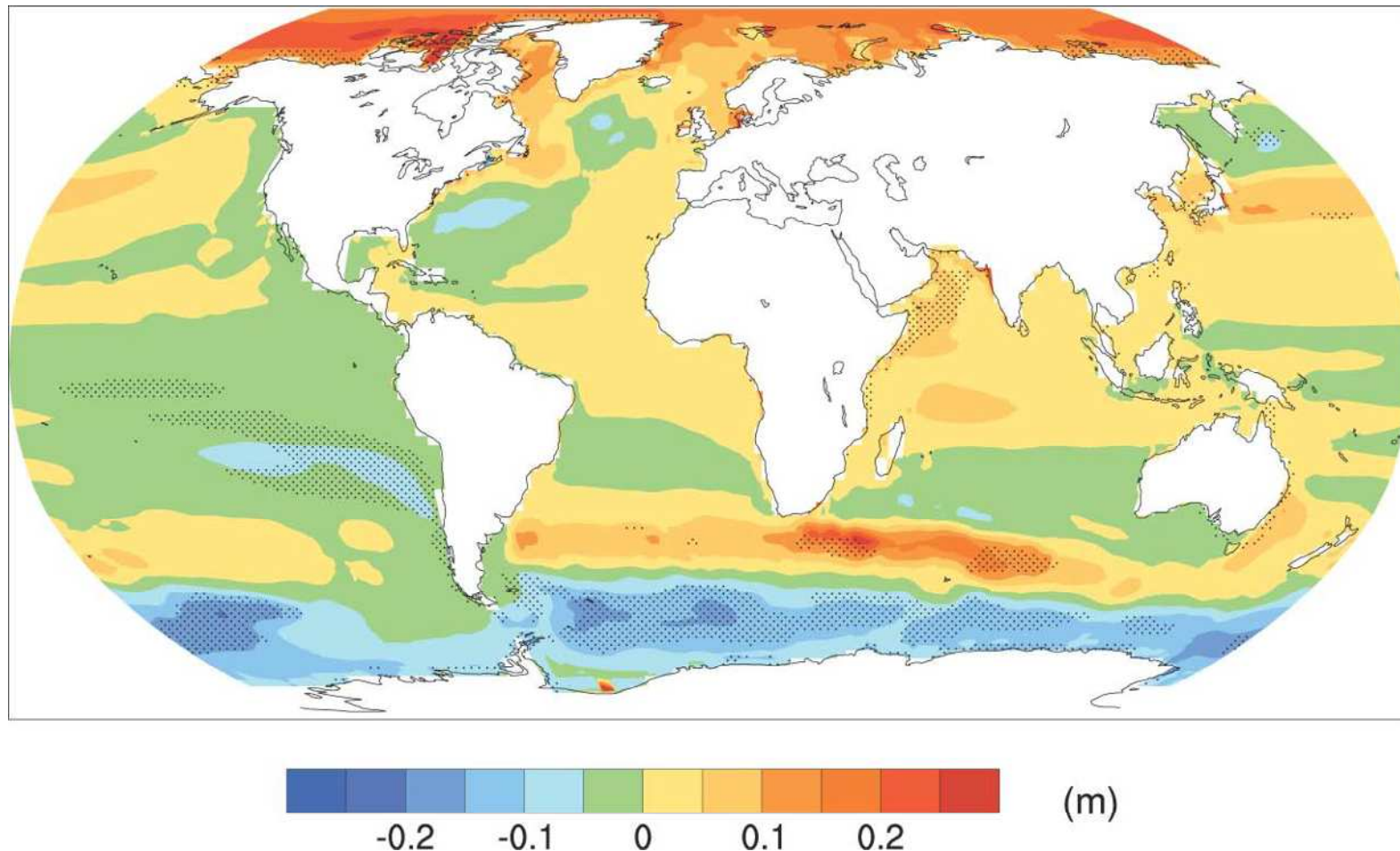


Figure 10.32. Local sea level change (m) due to ocean density and circulation change relative to the global average (i.e., positive values indicate greater local sea level change than global) during the 21st century, calculated as the difference between averages for 2080 to 2099 and 1980 to 1999, as an ensemble mean over 16 AOGCMs forced with the SRES A1B scenario. Stippling denotes regions where the magnitude of the multi-model ensemble mean divided by the multi-model standard deviation exceeds 1.0.

Future Change in Tropical Cyclones

Projection of the Change in Future Weather Extremes Using Super-High-Resolution Atmospheric Models

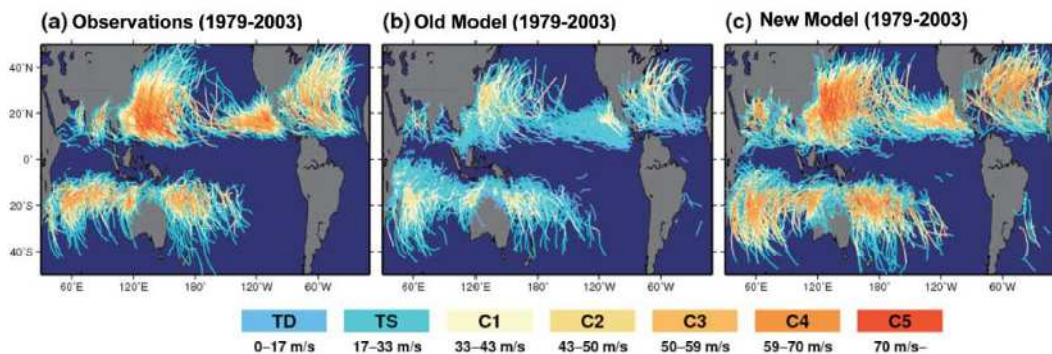


Figure 1. Global distribution of tropical cyclones for (a) observations, (b) the present-day simulation using the old model, and (c) using the new model. Tropical cyclone track

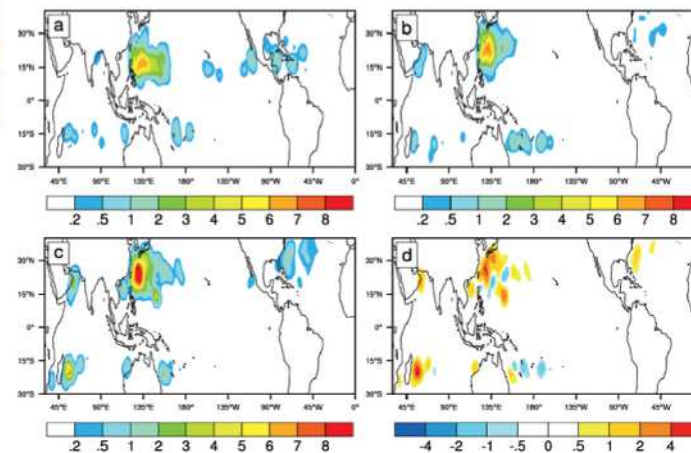


Figure 2. Tropical cyclone frequency of Category 5 storms for (a) observations (1979-2003), (b) present-day simulation by the new model (1979-2003), (c) future simulation, and (d) future changes. Unit is number per 25 years.

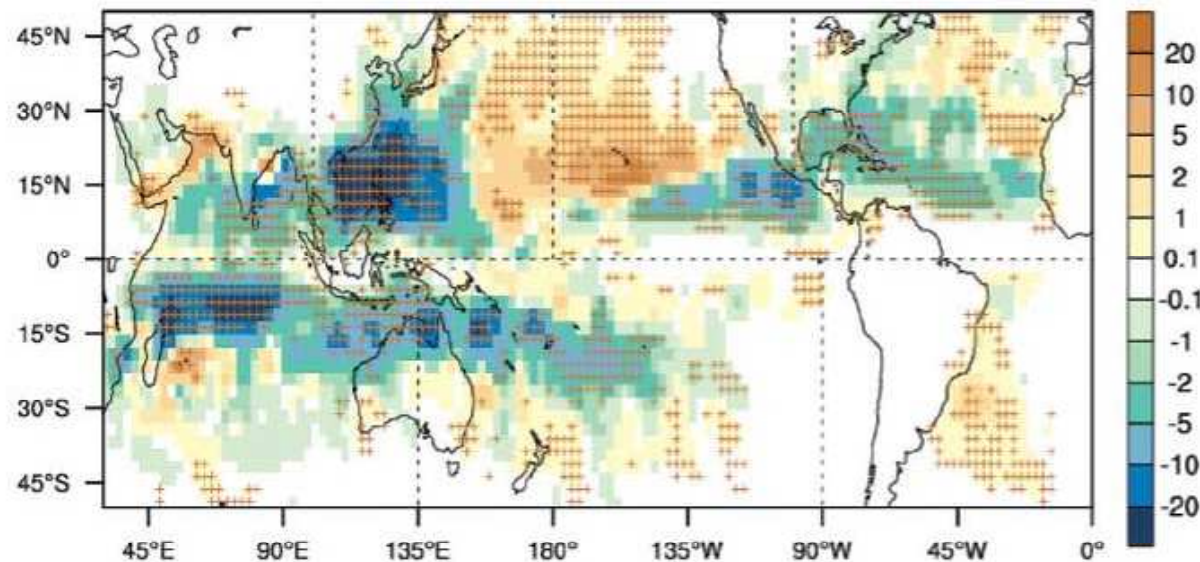


Figure 3. Ensemble mean future changes in tropical cyclone frequency. Unit is number per 25 years. Cross marks indicate that more than 10 experiments out of 12 experiments project the same sign.

SUMMARY

- **Unusual weather** and climate are attributed to unusual atmospheric flows, storms and convective disturbance.
- However, atmospheric environment is maintained and influenced by other elements playing roles to sustain the **climate system**.
- Sometimes, unusual convective activity can be connected to long-term SST anomalies related to **ocean** variability.

- **Radiative processes** including longwave absorption by greenhouse gases and shortwave reflection by snow, ice, clouds and aerosols determine the Earth's ground temperature.
- The **Earth's ground temperature** and ice-coverage are influential to vertical and horizontal atmospheric oceanic stability, amount of water vapor and water cycle, and can affect global atmospheric and oceanic flows, storms and convective features and then our daily lives.
- Therefore, we need to continue **careful watches** over global and local climate systems.